Fakultät für Elektrotechnik und Informationstechnik
Lehrstuhl für Hybride Elektronische Systeme

High Resolution Probing of Charge Carrier Properties in Semiconductor Device Materials

Sören Hommel

Vollständiger Abdruck der von der Fakultät für Elektrotechnik und Informationstechnik der Technischen Universität München zur Erlangung des akademischen Grades eines Doktor-Ingenieurs genehmigten Dissertation.

Vorsitzender:
Prof. Dr. rer. nat. Bernhard Wolfrum
Prüfende/-r der Dissertation:
1. Prof. Dr. rer. nat. Franz Kreupl
2. Prof. Dr.-Ing. habil. Markus Becherer

Die Dissertation wurde am 09.11.2018 bei der Technischen Universität München eingereicht und durch die Fakultät für Elektrotechnik und Informationstechnik am 05.04.2019 angenommen.

Abstract

The downsizing of semiconductor structures predicted in 1965 by Moore's law has been ongoing ever since. This trend has lead semiconductor industry to many innovative solutions, involving reduced gate lengths, "fins" and "surrounded gates", and new materials such as high-k dielectrics and wide bandgap semiconductors, e.g., silicon carbide (SiC) and gallium nitride (GaN). In modern semiconductor devices the entire transistor is built within a few tens to hundreds of nanometers of depth. This drives the need for new characterization methods to image doped regions within one semiconductor material with high spatial resolution.
A method for the high resolution quantification of implant or charge carrier concentration was lacking for decades. This thesis aims at expanding the available scanning probe methods (SPM) to close this yet existing gap. A number of different carrier- and dopant profiling techniques are compared using a standard dopant calibration sample. Scanning Microwave Microscopy (SMM), on which the focus of this thesis lies, stands out by fulfilling the requirements in spatial resolution, and signal dependence on dopant density. Furthermore, the SMM signal contains the information to distinguish the dopant types, enabling the development of dopant quantification methods.
Since SMM combines the mechanical tip dimensions with the microwave excitation region, the effective scan resolution is not directly given by the cantilever parameters. The highly confined two dimensional electrongas (2DEG) in an aluminum gallium nitride (AlGaN)/GaN heterostructure was scanned and the obtained profile deconvoluted with the expected shape of the 2DEG profile to reveal the effective tip radius in SMM. A comparison between different cantilevers shows that the effective scan resolution is limited mainly by the cantilever radius and shape and only by a smaller extent by the microwave excitation region.
An established procedure is applied to calibrate the S_{11} data recorded in SMM into capacitance and resistance. Based on the resistance signal, a method to calculate resistivity and dopant density from the SMM resistance is employed. It enables the quantitative two-dimensional dopant profiling with an accuracy of better than 60 %.

A second introduced method is based on the SMM capacitance data. It enables to distinguish the dopant type and shows a better repeatability. The difference between accumulation and depletion capacitance is used for dopant type distinction. The depletion capacitance is shown to present a reliable tool to investigate the relations between dopant densities. This enables the calculation of dopant densities deviating from the datasheet densities by a factor of 0.1 to 20. Further improvements are achieved by using parameter fits. The method enables the investigation of dopant types and densities in one single image with all data obtained in one single measurement.
The transfer of the dopant density calculation to an industrial application is demonstrated for an ESD diode. A further industrial application is the spatially resolved imaging of charge carriers accumulated by trapping effects, shown on the example of a Si diode.

Kurzfassung

Seit der Formulierung des Moorschen Gesetzes im Jahre 1965 schreitet die Miniaturisierung von Halbleiterstrukturen stetig voran. Dieser Trend zwingt die Halbleiterindustrie zu innovativen Lösungen. Dazu zählen nicht nur reduzierte Kanallängen, sondern auch neue Materialien wie High-k-Dielektrika und Halbleiter mit großer Bandlücke wie Siliziumkarbid (SiC) und Galliumnitrid (GaN). In modernen Halbleiterstrukturen haben ganze Transistoren nur wenige zehn bis hundert Nanometer Tiefe. Daraus ergibt sich die Notwendigkeit einer neuen Methode, die es erlaubt Dotiergebiete kleinster Transistoren mit einer hohen lateralen Auflösung darzustellen.

Nach einer solchen Methode zur quantitativen, hochauflösenden Darstellung von Dotierkonzentrationen wird seit Jahrzehnten gesucht. Ziel dieser Arbeit ist die Weiterentwicklung existierender Methoden der Rasterkraftmikroskopie, um diese Lücke zu schließen. Eine Reihe verschiedener Methoden zur Erstellung von Dotierprofilen wird mit Hilfe einer Standard Dotierprobe verglichen. Rastermikrowellenmikroskopie (SMM), die im Fokus dieser Arbeit steht, erfüllt sowohl die Anforderungen an die laterale Auflösung, als auch an die Skalierung der Signale mit der Dotierkonzentration. Zudem lässt sich auch der Dotiertyp aus den SMM Signalen bestimmen. Damit bietet SMM die perfekte Basis zur Entwicklung quantitativer Dotiermessmethoden.

Die Auflösung von SMM hängt sowohl von Geometrie und mechanischen Eigenschaften der Messspitze als auch von der Eindringtiefe der Mikrowelle ab. Wie diese Parameter in den effektiven Spitzenradius eingehen ist allerdings unklar. Um den effektiven Spitzenradius zu bestimmen wurde das stark komprimierte zweidimensionale Elektronengas (2DEG) einer Aluminiumgalliumnitrid (AlGaN)/GaN Heterostruktur im Querschnitt gescannt und das extrahierte Profil mit dem erwarteten Profil des 2DEGs entfaltet. Ein Vergleich verschiedener Spitzen zeigt, dass der effektive Spitzenradius maßgeblich von Geometrie und nur wenig von der Eindringtiefe geprägt wird und damit die Qualität der Spitze großen Einfluss auf die SMM Auflösung hat.

Eine etablierte Methode wird zur Kalibrierung der SMM S_{11} Daten in Kapazität und Widerstand verwendet. Eine auf den resultierenden SMM Widerstandsdaten basierende Methode ermöglicht die Berechnung von Dotierkon-

zentrationen. Diese Methodik ermöglicht die zweidimensionale, quantitative Messung von Dotierkonzentrationen mit einer Genauigkeit von besser als 60 %. Eine zweite auf dem kapazitiven Signalteil basierende Methode wird eingeführt. Diese ermöglicht die Unterscheidung des Dotiertyps und weist eine hohe Reproduzierbarkeit auf. Die Differenz zwischen Akkumulations- und Verarmungskapazität wird hierbei zur Bestimmung des Dotiertyps genutzt. Mit Hilfe der Verarmungskapazitäten können Relationen zwischen den Dotierungen zuverlässig bewertet werden. Aus diesen können Dotierkonzentrationen berechnet werden, die mit einem Faktor zwischen 0,1 und 20 von den erwarteten Konzentrationen abweichen. Die Genauigkeit kann durch Parameterfits weiter optimiert werden. Dotiertyp und -konzentration können somit unter Verwendung von Daten aus einer einzigen Messung in einem einzigen Bild dargestellt werden.
Die Anwendung der Methodik auf industrielle Probleme wird am Beispiel einer ESD Diode sowie durch die lateral aufgelöste Darstellung eines durch Oxidstörstellen verursachten Elektronenkanals in einer Siliziumdiode demonstriert.

Contents

1 Introduction **8**

2 Theoretical Background **10**

2.1 Vector Network Analysis 10

2.2 Metal Oxide Semiconductor Structure 13

2.2.1 States of a MOS-Structure 13

2.2.2 Surface Potential Dependencies 19

2.2.3 Capacitance Voltage Characteristics 21

2.2.4 High Frequency Models 23

3 Methods for Dopant Profiling **25**

3.1 Basics of Atomic Force Microscopy and Electrostatic Force Microscopy 25

3.2 Calibration Sample 30

3.3 Scanning Microwave Microscopy 32

3.3.1 Principle 32

3.3.2 SMM Setup 37

3.3.3 Vector Network Analyzer 39

3.4 Alternative Methods 40

3.4.1 Scanning Electron Microscopy 40

3.4.2 Scanning Capacitance Microscopy 42

3.4.3 Scanning Microwave Impedance Microscopy 44

3.4.4 Scanning Spreading Resistance Microscopy 47

3.4.5 Scattering-type Scanning Nearfield Optical Microscopy . 49

3.5 Summary 53

4 Experimental Details **56**
4.1 Sample Preparation for SMM 56
4.2 Conductive Probes 58
4.3 Finite Elements Method 60

5 Quantitative Dopant Profiling by SMM **65**
5.1 Lateral Resolution 65
5.1.1 Experimental results 65
5.1.2 Discussion 69
5.2 Dopant Density by Resistivity 70
5.2.1 Experimental results 70
5.2.2 Discussion 74
5.3 Dopant Type and Density by Capacitance 77
5.3.1 Spectroscopy 77
5.3.2 Dopant Type 80
5.3.3 Depletion Capacities 85
5.3.4 Dopant Density Calculation 87
5.3.5 Parameter Optimization 90
5.4 Industrial Applications 98
5.4.1 Dopant Profile 98
5.4.2 Trap Generated Charges 102

6 Summary **107**

Notations and Abbreviations **111**

List of Figures **115**

List of Tables **118**

List of Publications **119**

References **121**

1 Introduction

The miniaturization in semiconductor industry was predicted as early as 1965 by Moore's law, suggesting that the integration scale would increase by a factor of four every three years. The downsizing of semiconductor structures has been ongoing ever since [1, 2]. The trend towards higher integration has lead semiconductor industry to many innovative solutions to downscale semiconductor devices. Those solutions not only scale the entire device dimensions according to the reduced gate length, e.g., FinFET and further silicon on insulator (SOI) technologies [3–8], but involve new materials such as high k dielectrics and wide band-gap semiconductors, e.g., silicon carbide (SiC) and gallium nitride (GaN) [9–12]. The miniaturization is not just a phenomenon in logic devices, it more and more accounts also for power devices. In modern e.g. SOI devices, the entire transistor is built within a few tens to hundreds of nanometers of depth, which requires structuring accuracies of implants and etch processes in the order of a few nanometers. The high demand for fabrication accuracy drives the need for new characterization methods with a high spatial resolution, which not only image metallic structures and dielectrics, but also doped regions within semiconductor material.

Various dopant profiling methods are deployed in technology development, process control and failure analysis. Two widely used approaches are on the one hand secondary ion mass spectroscopy (SIMS), which is relatively expensive and can only be used for homogeneous regions larger than a few ten micrometers, and on the other hand wet chemical decoration of doped regions, which is unreliable as the results can vary even for identical structures on the same sample [13, 14].

A method for quantification of implant or carrier concentration on small areas of tens of nanometers diameter was lacking for decades. Research on dopant profiling methods with a high spatial resolution, e.g. scanning capacitance microscopy (SCM), has been ongoing for over 30 years. SCM was first developed in 1984 as a method to, amongst others, characterize video discs [15]. Nevertheless, state-of-the-art dopant profiling methods yet do not meet the high demands of recent technology. However, scanning probe techniques involve complex evaluation of scan results, which so far did not allow a direct and

reliable extraction of dopant type and dopant density.
This thesis aims at expanding the available scanning probe methods (SPM) to close this still existing gap. A theoretical background on dopant profiling methods is provided in section 2 with focus on high frequency (HF) network analysis and the physics behind the Metal-Oxide-Semiconductor (MOS) structure. Furthermore capacitance-voltage (C-V) characteristics under HF conditions are introduced and a special case for measurements in the GHz range is presented.
Section 3 gives an overview of state-of-the-art dopant profiling methods including a brief description of Scanning Microwave Microscopy (SMM) and the SMM setup. The chapter is summarized with a comparison of the methods on resolution, dopant type distinction and ability for quantitative measurements.
In section 4, the sample preparation is discussed and the finite elements method (FEM) model of the probe-sample interface is introduced. The model is used to optimize the HF AFM probes.
The SMM results are presented in section 5. First, the resolution of a SMM scan is investigated which involves the development of a method to obtain the effective tip diameter using GaN. Further, the resistivity in SMM is demonstrated to enable the calculation of absolute dopant densities. On the basis of fundamental investigations on SMM methodology, a method to obtain dopant type and densities from the SMM capacitance data is developed. Finally, the application of SMM on state-of-the-art semiconductor devices is demonstrated.
Section 6 summarizes the results and concludes the thesis.

2 Theoretical Background

2.1 Vector Network Analysis

The interpretation of SMM signals is based on network analysis. A network consists of a certain amount of ports. Each port is defined as a pair of terminals and represents a connection point to the network [16]. In a low frequency range, those ports can be characterized with hybrid (H-) parameters. In a classic HF network admittance (Y-) parameters are used. With increasing frequency, those parameters can hardly be measured accurately and generate problems in theoretic considerations. Therefore measurement of voltage and current at a perfect HF short would be necessary. For example in a waveguide the classical definitions of current, voltage and terminal pair do not apply. To find a solution for that problem, it is necessary to divide a wave on a transmission line into an incident and an output wave quantity [17]. A scattering (S-) parameter describes the relation between the incident and the output wave quantity. Thus, a network can be described through the scattering parameters of its ports. A scattering parameter S_{nm} is described through its indices n and m, where n and m are the corresponding port numbers. If $n = m$, the parameter describes the reflection from port m on port m when all other ports are terminated reflection-free. If $n \neq m$, the parameter describes the transmission from port m to port n, all other ports terminated reflection-free as well. As in the methods employed in this thesis only one port is used, this section will focus on the complex parameter $\underline{S}_{11}$, which describes the reflection from port 1 on port 1 [17]. At a known measurement frequency, $\underline{S}_{11}$ can be used to calculate the input impedance of the circuit. The relation is given by

$$\underline{S}_{11} = \frac{\underline{Z}_{in} - \underline{Z}_0}{\underline{Z}_{in} + \underline{Z}_0}, \tag{1}$$

where $\underline{Z}_{in}$ is the input impedance and $\underline{Z}_0$ the characteristic impedance of the network. As $\underline{Z}_{in}$ depends on the measurement equipment and the network connecting the device under test (DUT) to the vector network analyzer (VNA), the measured reflection $\underline{S}_{11,meas}$ has to be calibrated to extract the actual reflection r_{DUT} caused by the DUT. For a one-port network, the one-port error

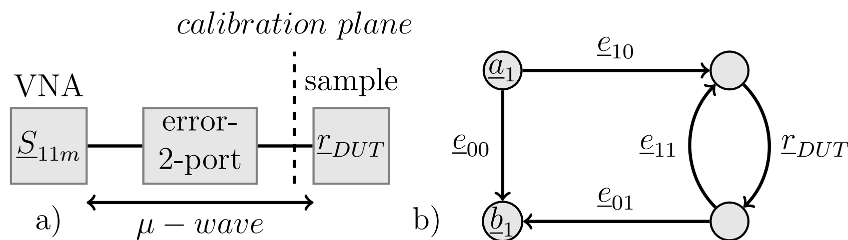

Figure 1: (a) Network reduced to the reflection $\underline{S}_{11m}$ measured at port 1, the actual reflection of the DUT $\underline{r}_{DUT}$ and the error two port describing the black-box network inbetween. (b) siganl flow chart showing which error parameter describes which signal part. $\underline{a}_1$ and $\underline{b}_1$ are the output and incident wave quantities.

model shown in fig. 1 is used to describe the relation between the measured $\underline{S}_{11,meas}$ and the reflection r_{DUT} [17]. Figure 1 (a) shows the circuit considering the error model. The VNA is connected to the DUT through a network of transmission lines and parasitic components, which can be described as an error 2-port. In fig. 1 (b) $\underline{S}_{11,meas}$ is described through the output wave quantity a_1 and the incident wave quantity b_1 with $S_{11m} = b_1/a_1$. Following the signal flow chart in fig. 1 (b), $\underline{S}_{11,meas}$ can be expressed as

$$\underline{S}_{11,meas} = \underline{e}_{00} + \frac{\underline{e}_{10}\underline{e}_{01}}{1 - \underline{e}_{11}\underline{r}_{DUT}}\underline{r}_{DUT}. \tag{2}$$

A common method to calibrate $\underline{S}_{11}$ is to use the open short load (OSL) calibration [17, 18]. Therefore, three standards, open, short and load are applied to the measurement setup. They do have precisely defined parameters and, therefore, allow a very accurate calculation of the four error parameters $\underline{e}_{00}$, $\underline{e}_{10}$, $\underline{e}_{01}$ and $\underline{e}_{11}$. In some cases, like in SMM, the interface required for the calibration plane is not accessible to plug calibration standards. In general, the calculation of the error parameters can be done with other known impedances accessible at the calibration plane as well. Then, accuracy of the calibration strongly depends on the accuracy of those impedances. For the calculation of four error parameters, a minimum of three impedances need to be measured. Equation 2 can be converted to

$$\underline{S}_{11,meas} = (\underline{e}_{10}\underline{e}_{01} - \underline{e}_{00}\underline{e}_{11})\underline{r}_{DUT} + \underline{e}_{00} + \underline{e}_{11}\underline{r}_{DUT}\underline{S}_{11,meas}, \tag{3}$$

leading to a system of equations. This system can be solved analytically for n=3 measured impedances and numerically for n>3 measurements.

$$\begin{pmatrix} \underline{S}_{11,meas1} \\ \underline{S}_{11,meas2} \\ \dots \\ \underline{S}_{11,meas-n} \end{pmatrix} = \begin{pmatrix} \underline{r}_{DUT1} & 1 & \underline{r}_{DUT1}\underline{S}_{11,meas1} \\ \underline{r}_{DUT2} & 1 & \underline{r}_{DUT2}\underline{S}_{11,meas2} \\ \dots & \dots & \dots \\ \underline{r}_{DUTn} & 1 & \underline{r}_{DUTn}\underline{S}_{11,meas-n} \end{pmatrix} \begin{pmatrix} \underline{e}_{10}\underline{e}_{01} - \underline{e}_{00}\underline{e}_{11} \\ \underline{e}_{00} \\ \underline{e}_{11} \end{pmatrix} \tag{4}$$

The possibility to calculate the error parameters without calibration standards enables the calibration plane to be located at an interface not accessible for standard calibration standards. In SMM, for example, the calibration plane can therefore be located directly at the tip-sample interface. Once $\underline{r}_{DUT}$ is calculated, the capacitance and conductance can be extracted. The main idea which the high frequency SPM methods extracting dopant information are based on, is to use the relation between the reflection $\underline{r}$ and the complex impedance $\underline{Z}$ of the investigated structure. The relation between $\underline{r}_{DUT}$ and sample impedance $\underline{Z}_{DUT}$ is given by

$$\underline{r} = \frac{\underline{Z}_{DUT} - \underline{Z_0}}{\underline{Z}_{DUT} + \underline{Z_0}}, \tag{5}$$

where $\underline{Z_0}$ is the characteristic impedance of the circuit [16]. This thesis deals with networks with a characteristic impedance of $\underline{Z_0} = 50\ \Omega$. Transforming $\underline{Z}_{DUT}$ to an admittance $\underline{Y}_{DUT}$

$$\underline{Y}_{DUT} = \frac{1}{\underline{Z}_{DUT}}, \tag{6}$$

the capacitance can be calculated from $\underline{Y}_{DUT}$.

$$\underline{Y}_{DUT} = G + j\omega C \tag{7}$$

A simple example with a pure capacitance of 1.99 fF, a typical value in SMM measurement range, and no conductive or resistive part is calculated to show the importance of the right location of the calibration plane. The frequency is

chosen at the SMM maximum frequency of 20 GHz. $\underline{Z}_{DUT}$ can be calculated directly from C, because the conductive part is neglected in this example.

$$\underline{Z}_{DUT} = \frac{1}{j\omega C} = \frac{1}{j2\pi \times 20\ GHz 1.99\ fF} = -4000j\ \Omega \tag{8}$$

Figure 2 shows a Smith chart, where $\underline{Z}_{DUT}$ is marked in blue. To be able to mark $\underline{Z}_{DUT}$ in the Smith chart, it is normalized to 50 Ω.

$$\underline{z}_{DUT} = \frac{\underline{Z}_{DUT}}{\underline{Z}_0} = \frac{-4000j\ \Omega}{50\ \Omega} = -80j \tag{9}$$

Besides the impedance and admittance, the influence of the length of a transmission line can be analyzed in a Smith chart as well. The outer scale ring of the Smith chart shows the change of phase by moving towards the generator, which is in our case the VNA. The length is normalized to the wavelength λ. With a frequency of 20 GHz, λ equals 14,99 mm in a perfect conductor. If the calibration plane would be dislocated by 3.75 mm, even with a transmission line perfectly matched to 50 Ω, this would mean a dislocation of 0.25 λ. The phase shift by this dislocation is marked in red in fig. 2. In the Smith chart, the impedance after dislocation of $\underline{z}_{dislocated} = 0.0125j$ is marked in red as well. The dislocated value is in the inductive part of the Smith chart. The calculated result is now an inductance.

$$L = \frac{\underline{z}_{dislocated}}{j\omega}\underline{Z}_0 = \frac{0.0125j}{j2\pi \times 20\ GHz}50\ \Omega = 4.97\ pH \tag{10}$$

This shows that it is crucial to locate the calibration plane directly at the DUT to get reliable results, as dislocations can change the measurement results significantly.

2.2 Metal Oxide Semiconductor Structure

2.2.1 States of a MOS-Structure

Understanding physical and electrical behavior of a MOS-structure is essential for the SPM methods SCM, SMM and scanning microwave impedance

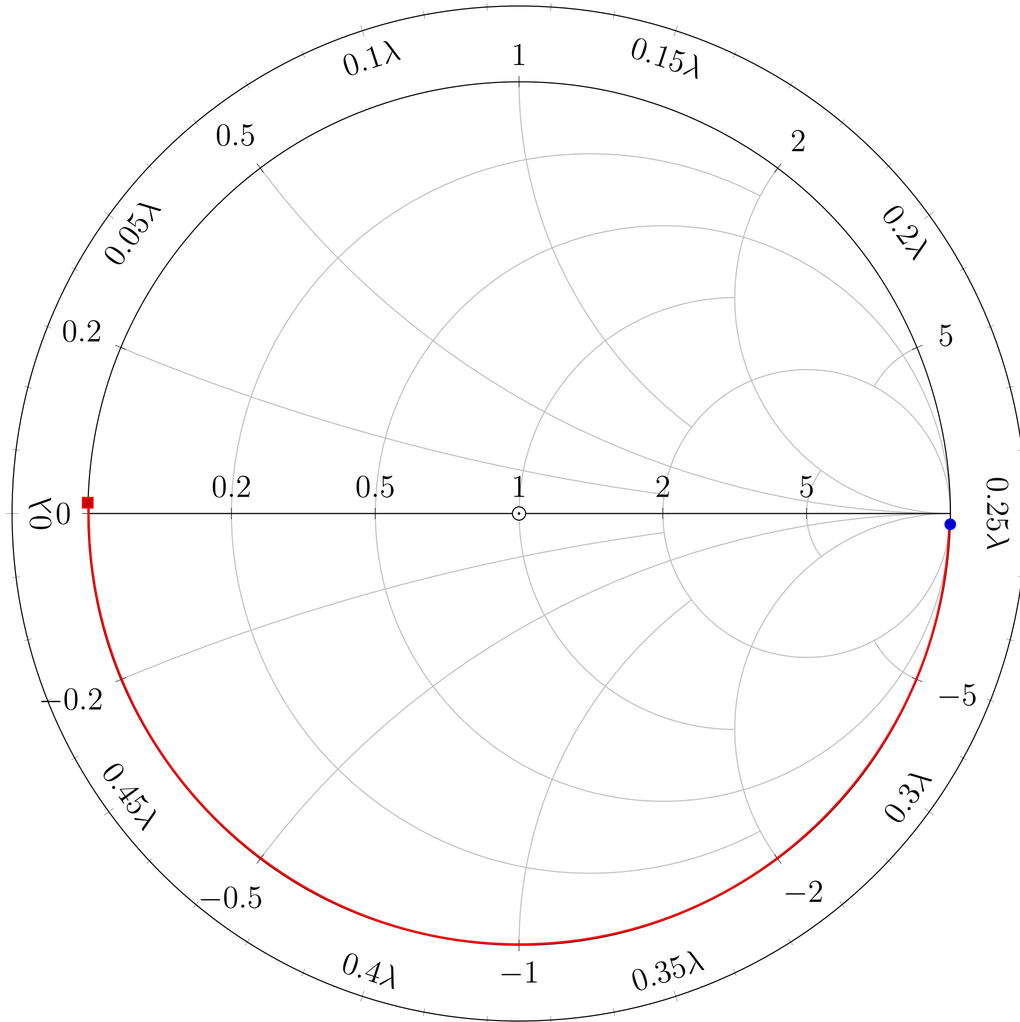

Figure 2: The smith chart shows the real part at the x-axis. The imaginary part can be read on the outer circle. In impedance mode, the upper half shows inductive values and the lower half capacitive ones. In admittance mode, the upper half is capacitive and the lower half inductive. All values are normalized to the characteristic impedance $\underline{Z}_0$, the frequency f and the wavelength λ. The outer circle shows the phase shift by moving towards the generator. The half circle marked in red shows the transition from $\underline{z} = -80j$ (blue) to $\underline{z} = 0.0125j$ (red) by moving $\lambda/4$ towards the generator.

microscopy (SMIM), as they probe a MOS-structure consisting of the metallic tip, the native oxide and the investigated semiconductor. Therefore, the MOS-structure dependencies relevant for these scanning probe methods will be discussed in this section. The MOS-structure can seize different states.

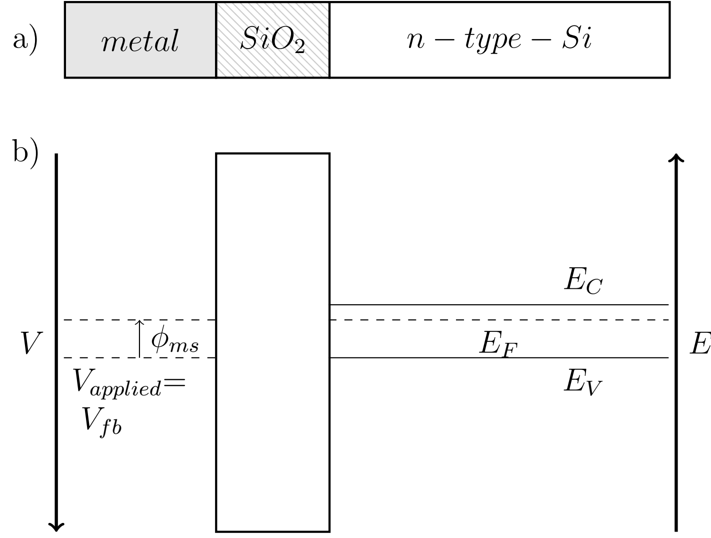

Figure 3: (a) Schematics of an n-type silicon MOS-structure. (b) Corresponding band diagram. $V_{applied} = V_{fb}$ compensates ϕ_{ms}, consequently the bands are flat.

Figure 3 shows the MOS-structure with n-doped silicon as a semiconductor in flat-band condition. An ideal metal-insulator-semiconductor (MIS) structure is in thermal equilibrium at a bias of 0 V. All bands are flat under these circumstances. For a real MOS-structure, the work function difference between the semiconductor and the metal has to be considered [19]. The work function difference can be expressed as

$$\phi_{ms} = \phi_m - (\chi/q + E_g/2q - \psi_{Bn}) \tag{11}$$

for n-type semiconductors and

$$\phi_{ms} = \phi_m - (\chi/q + E_g/2q + \psi_{Bp}) \tag{12}$$

for p-type semiconductors with E_g being the bandgap and χ the electron affinity of the semiconductor. The Fermi potentials with respect to the midgap ψ_{Bn} and ψ_{Bp} can be estimated by

$$\psi_{Bn} = \frac{kT}{q} ln(\frac{N_D}{n_i}) \tag{13}$$

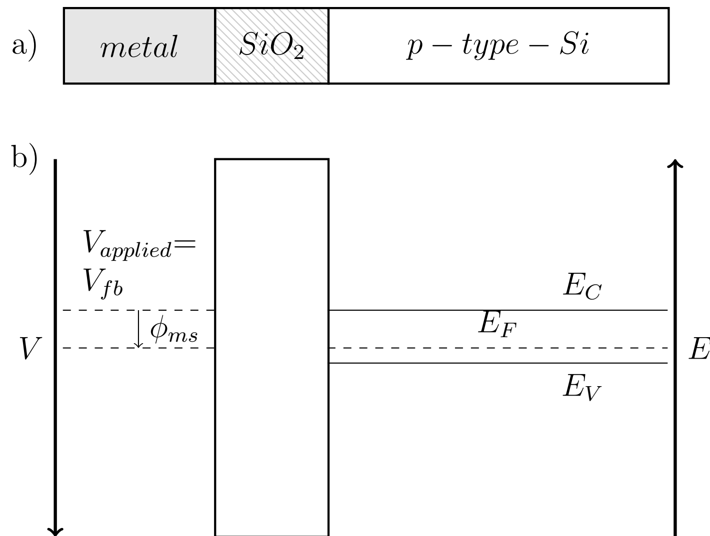

Figure 4: (a) Schematics of a p-type silicon MOS-structure. (b) Corresponding band diagram. $V_{applied} = V_{fb}$ compensates ϕ_{ms}, consequently the bands are flat.

for n-type and

$$\psi_{Bp} = \frac{kT}{q} ln(\frac{N_A}{n_i}) \tag{14}$$

for p-type, with donor and acceptor densities N_D and N_A, respectively, n_i the intrinsic carrier density, k the Boltzmann constant, T the temperature and q the elementary charge [19, 20]. In analogy, fig. 4 shows the band diagram of p-type silicon at flat-band condition. By applying a bias to the metal, the majority carriers can be accumulated to the semiconductor surface. For n-type Si, a bias larger than the flatband voltage V_{fb} $V_{bias} > V_{fb}$ has to be applied to accumulate the charges as shown in fig. 5.
By applying a positive voltage to the semiconductor interface, the bands bend downwards and allow the negative charges in the conduction band to be accumulated to the semiconductor surface. The accumulation case for p-type Si is shown in fig. 6. A negative voltage is applied to the structure bending the bands of the semiconductor upwards. The positive charges can accumulate due to the lift in valence band. Two additional cases would have to be considered in low frequency behavior of a MOS-structure, depletion and inversion.

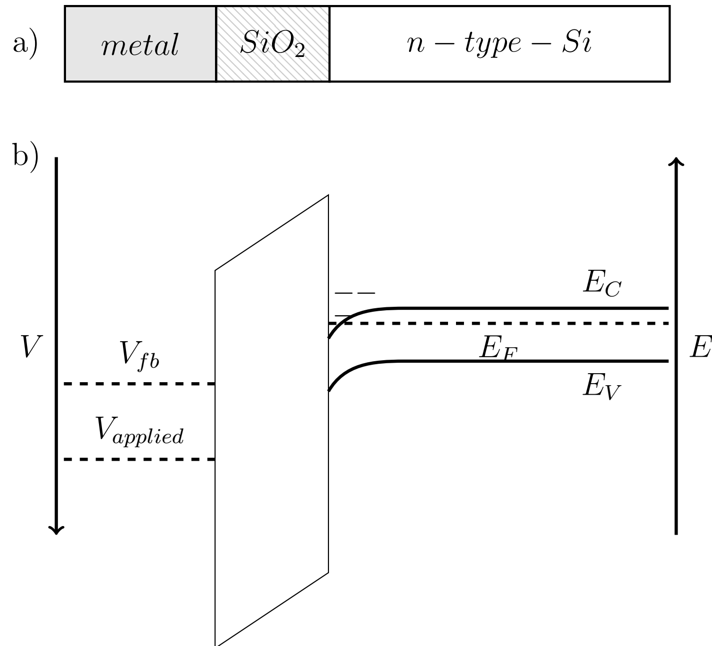

Figure 5: (a) Schematics of an n-type silicon MOS-structure. (b) Corresponding band diagram. As $V_{applied} > V_{fb}$, the bands bend downward at the Si-surface leading to an accumulation of electrons.

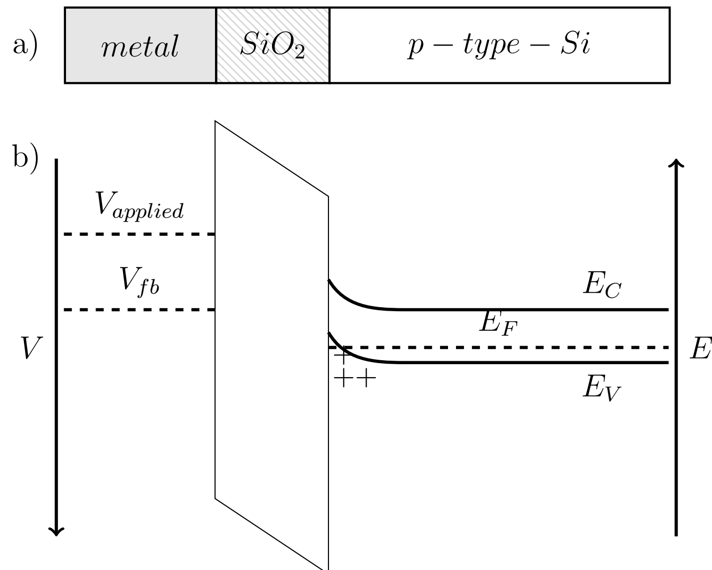

Figure 6: (a) Schematics of a p-type silicon MOS-structure. (b) Corresponding band diagram. As $V_{applied} < V_{fb}$, the bands bend upward at the Si-surface leading to a accumulation of holes.

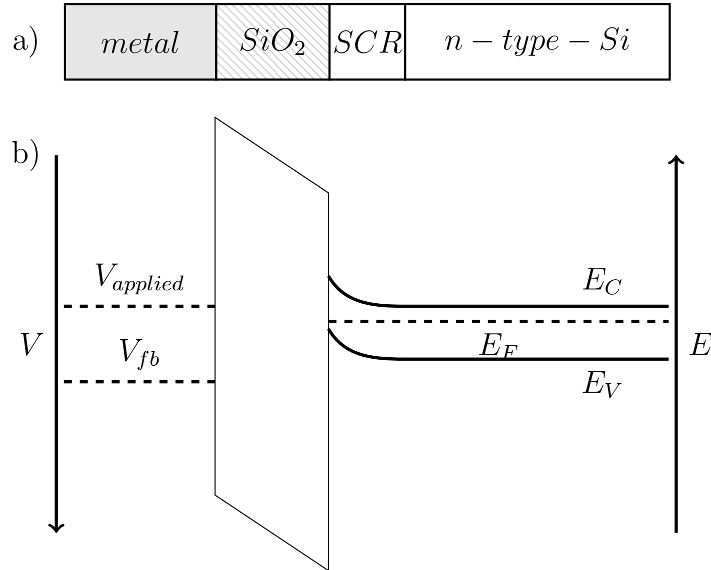

Figure 7: (a) Schematics of an n-type silicon MOS-structure. (b) Corresponding band diagram. As $V_{applied} < V_{fb}$, the bands bend upward at the Si-surface leading to a depletion of electrons. This depletion leads to a SCR below the surface indicated in (a).

As inversion case is not relevant in high frequency characteristics, only the depletion has to be taken into account. The charge carriers in n- and p-type Si can be depleted from the semiconductor surface by applying a negative, respectively positive, voltage to the metal. Figure 7 shows a negatively biased n-type MOS-structure. Due to the negative bias, the bands bend upward and the negative carriers are depleted from the semiconductor surface. The depletion of carriers creates a space charge region (SCR) below the oxide. Figure 8 shows the depletion case for a p-type semiconductor, where a positive bias is applied to deplete the holes from the semiconductor surface. The width of the SCR W_d depends on the potential ϕ_s at the semiconductor surface,

$$W_d = \sqrt{\frac{2\epsilon_{Si}\phi_s}{qN_x}} \tag{15}$$

with $N_X = N_D$ for n-type and $N_X = N_A$ for p-type semiconductors, respectively [20]. Whereas W_d is dependent on ϕ_s, it reaches a maximum at

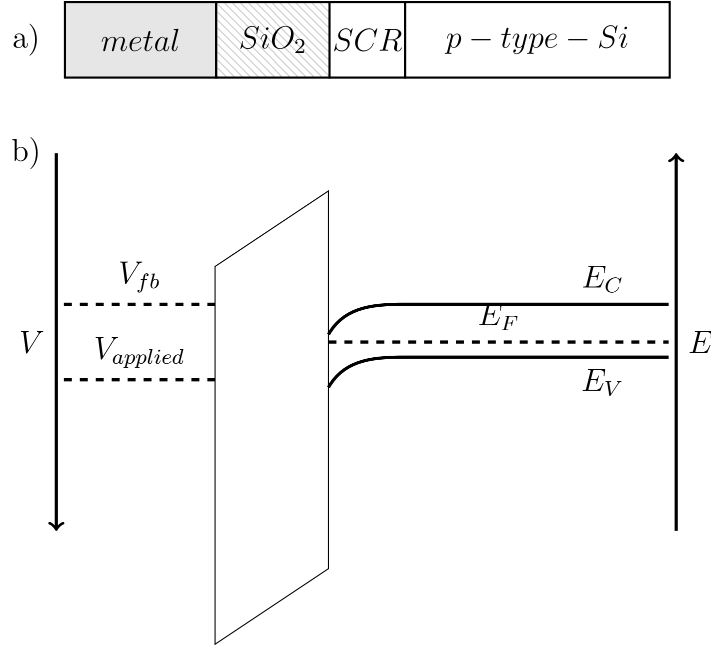

Figure 8: (a) Schematics of a p-type silicon MOS-structure. (b) Corresponding band diagram. As $V_{applied} > V_{fb}$, the bands bend downward at the Si-surface leading to a depletion of holes. This depletion leads to a SCR below the surface indicated in (a).

$\phi_s = 2\psi_{Bn/p}$ [19,20]. Considering eqs. (13) to (15), the maximum width of the SCR is

$$W_{d\ max} = \sqrt{\frac{4\epsilon_{Si} kTln(N_{D/A}/n_i)}{q^2 N_{D/A}}}. \tag{16}$$

2.2.2 Surface Potential Dependencies

It can be calculated at which value the potential ϕ_s reaches the states of accumulation, flatband and depletion. Nonetheless, it is hard to predict which corresponding bias to apply in order to achieve the respective surface potential, e.g. flatband potential, as the surface potential depends on various other potentials, like contact potentials, intrinsic potentials etc. A simple structure as in a typical measurement case for SMM and SCM, is shown in fig. 9. Following Kirchhoff's mesh rule, the relation between the potentials within the

MOS structure and the voltage V_{TS} applied between tip and backside metal is given by

$$V_{TS} = -\phi_{ms} - \phi_{ox} - \phi_s + \phi_i + \phi_c \tag{17}$$

[19, 21]. Solved for the surface potential ϕ_s, the result is

$$\phi_s = -V_{TS} - \phi_{ms} - \phi_{ox} + \phi_i + \phi_c. \tag{18}$$

The metal semiconductor work function difference ϕ_{ms}, and the simultaneously the backside contact potential ϕ_c, can be calculated using equations eqs. (11) and (12) and the built-in voltage $\phi_i = \frac{kT}{q}ln(\frac{N_{A2}}{N_A})$ [21]. Inserting those equations for the potentials leads to the dependencies shown in eqs. 19.

$$\begin{aligned}
\phi_s &= -V_{TS} - \phi_{ox} + (\frac{kT}{q}ln(\frac{N_{A2}}{N_{A1}})) + (\phi_{bm} - (\chi + E_g/2q + \frac{kT}{q}ln(\frac{N_{A2}}{n_i}))) \\
&\quad -(\phi_m - (\chi + E_g/2q + \frac{kT}{q}ln(\frac{N_{A1}}{n_i}))) \\
&= -V_{TS} - \phi_{ox} + \phi_{bm} - \phi_m + \frac{kT}{q}(-ln(\frac{N_{A2}}{N_{A1}}) - ln(\frac{N_{A2}}{n_i}) + ln(\frac{N_{A1}}{n_i})) \\
&= -V_{TS} - \phi_{ox} + \phi_{bm} - \phi_m + 2\frac{kT}{q}ln(\frac{N_{A1}}{N_{A2}})
\end{aligned} \tag{19}$$

The metal on both tip and backside is usually known, hence, are the corresponding metal work functions ϕ_m and ϕ_{bm}. The voltage drop ϕ_{ox} depends on the oxide thickness and the applied voltage. The term $2\frac{kT}{q}ln(\frac{N_{A1}}{N_{A2}})$ shows a strong dependency on the surface and substrate dopant densities N_{A1} and N_{A2}. To get an estimation on the influence of these dopant densities, a short example with typical dopant densities is calculated here. A typical substrate density could be $N_{A2} = 10^{15} atoms\ cm^{-3}$ and the density of an implant at the surface $N_{A1} = 10^{19} atoms\ cm^{-3}$, for instance. With an estimated temperature voltage of $\frac{kT}{q} = 26\ mV$ at room temperature the equation leads to $2 * 26mV * ln(10^4) = 0,479\ V$, while the term becomes 0 for $N_{A1} = N_{A2}$. This shows how the dopant densities within the semiconductor do influence the surface potential. This is important if different dopant densities in the

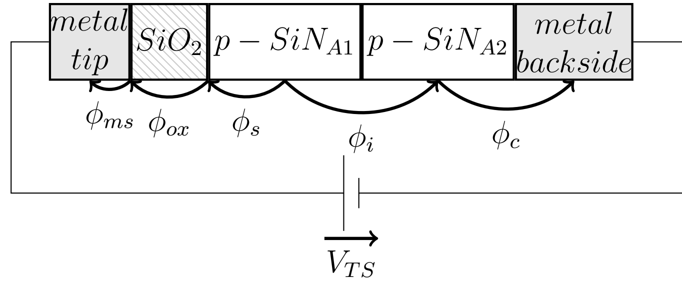

Figure 9: Voltages and potentials in a simple MOS-structure in measurement case. Tip metal, oxide, doped silicon, a differently doped substrate and the backside contact are considered. V_{TS} is applied beweteen the tip and the substate, respective potentials are metal semicondutor work function difference ϕ_{ms}, oxide potential ϕ_{ox}, surfce potential ϕ_s, build in potential ϕ_i and contact potential ϕ_c.

same sample are measured under the same bias condition. As the only tunable parameter in this equation is the bias voltage V_{TS}, it has to be chosen accordingly to reach the respective states. For accumulation (depletion) state, it has to be chosen positive (negative) enough for the potentials within the semiconductor to become negligible. As for all states in between, including flatband condition, the potentials within the MOS-structure have to be taken into account. For structures with thin oxides this leads to a strong deviation from flatband if the dopant densities vary. If, like in the given example, the applied voltage is chosen accordingly to measure $N_{A1} = N_{A2} = 10^{15} atoms\ cm^{-3}$ at flatband condition, a $N_{A1} = 10^{15} atoms\ cm^{-3}$ Si will be in accumulation state under those conditions.

2.2.3 Capacitance Voltage Characteristics

SCM, SMM and SMIM are probing dopant densities and are mainly based on the density dependent capacitive behavior of the MOS-structure. They use different techniques to process qualitative images showing signal contrast between different dopant types and densities. In order to interpret those images correctly, it is necessary to understand the capacitive high frequency behavior of a MOS structure. The HF C-V characteristics provide an accurate approach to describe this capacitive behavior. The C-V characteristics are shown schemat-

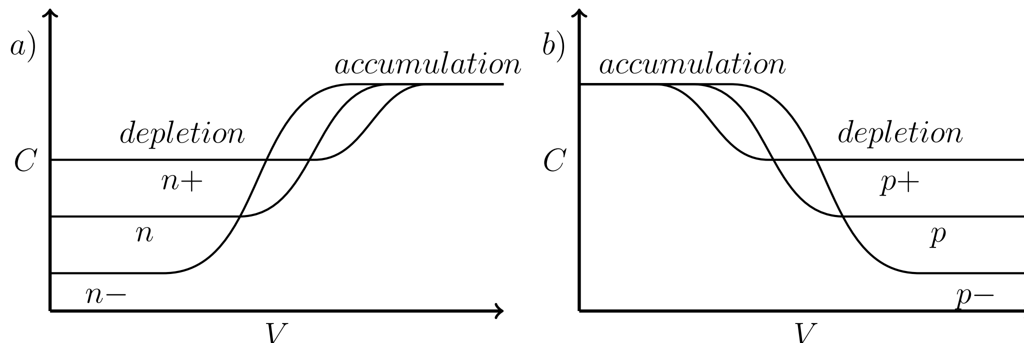

Figure 10: High frequency C-V characteristics for (a) n- and (b) p-type silicon. The dopant density dependent influence of metal-semiconductor work function difference ϕ_{ms} on flatband voltage shifts the curves. The shift is schematically exaggerated to demonstrate the principle.

ically in fig. 10. For both p- and n-type semiconductors the capacitance in accumulation case is close to the oxide capacitance [19–21]. Therefore, the accumulation capacities, independent of doping type and density, all reach the oxide capacitance level as shown schematically in fig. 10. As demonstrated in fig. 5, an n-type semiconductor, depicted in fig. 10 (a), reaches accumulation state when a voltage larger than V_{fb} is applied. The p-type semiconductor shown in fig. 10 (b) reaches accumulation state when biased smaller than V_{fb} (see fig. 6). The depletion state is reached by applying a negative, (positive) voltage relative to V_{fb} for n-type (p-type) semiconductors (see figs. 5 and 6). The depletion capacitance depends on the width of the SCR. The SCR forms a capacitance in series to the oxide capacitance. The MOS-structure reaches its minimum capacitance C_{dmin} when the SCR gets maximal at $W_d = W_{d\ max}$ [19]. C_{dmin} can then be calculated from

$$C_{dmin} = A * \frac{\epsilon_i \epsilon_s}{\epsilon_i W_{d\ max} + \epsilon_s d_i}, \tag{20}$$

with ϵ_i and ϵ_s being the respective insulator and semiconductor permittivities, d_i the thickness of the insulator and A the capacitor area. As shown by eqs. (16) and (20), the depletion capacitance minimum decreases with decreasing dopant density. The variation of flatband voltage is due to the different dopant types and densities influencing the metal work function difference as shown in eqs. (11) to (14). Consequently the flatband voltage of n-type

semiconductors increases with dopant density whereas it decreases for p-type semiconductors as depicted schematically in fig. 10.

2.2.4 High Frequency Models

Besides the standard C-V characteristics, there is a further effect influencing the AFM based dopant characterization methods not considered in standard literature. It can be observed that in SMM accumulation capacitance does not always reach oxide capacitance level [22]. This effect is known from C-V characteristics of a highly resistive substrates, where it occurs far below the GHz frequencies [23–28]. The effect is frequency dependent, thus influencing measurements at higher frequencies stronger than those at lower frequencies [26, 29]. Furthermore, the effect is dependent on the dopant density, occurring earlier at low dopant densities [23, 24]. Figure 11 schematically illustrates the reduced accumulation capacitance at low dopant densities. The main reason for this reduced accumulation capacitance was found to be the increase of series resistance by decrease of dopant density [26]. Therefore, Rejeiba et al. developed a model allowing to tune the different influence factors like parallel and series resistance of decreasing dopant density individually and thus investigate their effects on C-V and conductance-voltage (G-V) independently [26]. Rong et al. suggest that this dependency would be due to the dielectric relaxation time [24]. Thereby the frequency dependence could be explained as well, because once the frequency is close enough to be in the order of the relaxation time

$$\theta = \rho_{Si}(N_{D/A})\epsilon_{Si}, \tag{21}$$

where ρ_{Si} is the conductivity of silicon and ϵ_{Si} the permittivity of silicon, the majority carriers are no longer able to follow the frequency properly [24]. This observation is consistent with a model introduced by Luna-Lopez et al., where the contribution of the large series resistance on the time constant is pronounced as well [29].

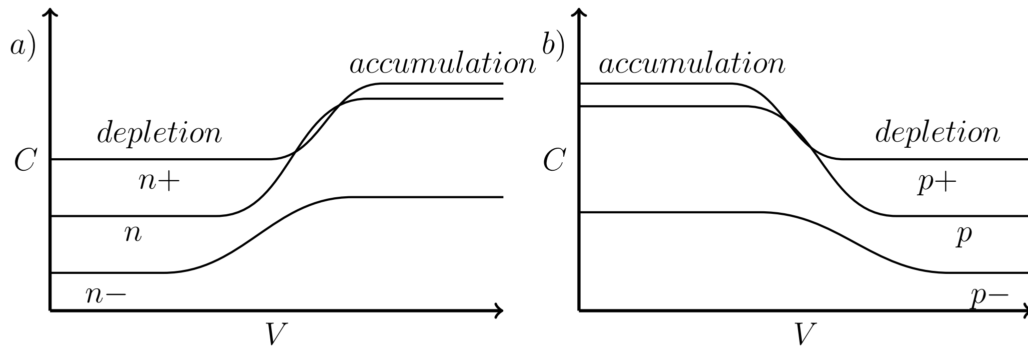

Figure 11: High frequency (GHz-range) C-V characteristics for (a) n- and (b) p-type silicon. The reduction of accumulation capacitance with decreasing dopant density is shown schemetically, starting slighty at mid range dopant densities (n, p) and causing the largest reduction for low dopant densities (n-, p-). The carrier mobility dependency of this effect results in a stronger reduction for p-doped semiconductors.

3 Methods for Dopant Profiling

In 1965, Moore's law predicted that the integration scale would increases by a factor of four every two to three years [1]. This is still valid and drives the need for high resolution methods to reliably characterize dopant distributions within semiconductor devices. This includes e.g. contact implants of a few ten nanometers. AFM based methods meet the high resolution requirements. They allow to image dopant distribution in semiconductor devices on nanoscale. State-of-the-art SPM techniques are discussed in the following chapter.

3.1 Basics of Atomic Force Microscopy and Electrostatic Force Microscopy

Scanning tunneling microscopy (STM) was the first SPM method, developed by Binnig et al. in 1981 [30]. It already provided a good method to image the topography of a sample at a nanoscale resolution, but it was limited to conductive material only. In 1985, its inventors introduced another SPM method, called atomic force microscopy (AFM). This new method allowed the investigation of both conductive and non-conductive material, leading to a wider field of application. The first AFM enabled the characterization of sample topography by detecting small forces between the AFM tip and the sample [31]. There are three basic AFM modes: Contact mode, AC or tapping mode, and non-contact mode. Schematics of the contact mode AFM are shown in fig. 12.

In contact mode AFM, the AFM tip is constantly in contact with the sample surface while scanning the defined area. A change in topography leads to a deflection of the AFM cantilever. There are several ways to sense the cantilever deflection. The most common way is to sense deflection with an optical sensor, like shown in fig. 12. An optical laser beam is reflected from the cantilever backside and detected by a quadrant photo diode. This photo diode detects deviations in cantilever deflection (vertical) and friction (lateral) from a certain setpoint. These setpoint deviations in deflection are fed into a feedback loop controlling the AFM piezoelectric z-scanner. The feedback loop corrects the z-position by means of piezoelectric actuators until the deviation

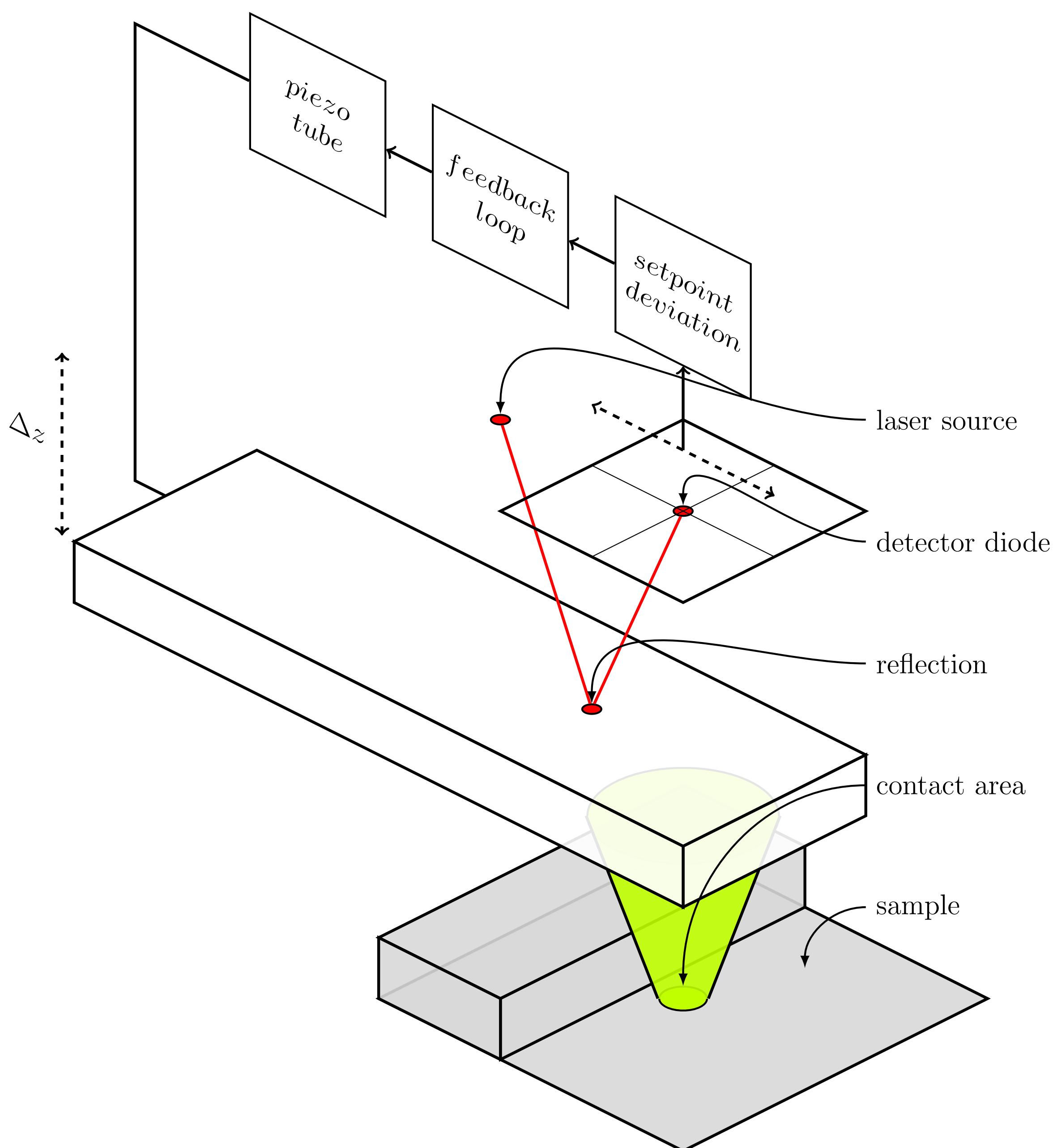

Figure 12: AFM contact mode schematics. The cantilever deflection is detected optically with laser and quadrant diode. The setpoint deviation is tracked and fed back into a feedback loop controlling the piezo tube. The piezo tube is attached to the cantilever and controlled to level out the deviation.

from the setpoint is compensated. Thus, the cantilever deflection is held to one setpoint and the AFM tip stays in contact to the sample with constant force load.
An alternative way to sense the cantilever deflection is to use a piezoelectric cantilever [32]. In this case, a measurement bridge of piezoresistive implants in the cantilever is used to sense the deflection. The feedback loop works the same for both types of deflection detection.
There are different approaches for the x-, y- and z-piezoelectric scanners. In some AFMs they do move the sample or cantilever in all directions. In other AFM models, the movement of the x- and y- piezoelectric scanners is decoupled from the z-movement by scanning the sample in x- and y- direction and integrating the z-piezo in the cantilever holder.
Figure 13 shows the schematics of a tapping mode AFM. In contrast to contact AFM, the AFM tip is not constantly in contact with the sample, i.e. only taps the sample surface at a certain frequency. This frequency depends on the eigenfrequency of the used cantilever [31]. An AC bias slightly off the eigenfrequency is applied to a dither piezo oscillating the cantilever. The oscillation amplitude changes with a change in topography due to damping effects and deviations in amplitude are monitored using the quadrant photodiode. The feedback loop regulates the z-piezo to achieve the setpoint amplitude value [1].

Non-contact mode is the basis for some electrostatic force microscopy (EFM) approaches. The distance between sample surface and cantilever tip is kept constant during the whole measurement time, only varying due to the oscillation amplitude of the cantilever. The shift of the oscillation frequency due to the topography is tracked and adjusted by regulating the tip sample distance [1].
EFM probes electrostatic forces on the investigated samples. In semiconductor industry it is used to probe charges, voltages and potentials of semiconductor devices [33]. It can furthermore be used to measure the tip sample capacitance [34]. When AFM tip and sample are close enough for the electrostatic force to be considerable, the electrostatic force can be described as

$$F = \frac{1}{2} \frac{dC_{ts}}{dz} V_{ts}^2, \tag{22}$$

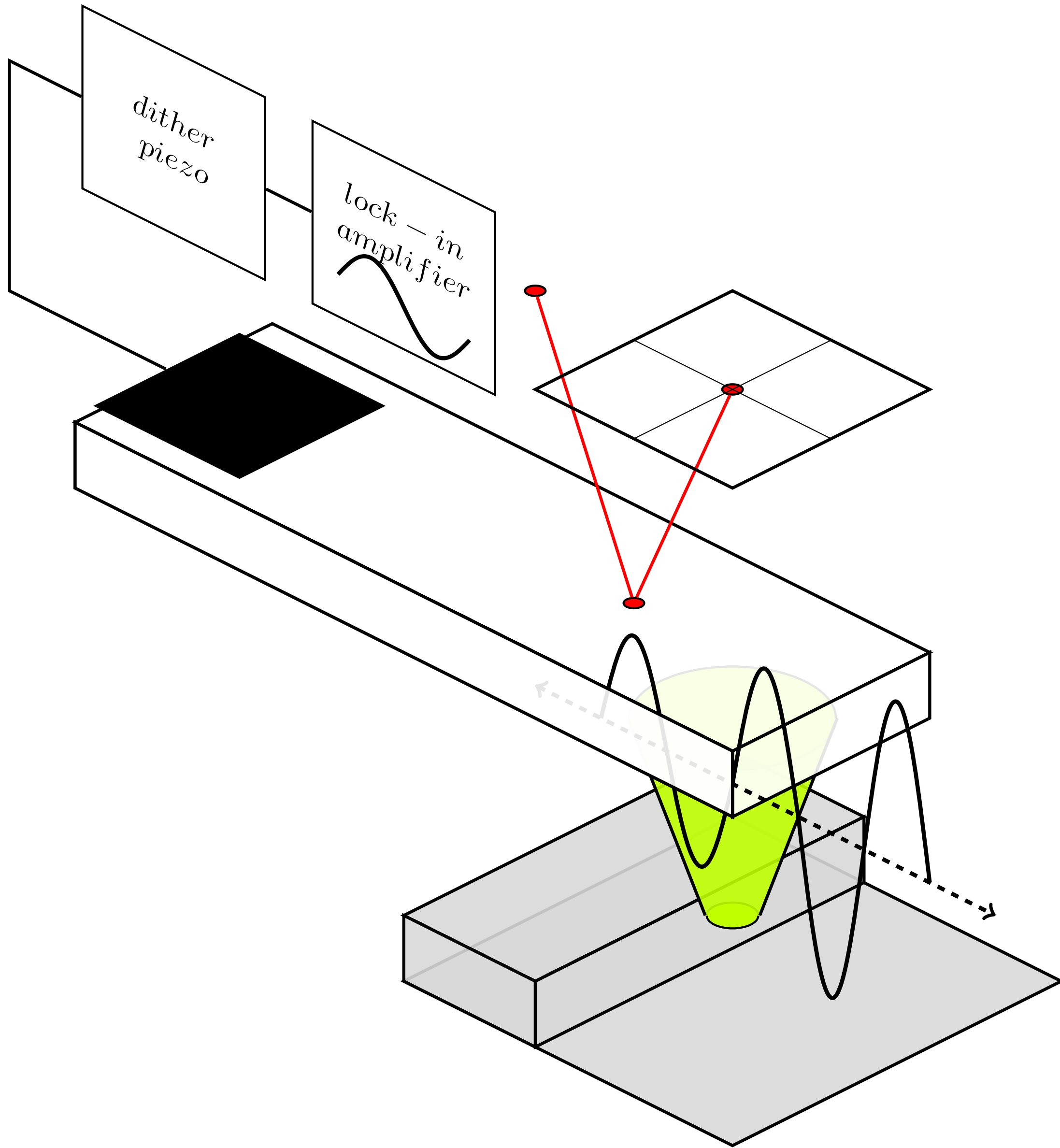

Figure 13: AFM tapping mode schematics. The feedback loop is similar to fig. 12. Additional to contact AFM, an AC bias generated in the lock-in amplifier is applied to oscillate the cantilever. Oscillation amlitude changes with topography. The laser deflection signal is fed back into the lock-in amplifier to track the oscillation amplitude and phase. The feedback loop adjusts the piezo tube (similar fig. 12) to keep setpoint amplitude.

with C_{ts} as the tip to sample capacitance and V_{ts} the voltage between tip and sample [33]. For a sample which is not operated, only the potentials resulting

from the applied static and dynamic voltages and the potential resulting from the work function difference between metal tip and semiconductor sample have to be considered for V_{ts}.

$$V_{ts} = V_{DC} - \phi_{ms} + V_{AC} \sin \Omega t \tag{23}$$

V_{DC} and V_{AC} are the DC and AC voltages applied to the AFM tip and the contact potential ϕ_{ms} can be calculated as shown in eqs. (11) and (12). With V_{ts} known, the electrostatic force can basically be decomposed into three terms, F_{DC}, F_{Ω} and $F_{2\Omega}$. F_{DC} is the part of the force that constantly bends the cantilever [33]. It is thus hard to detect, while F_{Ω} and $F_{2\Omega}$ can be detected at the respective harmonic with a lock-in detector. Considering eqs. (22) and (23) the term

$$F_{DC} = \frac{1}{2}\frac{dC_{ts}}{dz}[(V_{DC} - \phi_{ms})^2 + \frac{1}{2}V_{AC}^2] \tag{24}$$

describes this constant force [33]. At the AC frequency Ω the term

$$F_{\Omega} = \frac{dC_{ts}}{dz}(V_{DC} - \phi_{ms})V_{AC} \sin \Omega t \tag{25}$$

shows a linear dependency on the capacitive coupling dC/dz and the contact potential ϕ_{ms} [33]. The electrostatic force term at the second harmonic 2Ω is mainly dependent on the local capacitive coupling between tip and sample [33].

$$F_{2\Omega} = \frac{1}{4}\frac{dC_{ts}}{dz}V_{AC}^2 \cos 2\Omega t \tag{26}$$

As the second harmonic is independent of the constant voltages and potentials, it is well suited for dielectric quantification and further capacitive analysis [35–37]. This equation can be transformed to

$$\frac{dC_{ts}}{dz} = \frac{4F_{2\Omega}}{V_{AC}^2} \tag{27}$$

and integrated to extract information of the tip sample capacitance [34, 38].

3.2 Calibration Sample

The development of dopant profiling methods requires a proper understanding of the respective methods. Therefore, it is necessary to have a suitable sample to be able to characterize the expected and parasitic influences. To characterize the different dopant profiling techniques, a silicon die with a large amount of simultaneously measurable dopant densities in both p- and n-type is needed. Most available samples offer differently doped epi-layers, which are either p- or n-doped [34, 39, 40]. None of those epitaxial grown samples offer both dopant types in various densities. Therefore the Failure Analysis of Infineon Technologies AG developed a sample with both p- and n-type doped regions in close proximity [41]. Figure 14 shows an optical overview image of the sample sized 5.5 mm x 3.5 mm. It is basically structured in four areas. The first area consists of 20 fields besides each other, each field being doped with a certain dopant density. Table 1 shows the datasheet densities in the same order as the doped stripes on the sample, starting from lowly doped n-type on the left to highly doped n-type in the middle and continuing from highly doped p-type in the middle to lowly doped p-type on the right. The fields in area A are sized 100 μm x 500 μm, offering sufficient area to enable SIMS measurements. At each of the 20 fields in area A, SIMS measurements were performed to validate the implants. The results are included in table 1. At lower dopant densities, SIMS results were too noisy to exactly determine a density, but all intended values were within the noise amplitude. Area B contains 55 different fields with a width of 50 μm each. The important fields are field 20 to field 35. Those fields contain all 20 dopant densities in the same order as in area A. Area B is split in three rows. In all three rows, the 20 different dopant densities are implanted in steps with a pitch of 2.5 μm to each other. The width of the implants differs between the three rows. The upper implants are 2 μm wide, the implants in the middle 1 μm and the implants in the lowest row 0.5 μm. Area C is basically similar to area B with one addition. There are trenches to have a strong but defined topography within the doped regions. Area D contains the same implants like the other areas. They are crossed to have defined p/n junctions. If not explicitly mentioned, the 2 μm stripes in area B are studied in the experiments within this thesis.

Table 1: Dopant densities and types of the substrate and the 20 differently doped fields in area A. The p-type is boron doped, the n-type phosphor. The intended dopant densities and the results achieved with SIMS measurements in area A are shown.

Field	dopant type	intended dopant density (cm^{-3})	SIMS results (cm^{-3})
substrate	p-type	1×10^{15}	
1	n-type	4×10^{15}	4×10^{15}
2	n-type	1×10^{16}	1×10^{16}
3	n-type	4×10^{16}	4×10^{16}
4	n-type	1×10^{17}	1×10^{17}
5	n-type	4×10^{17}	4×10^{17}
6	n-type	1×10^{18}	1.1×10^{18}
7	n-type	4×10^{18}	5×10^{18}
8	n-type	1×10^{19}	1.2×10^{19}
9	n-type	4×10^{19}	5.5×10^{19}
10	n-type	1×10^{20}	1.5×10^{20}
11	p-type	1×10^{20}	9×10^{20}
12	p-type	4×10^{19}	8×10^{19}
13	p-type	1×10^{19}	1.4×10^{19}
14	p-type	4×10^{18}	5×10^{18}
15	p-type	1×10^{18}	1.2×10^{18}
16	p-type	4×10^{17}	3.5×10^{17}
17	p-type	1×10^{17}	1×10^{17}
18	p-type	4×10^{16}	4×10^{16}
19	p-type	1×10^{16}	1×10^{16}
20	p-type	4×10^{15}	4×10^{15}

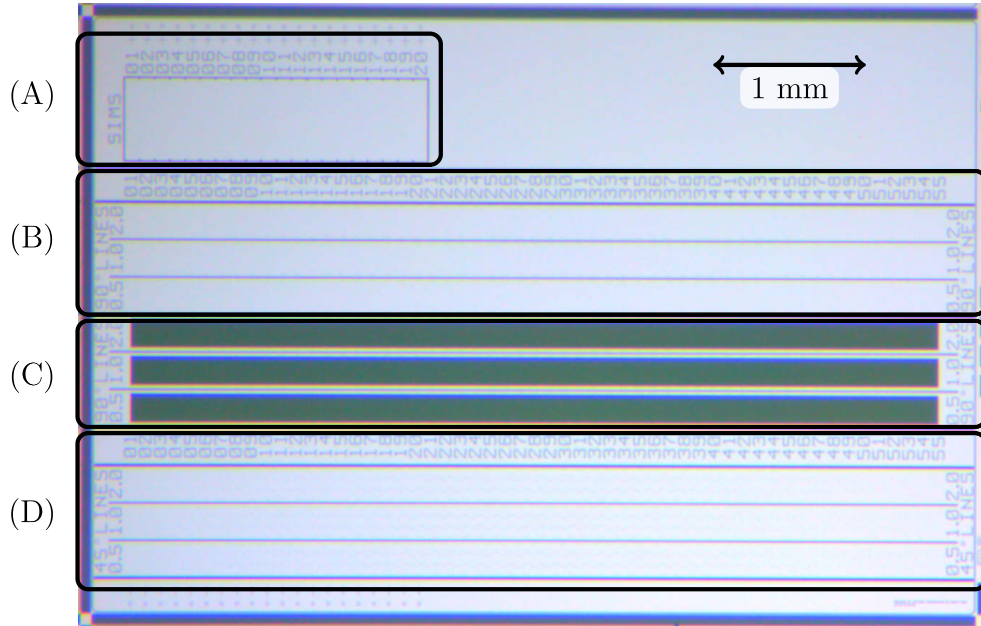

Figure 14: Calibration sample with different n- and p-type dopant densities. Area A contains 20 fields with the dopant density implants (see table 1) scaled large enough for SIMS. Area B contains 55 fields. Fields 1 to 19 contain as many dopant density stripe implants as their field number. 20 to 35 contain all dopant density stripe implants. Above 35 the number of dopant density stripe implants decreases again, until there is only one stripe left at field 55. Area C is basically a copy of area B with additional trenches. In area D the stripes with the p- and n-type dopants overlap to create p/n-junctions.

3.3 Scanning Microwave Microscopy

3.3.1 Principle

As an AFM based method, SMM has a wide range of applications in the analysis of biological, chemical and electronic samples [42–46]. The most important application of SMM is the two dimensional dopant profiling in semiconductor devices. SMM combines the high spatial resolution of an AFM with the possibility to apply a microwave through a conductive tip to the DUT [39]. Figure 15 schematically shows the setup used in SMM measurements. It is based on the AFM contact mode principle. A Vector Network Analyzer (VNA) applies a microwave to the conductive AFM tip. The microwave probes the DUT, which

is a MOS structure consisting of the conductive metallic AFM tip, the native grown oxide on top of the semiconductor and the semiconductor itself, see fig. 15. While part of the microwave is reflected at parasitic elements before and after the MOS structure and another part transmits through the sample, a part of the microwave is reflected at the MOS structure. The reflected part of the microwave is measured at the network analyzer as $\underline{S}_{11m}$. It is recorded during the measurement and can be used for further processing in order to determine electric sample properties quantitatively.

In addition to the network analyzer, a lock-in amplifier can be used to modulate the GHz-range HF signal with a kHz-range low frequency signal. Figure 16 illustrates how the modulation frequency drives the C-V characteristics between accumulation and depletion states to probe the slope of the C-V characteristics similar to classical SCM. This measurement technique is called dC/dV or $d\underline{S}_{11}/dV$ imaging and can be used for a number of quantitative and qualitative dopant profiling methods. Figure 17 shows a typical 2D $d\underline{S}_{11}/dV$ image of the p-n-calibration sample. The lock-in phase has been adjusted in order to distinguish between p- and n-type. With the calibration sample it was possible to adjust the phase shift to have the larger values for n-type dopants and smaller ones for p-type dopants. Such images of the calibration sample can be used to calibrate the image recorded on an unknown DUT with the same setup [39,41]. The easiest way is a comparison between a measurement at a calibration sample with well-known dopant densities and the DUT to calibrate the data [39]. However, the calibration itself cannot be validated with this method, because a shift of backside contact potential, which influences the semiconductor surface potential (see eq. (18)), would not be detected. Furthermore, a non-monotonic dependency of the dS_{11}/dV signal on the dopant density, as reported in literature [40, 41], would affect the comparison between calibration and test sample. Figure 17 shows the non-monotonic dependency on the dopant density as well. The n-type data behaves monotonously between 1x10^{16} atoms cm^{-3} and 10^{20} atoms cm^{-3} and the p-type data between 4x10^{16} atoms cm^{-3} and 10^{20} atoms cm^{-3}. Similarily, dS_{11}/dV also depends on the measurement frequency [40]. One possible root cause for this non-monotony is the reduced accumulation capacitance at low dopant densities, as schematically shown in fig. 16 and described in section 2.2.4. One approach to overcome the deficits in monotony

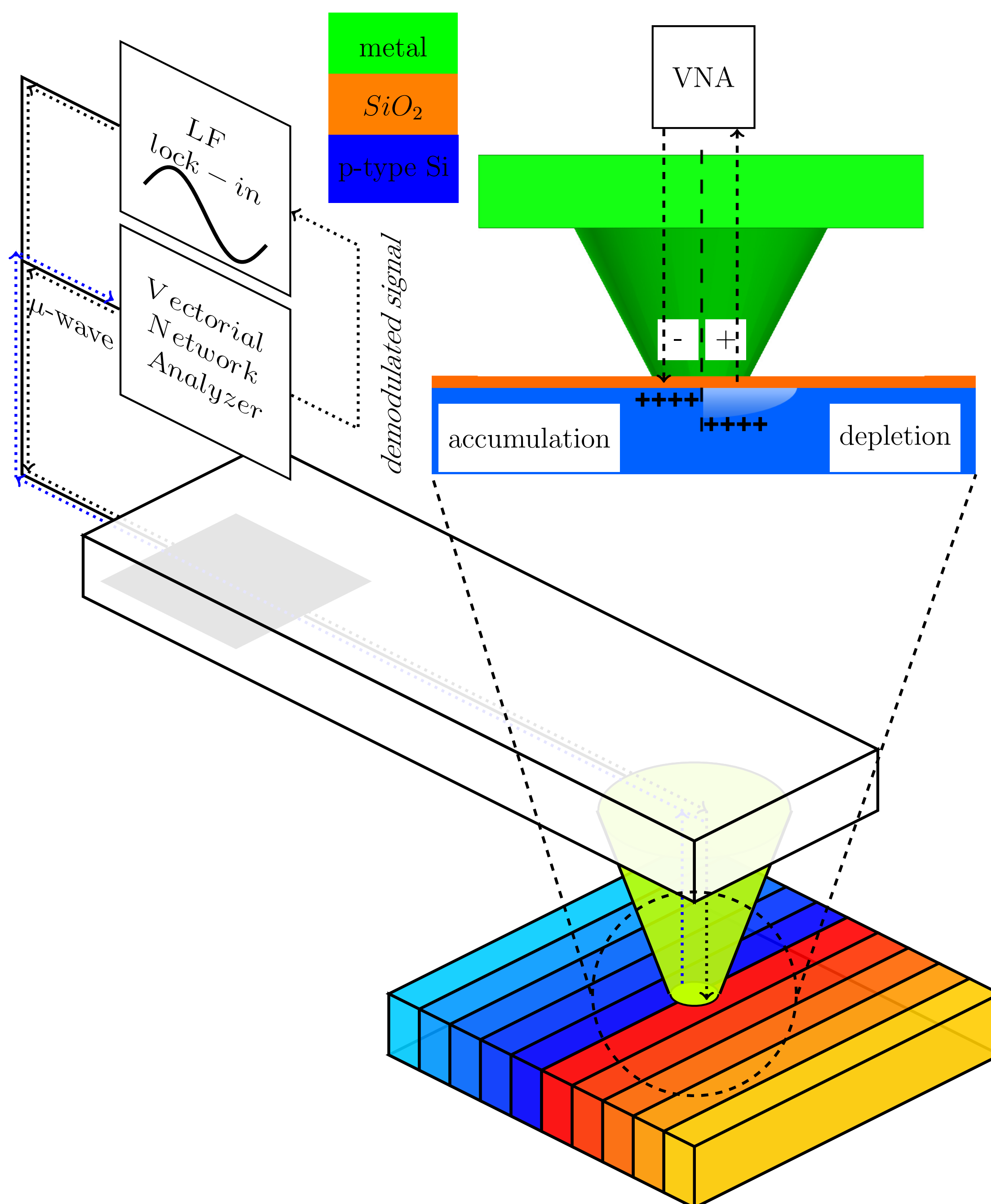

Figure 15: AFM SMM schematics. Additional to contact mode setup, a VNA and a lock-in amplifier are connected to the AFM tip to apply the microwave and modulation voltages. The reflected part of the microwave is measured at the VNA. The demodulated low frequent signal can be fed back into the lock-in amplifier. Additionally, a DC bias can be applied to the tip to accumulate or deplete charges at the semicondutor surface, as depicted in the inset.

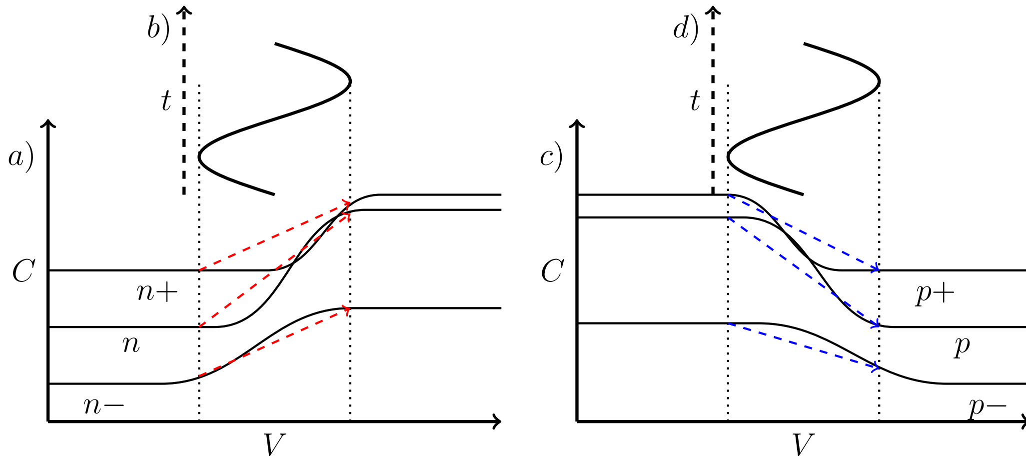

Figure 16: High frequency (GHz-range) C-V characteristics for (a) n- and (c) p-type silicon. The reduction of accumulation capacitance with decreasing dopant density is shown schematically, starting slightly at mid range dopant densities (n, p) and causing a big reduction for low dopant densities (n-, p-). The AC modulation voltage is indicated in (b) and (d). The red (n-type) and blue (p-type) arrows indicate the slope probed by the modulation voltage.

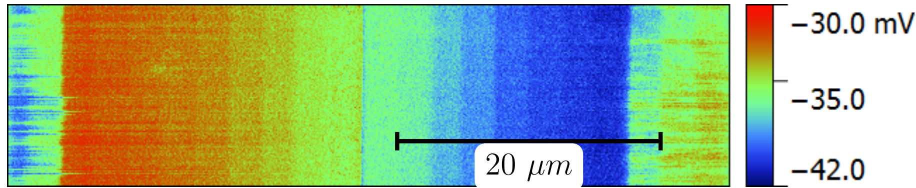

Figure 17: SMM $d\underline{S}_{11}/dV$ measurement of the calibration sample obtained at 4.56 GHz modulated with 3 V peak to peak at 90 kHz. The lock-in phase shift was adjusted to obtain higher values for n-type densities and lower values for p-type densities. To obtain positive and negative values as schematically shown in fig. 16, the lock-in phase offset needs to be adusted in addition to the phase shift.

and to enable the monitoring of deviations caused by a different backside contact potential is to measure the samples three times with different DC bias offsets [41]. This ensures a correct calibration. However, this method is still very time consuming and provides no solution to calculate dopant densities in case there are calibration deviations. Fortunately, SMM provides another opportunity to measure the sample without an additional lock-in amplifier and directly calibrate the reflected microwave into a capacitance and a resistance.

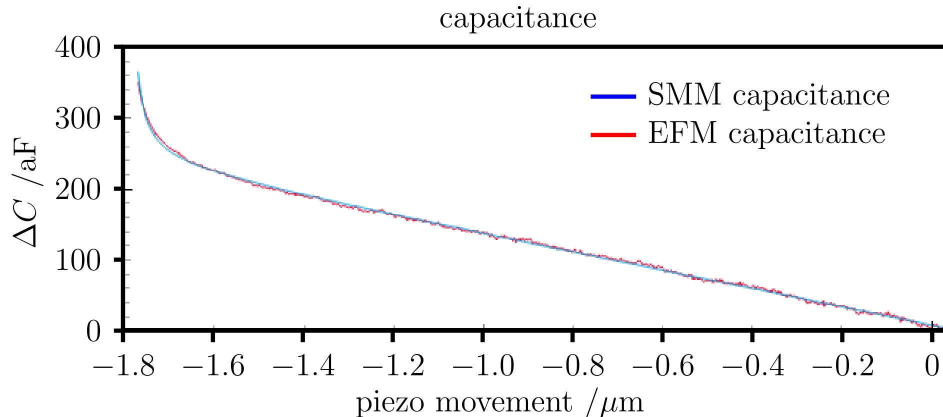

Figure 18: The simultaneously obtained EFM (blue) and SMM (red) capacities. The error parameters e00, e01, e10 and e11 were used as free fitting parameters to match the SMM capacitance to the EFM capacitance.

This calibration has first been introduced by Hoffmann et al. [47]. They used known capacities on a well-known calibration sample to solve eq. (4). As this calibration takes into account reflections and scatterings of the sample itself, it is valid only when performed directly on the DUT.
Therefore, Gramse et al. introduced a method enabling the calibration directly on the DUT [34]. A force distance curve is recorded directly on the DUT. During this force distance measurement SMM and EFM data are acquired simultaneously. From entire EFM dataset, the second harmonic is recorded as it gives the best opportunity to calculate the local capacitance. By integrating eq. (27) over the distance to the sample, a capacitance distance curve can be generated. The error parameters for the calibration can be calculated by fitting them into eq. (3) with $\underline{S}_{11m}$ being the $\underline{S}_{11}(z)$ data recorded during the approach curve and $\underline{r}_{DUT} = \frac{1}{j\omega C_{EFM}(z)}$ being the EFM capacitance data from the approach. Figure 18 shows the fitted capacitance obtained with an approach curve at the calibration sample. This fit enables the possibility to measure resistance and capacitance data from the acquired $\underline{S}_{11m}$. [34]. Figure 19 shows the $\underline{S}_{11m}$ in amplitude and phase recorded with an unbiased tip and the calculated capacitance signal from a measurement at the p-n-calibration sample. The monotonous dependency of the capacitance on the dopant density is promising. There is no intrinsic possibility for p/n distinction and no way to

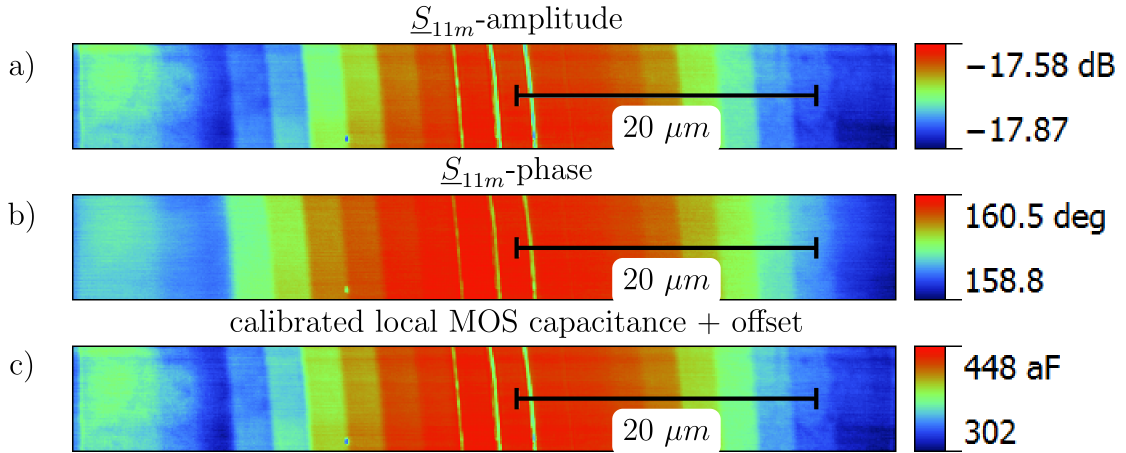

Figure 19: SMM measurement of calibration sample. a) The amplitude of the reflected microwave signal. b) The phase of the reflected microwave signal. c) The calibrated capacitance including the offset capacitance due to calibration.

accurately calculate the densities due to the unknown surface potential state. Therefore, section 5 will focus on ways to overcome those shortcomings.

3.3.2 SMM Setup

The principle of SMM has already been explained in section 3.3.1. The basic setup combines the high resolution imaging opportunities of an AFM with the opportunity to measure HF networks using a VNA. The setup consists of the AFM scanner and stage itself, a stage controller, an AFM controller, an acoustic enclosure, active vibration isolation, a head electronics box, the lock-in amplifiers and the network analyzer. Figure 20 shows the different components in detail. Figure 20 (a) shows the AFM stage and the scanner. The stage is a 200 mm x 200 mm stage, controlled by the stage controller shown in fig. 20 (e) with an accuracy and repeatability of 0.5 μm. The scanner, controlled by the AFM controller shown in fig. 20 (c) and the head electronics box (HEB) in fig. 20 (d) offers a range of 90 μm in x- and y-direction with an accuracy of 0.5 nm. In z-direction the range is 7 μm with an accuracy of 0.03 nm. The acoustic enclosure shown in fig. 20 (b) reduces the vibrations of the setup. Furthermore, it provides a shield layer and an isolation to reduce

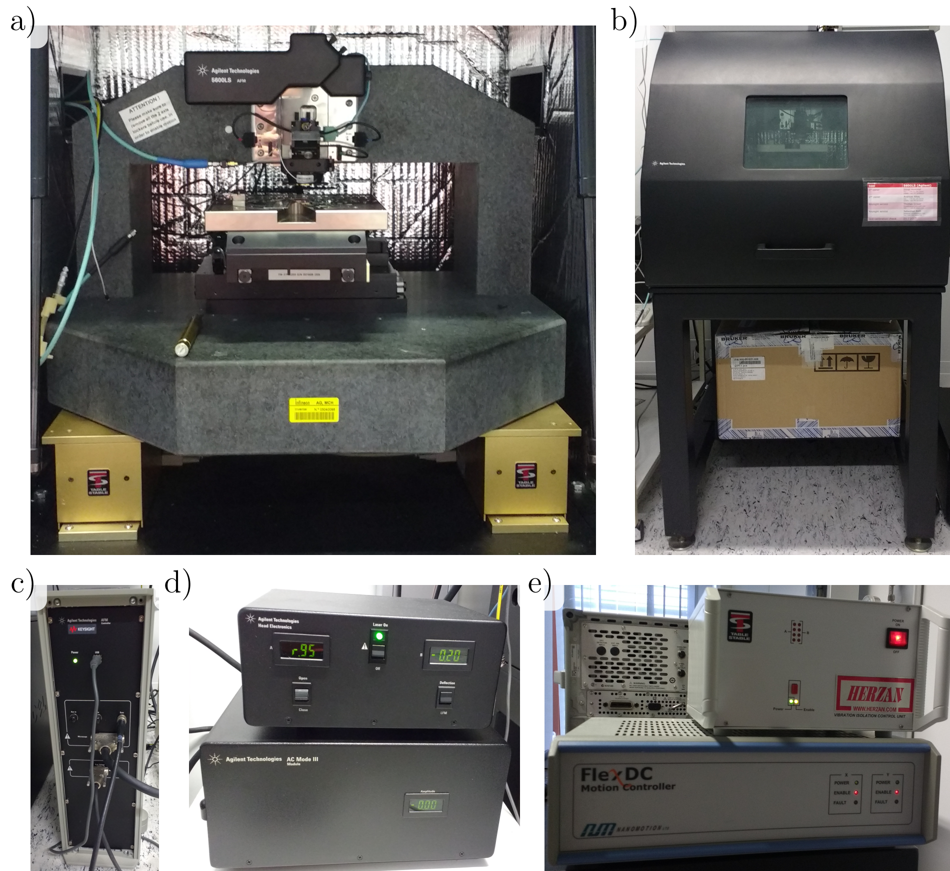

Figure 20: Components of the Keysight 5600 LS. a) The AFM itself consists of the marble table, the stage adjustable through servo motors and the AFM scanner including the optics. The feet below the table can be controlled for active vibration isolation. b) The acoustic chamber provides a passive vibration isolation as well as an isolation against electromagnetic fields. c) The AFM controller acts as an interface between the AFM software and the HEB. d) The HEB in the upper part controlls the AFM head servo and scanner. The MAC mode III module in the lower part provides the lock-in amplifiers enabling multiple lock-in based AFM modes. e) The table stable box in the upper part controls the active vibration isolation. The flex DC motion controller in the lower part controls the stage servo movements.

distortions due to external fields. The vibration isolation is enhanced by an active vibration isolation called table stable controlled by the unit shown in fig. 20 (e). The marble AFM table is set onto the actively controlled feet shown in fig. 20 (a). This enables an active cancellation of external vibrations.

The three lock-in amplifiers in the magnetic AC (MAC) mode III module shown in fig. 20 (d) can be simultaneously used to generate and lock-in an AC modulation voltage, which can be applied either to the AFM tip or through the stage to the sample. Therefore, they provide a frequency range between 200 Hz and 600 MHz and a maximum lock-in signal amplification of 128.

3.3.3 Vector Network Analyzer

The network analyzer used in this setup is the Keysight N5230C as shown in fig. 21. The VNA provides a frequency range between 300 kHz and 20 GHz. It offers four ports, thus enabling reflection and transmission measurements. As SMM is usually based on reflection measurements, only port one is used during the measurement. A dopant profiling measurement module (DPMM) is attached to port one as shown in fig. 21. It has two basic functions in SMM. The first one is to amplify the reflected microwave by 10 dB and increase the

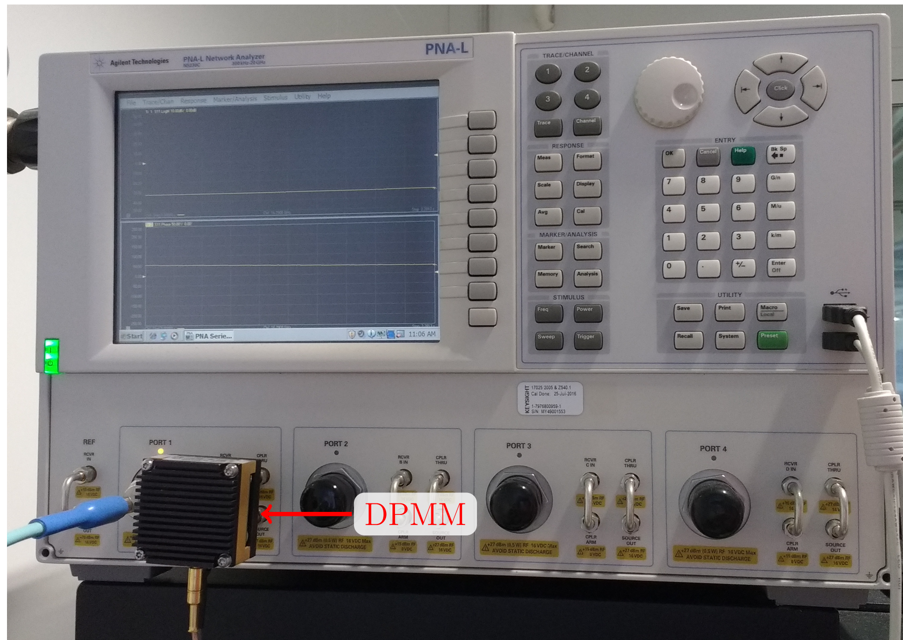

Figure 21: The vector network analyzer Keysight N5230C offers four ports and a frequency range from 300 kHz to 20 GHz. The DPMM is used to amplify and demodulate the reflected signal.

signal to noise ratio (SNR). The second is to feed the signal back into the lock-in amplifier to enable the $d\underline{S}_{11}/dV$ measurement.

3.4 Alternative Methods

In addition to SMM, there are several other dopant profiling methods to be considered. The two most established methods to quantitatively measure dopant densities are spreading resistance profiling (SRP) and secondary ion mass spectroscopy (SIMS). Both methods are clearly superior in accuracy and ease of use when an absolute dopant density is needed. In contrast to the good accuracy and depth resolution, they do not offer a possibility to resolve lateral deviations. Time of flight SIMS (ToF-SIMS) adds such a possibility to SIMS. In ToF-SIMS, the measured atoms can be assigned to their position, but as the probed area decreases, no low dopant densities can be determined. Therefore SRP and SIMS are complimentary methods to the locally resolved dopant profiling methods discussed in this thesis. Another established method is the wet chemical decoration. There are various acids, e.g. hydrofluoric acid, with etching rates selective on n- and p-type doping. After etching the region of interest, e.g. the p/n junction can be imaged optically or with a scanning electron microscope (SEM). In contrast to SRP and SIMS, it provides a good lateral resolution but no possibility for quantitative analysis. Therefore, it is a complementary method to SMM, enabling to image p/n junctions over large areas. Alternatives to SMM providing an ability to locally resolve doped regions with a quantitative approach are SCM, SMIM, scattering-type scanning nearfield optical microscopy (SSNOM), scanning spreading resistance microscopy (SSRM) and SEM. As the only non-SPM method, SEM, will be discussed first. The scanning probe based methods SCM, SMIM, SSNOM and SSRM will be discussed afterwards.

3.4.1 Scanning Electron Microscopy

SEM is one of the most popular methods in material characterization [48]. Various different localization applications in failure analysis can be solved using

SEM. Dopant profiling is rather an uncommon SEM application. Nonetheless, there are various studies of applying SEM for dopant profiling [48–51]. In SEM the DUT is investigated by scanning the electron beam across the surface of the DUT [50]. SEM offers various possibilities of electron detection. For dopant contrast, the best choice is a secondary electron (SE) detector [48–51]. The dopant contrast for p-type silicon was found to be present in a range between 10^{16} atoms cm^{-3} and 10^{20} atoms cm^{-3}, while the contrast range for n-type Si was found to be lower [48]. Figure 22 shows pictures acquired with two different SEM at the calibration sample. Figure 22 (a) was acquired using a Hitachi SU 8010 SEM. A low acceleration voltage of 0.7 kV was chosen as well as a large distance to the sample of 9.6 mm to achieve a good dopant contrast resolution. The contrast in the p-type region is distinguishable down to 5×10^{16} atoms cm^{-3}. The last clearly distinguishable contrast at n-type regions can be observed at 10^{18} atoms cm^{-3}. This confirms the expectations from literature. It was suggested that dopant contrast resolution could be increased by energy filtering [50]. Therefore the calibration sample was investigated with a FEI Magellan in deceleration mode. The benefit of this energy filtering is to get a more pronounced dopant contrast resolution. The low-pass energy filtering increases the influence of the lower energetic SEs in a depth of 5 nm, deemed responsible for the dopant contrast. Filtering those low energetic SEs supposedly increases the image contrast resolution [50]. Figure 22 (b) shows that the contrast in p-type could be increased down to 10^{16} atoms cm^{-3}. The contrast resolution of the n-type region still stops at 10^{18} atoms cm^{-3}. SEM is definitely a good method to quickly estimate the dopant profile of a sample. In addition to its quickness, it shows a monotonic behavior within one dopant type, making it easy to interpret as long only dopants of the same type are compared. A definite drawback is the inability to quantify the dopant densities, as the contrast is dependent on several operation parameters and sample charging strongly influences the signal. Furthermore, the inability to distinguish p-type from n-type is a big disadvantage. Still, its ability to quickly image large and small scan areas makes it an important supplementary tool for dopant profiling.

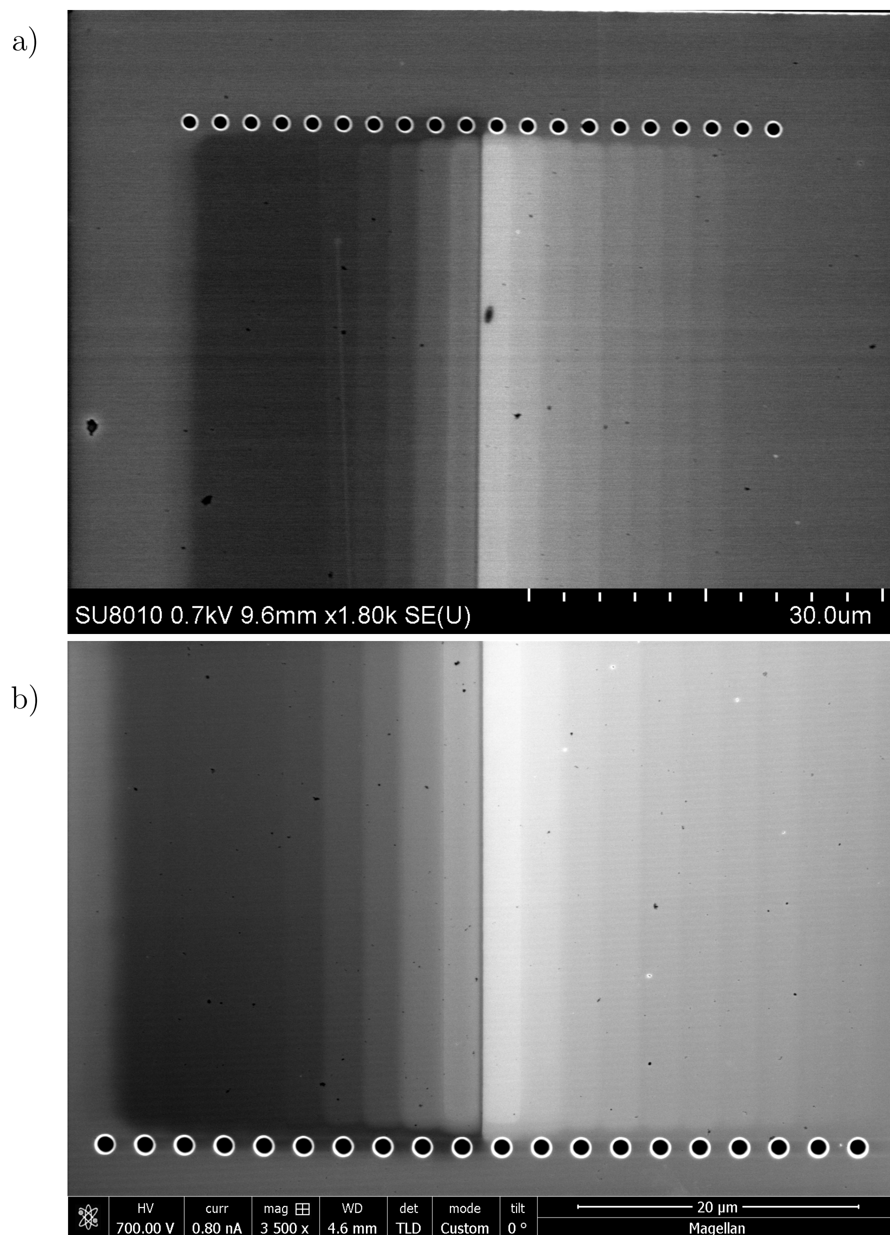

Figure 22: SEM image of calibration sample. The data shown in a) was acquired with a Hitachi SU 8010 at 0.7 kV with sample distance of 9.6 mm. The data shown in b) was acquired with a FEI Magellan at 0.7 kV with sample distance of 4.6 mm in deceleration mode.

3.4.2 Scanning Capacitance Microscopy

SCM is a well-established technique for qualitative dopant profiling of semiconductor devices. Figure 23 shows the general setup of an SCM. Like many meth-

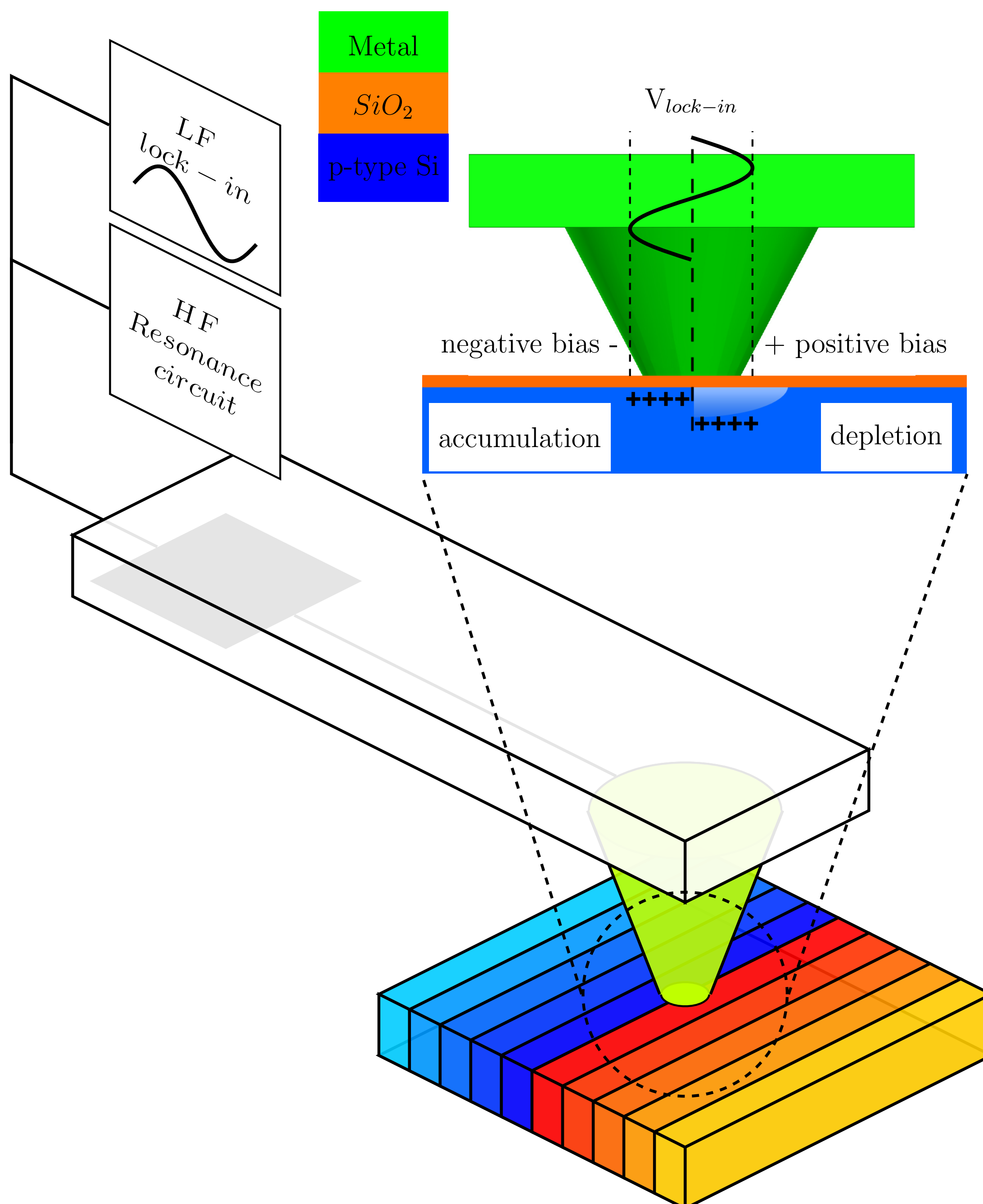

Figure 23: AFM SCM schematics. In addion to contact mode setup, a resonance circuit and lock-in amplifiers are connected to the AFM tip to probe the MOS structure and apply the modulation voltages. The inset shows, how the AC modulation bias is applied to probe the slope between accumulation and depletion (see fig. 11).

ods probing electrical sample properties, it is based on contact mode AFM. Like SMM, it operates with a high frequency to probe the MOS capacitor consisting of the conductive tip, the native oxide and the investigated semiconductor. Unlike SMM, the HF signal is not generated by a network analyzer. In SCM a resonance circuit typically oscillating at a GHz frequency is detuned by the MOS capacitor. As the oscillation frequency is mainly driven by the resonance circuit, the frequency is relatively fixed. A connected lock-in amplifier is used to modulate this HF oscillation by applying a kHz range frequency, similar to SMM. The resulting dC/dV signal has been used for multiple approaches to find a quantitative dopant profiling technique [52–57]. Those ideas, like in SMM, were mostly based on comparisons with other samples or methods [52, 53]. Since none of them succeeded in industrial use, a lot of work was put into modeling and understanding the SCM signals [52,54,55,58]. Many of those advances neglected the problem of different contact potentials and other parasitic elements between the semiconductor surface and the backside contact. Furthermore, the non-monotonic behavior of the detected dC/dV signal was not taken into account properly leading to artifacts. Figure 24 shows an SCM image acquired at the calibration sample. It was acquired at a relatively small oscillation frequency to reduce the frequency dependent non-monotony. A high modulation voltage of 5 V peak to peak was used to reduce dependence on the DC setpoint and probe the C-V characteristics in a wider range from accumulation to depletion. As shown in fig. 24, this enables a monotonous relation between dopant densities and signal over a wide range of densities. However, as the monotony range is unpredictable and the setpoint dependency is still influencing the measurement no quantitative result is possible. A multi-measurement calibration like described in section 3.3 could be transferred to SCM [41].

3.4.3 Scanning Microwave Impedance Microscopy

SMIM is based on contact mode AFM as well. The setup is quite similar to SMM and SCM and basis for many approaches to image dopant densities [59–63]. Like SCM, it operates at a limited frequency range with a frequency of about 3 GHz applied to a conductive probe [59]. As SMIM is the most recent

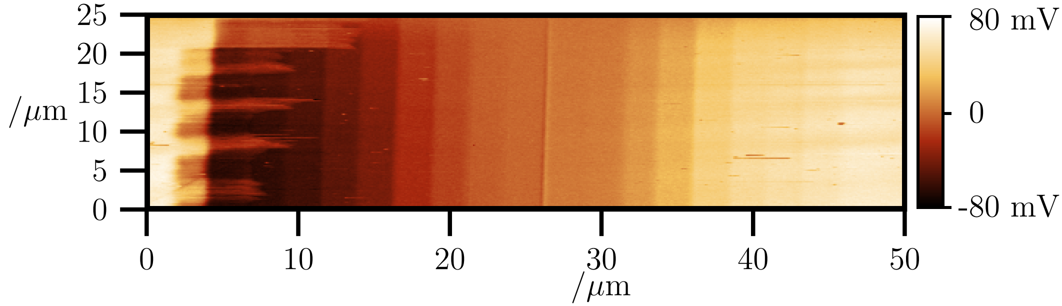

Figure 24: SCM out-of-phase (Q-) channel image of calibration sample. The image was recorded with 600 MHz resonance circuit oscillation frequency, 17 kHz modulation frequency with 5 V peak to peak. The lock-in phase shift was adjusted to level out the in-phase (I-) channel. There was no need to adjust the lock-in offset.

of the three AFM based methods it comes with a few new improvements in setup. Similar to SMM the measurement setup is matched to 50 Ω. In SMIM, custom made cantilevers closely matched to 50 Ω are used to reduce reflections and stray effects [59]. This leads to a better SNR. The lock-in amplifier is used similar to SCM and SMM to modulate the microwave signal and acquire a dC/dV signal. Figure 25 shows an image acquired on the calibration sample. The higher frequency of 3 GHz, and the lower AC bias of 1 V, causes the non-monotonic behavior to occur already at higher densities in SMIM than in SCM. In general, the drawbacks are similar to SCM and SMM when using the dC/dV signal. Like SMM, SMIM provides an opportunity to separate the reflected microwave into a capacitive and a resistive part [59]. In SMIM this is done by separating the reflected microwave into an in-phase and an out-of-phase part using a lock-in amplifier. A purely capacitive sample with a known capacitive step and no resistive change is measured. The phase shift is adjusted to flatten out the resistive part in one of the two signals and adjust the slope into the right direction in the other signal. After this calibration, the in-phase and out-of-phase channels from the lock-in can be used for capacitive and resistive imaging. Figure 26 has been acquired using a calibrated SMIM setup. The image shows the potential for monotonic dependency of the SMIM-C signal on the dopant densities. For the shared disadvantages with SMM, like lacking abilities to distinguish p- and n-type and the uncertain state of the MOS-

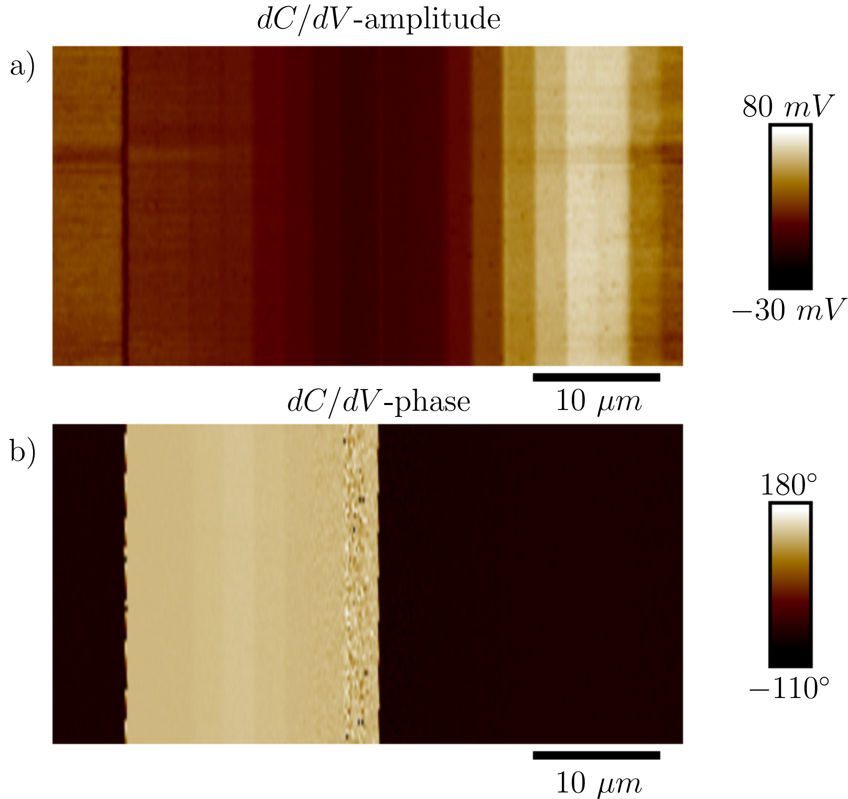

Figure 25: SMIM dC/dV measurement of calibration sample. a) shows the dC/dV-amplitude of the lock-in signal. b) shows the corresponding dC/dV-phase data. In contrast to the shown SCM and SMM lock-in images, The information is split into amplitude corresponding to the absolute value of the slope and the phase, indicating the dopant type through the sign of the slope.

structure, possible solutions will be discussed in section 5. The advantages of SMIM are the shielded probes enabling a better resolution due to the better SNR with smaller tips and the possibility to combine it with different AFMs from different tool vendors. The combination with force volume spectroscopy in a Bruker tool for example offers completely new possibilities by quickly acquiring a whole image of spectroscopy curves in each point. This enables the acquisition of C-V curves and the determination of a capacitance offset due to stray effects. Although those features might pay off in future, SMIM-C values are only arbitrary units. Therefore the possibility to measure absolute capacities in SMM is an advantage compared to SMIM.

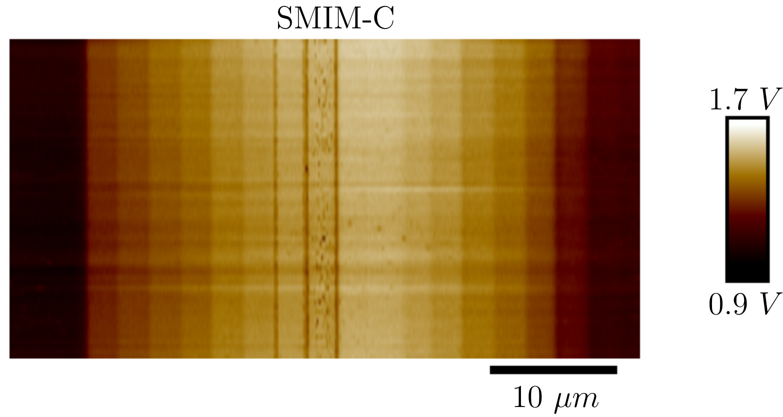

Figure 26: Capacitive SMIM data acquired on the calibration sample. The data scale correponds to the out-of-phase channel of a lock-in amplifier operating at the microwave carrier frequency. The lock-in phase is adjusted to make the out-of-phase channel sensitive on capacitive changes.

3.4.4 Scanning Spreading Resistance Microscopy

Like SMM, SCM and SMIM, SSRM can be used to generate locally resolved 2D dopant profiles [64–67]. SSRM is based on contact mode AFM as well. Figure 27 shows schematically the setup of SSRM. The principle of SSRM is to measure the local resistance

$$R(x,y) = \frac{\rho(x,y)}{4r}, \tag{28}$$

where ρ is the local resistivity of the sample and r is the tip radius [68]. Most other contact mode AFM based methods use contact forces in the pN and nN range. In contrast, SSRM needs forces in the range of μN or even mN to establish a proper contact between tip and sample [69]. Reasons for this high force are the need to scrape away the native oxide and to transform the silicon phase beneath the tip to achieve an ohmic contact [70, 71]. A constant DC bias voltage is applied to the tip during the measurement. The conductive tip is connected to a logarithmic current amplifier to measure currents (see fig. 27). It consists mostly of doped diamond to reduce the wear due to the high forces.

Figure 28 shows an SSRM image acquired on the calibration sample. The image was obtained with a contact force of 8.6 μN. The image shows the current

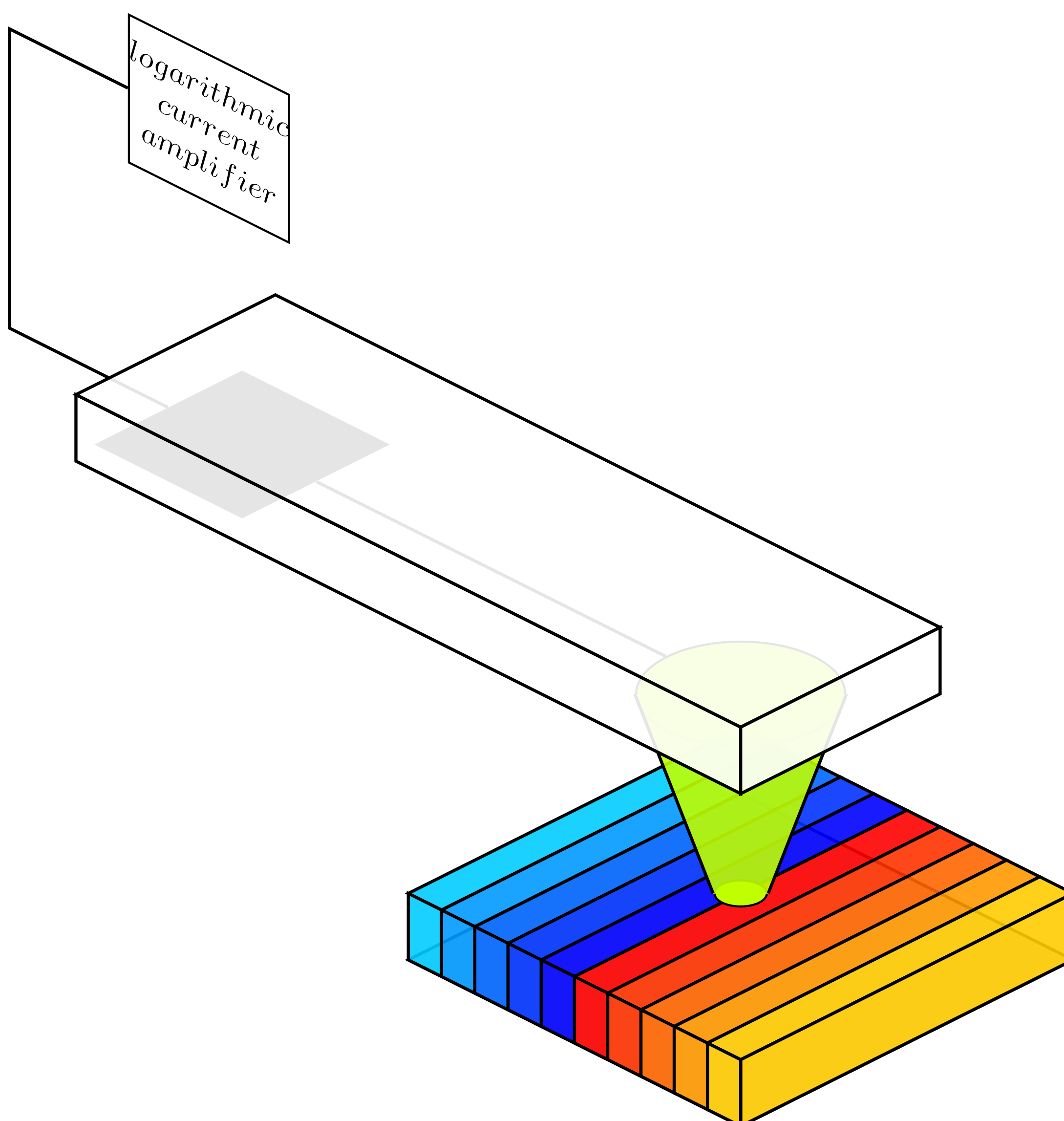

Figure 27: AFM SSRM schematics. Additional to the contact mode AFM setup, a logarithmic current amplifier is connected to the AFM tip. With an applied DC bias, it enables the measurement of small currents through tip and sample enabling the calculation of the local resistance.

flow at a bias of 2.5 V. For an entirely ohmic contact, p- and n-type doped regions are expected to give the same contrast. The distinction in fig. 28 could be due to the Schottky-like contact between tip and sample. Consequently, in case of a Schottky-like contact the p/n contrast reverts with a sign change of

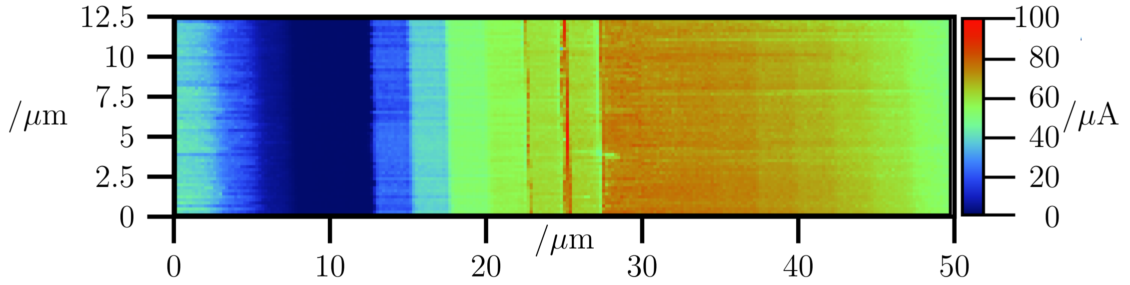

Figure 28: The SSRM image obtained at the calibration sample shows the currrent measured with a DC bias of 2.5 V.

DC bias. In the case of the fig. 28, the sample has a p-type substrate. Hence, the reduced current in the n-type sample region might as well be due to the p/n junction. The dependency between resistance and dopant density in SSRM is monotonic, leading to an easy interpretation of the native results. A drawback is the small signal difference between the dopant densities in the higher range, making it hard to separate small deviations from measurement artifacts and drift. The distinction between p- and n-type cannot be done from one image. If the contact is not entirely ohmic, the p/n information can be gained by comparing images acquired with different DC bias. As most state-of-the-art AFMs provide a mode to scan a line twice with different parameters, those images can be acquired in one measurement. A big benefit of SSRM is the ability to measure on focused ion beam cross-sections [69]. One of the biggest drawbacks is the destructiveness of the SSRM measurement, as the diamond tip scrapes away the measured region due to the high forces. Furthermore, the calibration for absolute density is quite time consuming as it has to be performed by comparing the DUT to a calibration sample [69]. Due to the wear of the tips, the validity of such a calibration is quite uncertain.

3.4.5 Scattering-type Scanning Nearfield Optical Microscopy

SSNOM is a tapping or non-contact mode based scanning probe method. As shown in fig. 29, a laser is focused on the cantilever tip and the backscattered light is detected [72–77]. The tip is thereby used to re-radiate the incident light and to supply a concentrated longitudinally polarized optical field to

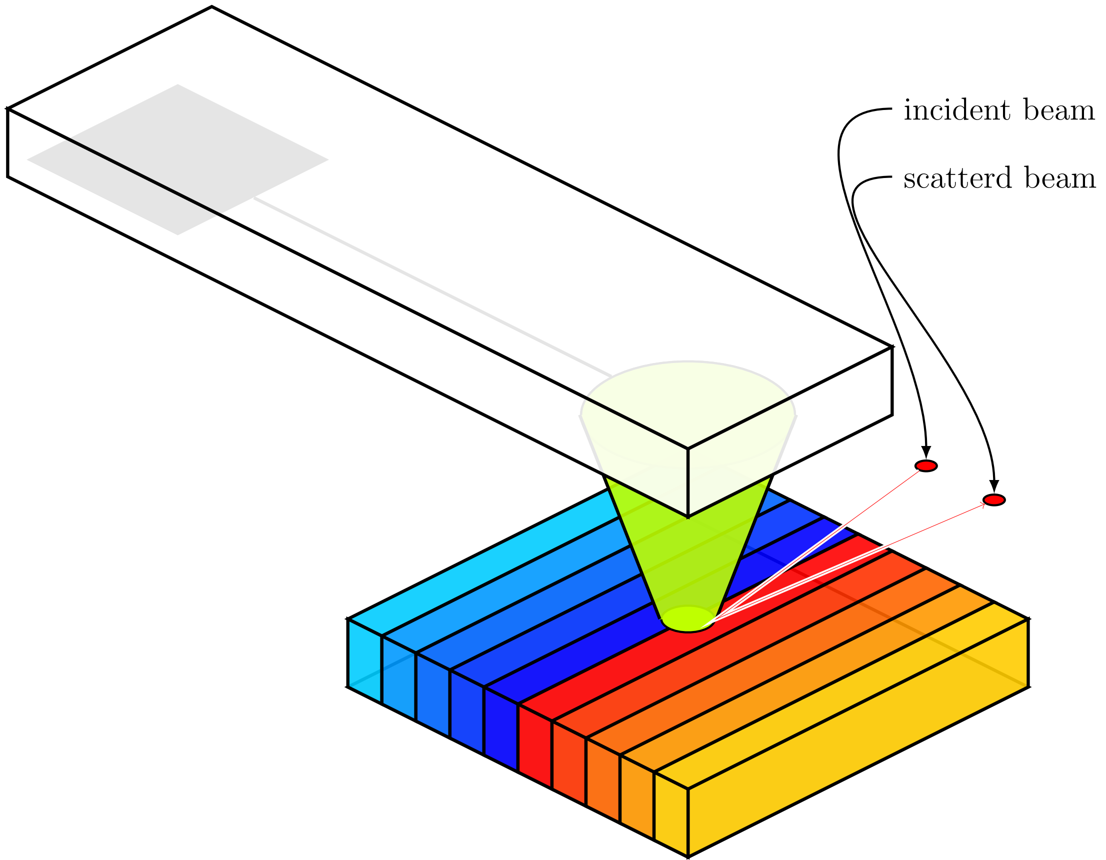

Figure 29: AFM SSNOM schematics. In addition to the tapping mode AFM setup, the tip is illuminated with a laser beam. The backscattered part of this beam is detected and resolved in amplitude and phase.

the sample material [74]. The tip induced electromagnetic field $E_{scattering}$ can be used for material dependent contrast [74]. The corresponding nearfield amplitude and phase can be extracted simultaneously to the AFM topography signals by demodulation at higher harmonics of the tapping frequency [73, 74]. In doped regions where the plasma frequency of a doped semiconductor equals the illumination frequency of the laser, nearfield amplitude and phase give a pronounced signal contrast [78].

Figure 30 shows SSNOM images acquired at the calibration sample using wave numbers between 700 cm^{-1} and 1900 cm^{-1}. The nearfield phase in fig. 30 (a) shows a good signal contrast. The peak in nearfield phase signal correlates with the dopant density. Consequently, lower wave numbers result in a signal

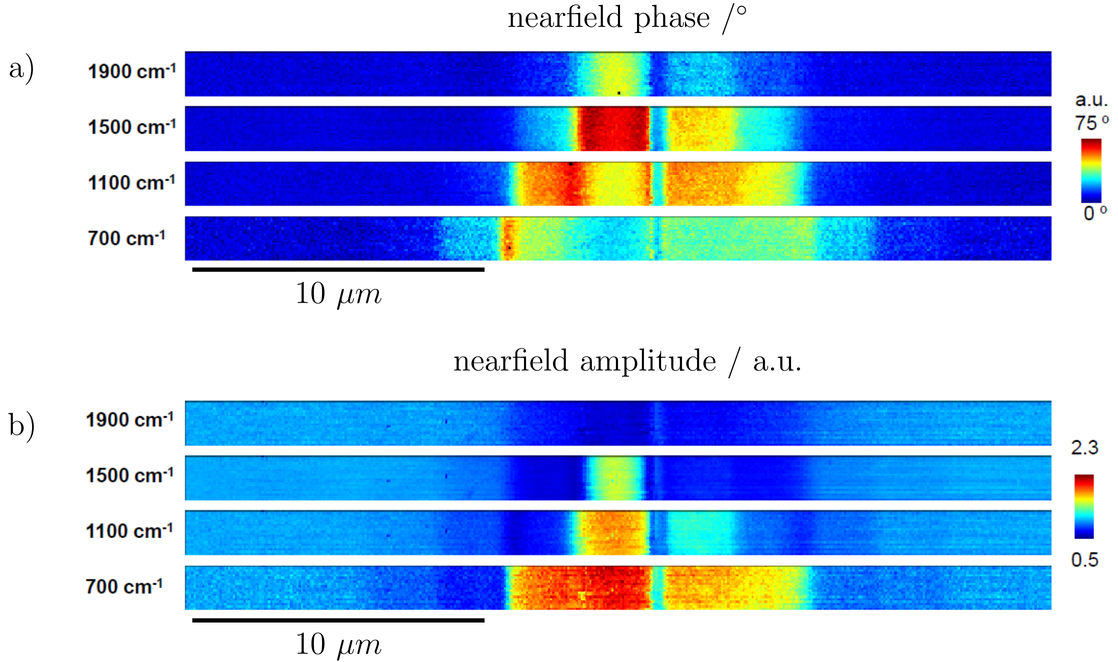

Figure 30: SSNOM image of the calibration sample. The SSNOM phase is shown in a), the SSNOM amplitude in b). Both were acquired simultaneously at wave numbers of 700, 1100, 1500 and 1900 cm^{-1}, shifting the signal peak to lower densities with lower wave numbers.

peak at a lower dopant density. The distinction of differently doped regions is clearly possible down to 10^{19} atoms cm^{-3} at a wave number 700 cm^{-1}. In this case, the nearfield amplitude has a wider range of distinguishable dopant densities. As shown in fig. 30 (b), the amplitude enables to resolve densities down to 4x10^{18} toms cm^{-3} at a wave number 700 cm^{-1}. The density resolution range can be enhanced by applying a higher laser frequency to achieve a lower wave number. Therefore the calibration sample was investigated with THz laser, using a frequency of 2.5 THz [78]. The corresponding SSNOM images acquired with a wave number of 85 cm^{-1} are shown in fig. 31 (a). The SNR is reduced, but the largely enhanced dopant density range down to 4x10^{17} atoms cm^{-3} shows the future potential of SSNOM. The extracted profiles in fig. 31 (b) clearly depict this density range. In SSNOM dopant density can be estimated from the wave number of its peak in SSNOM phase. Investigation of peak

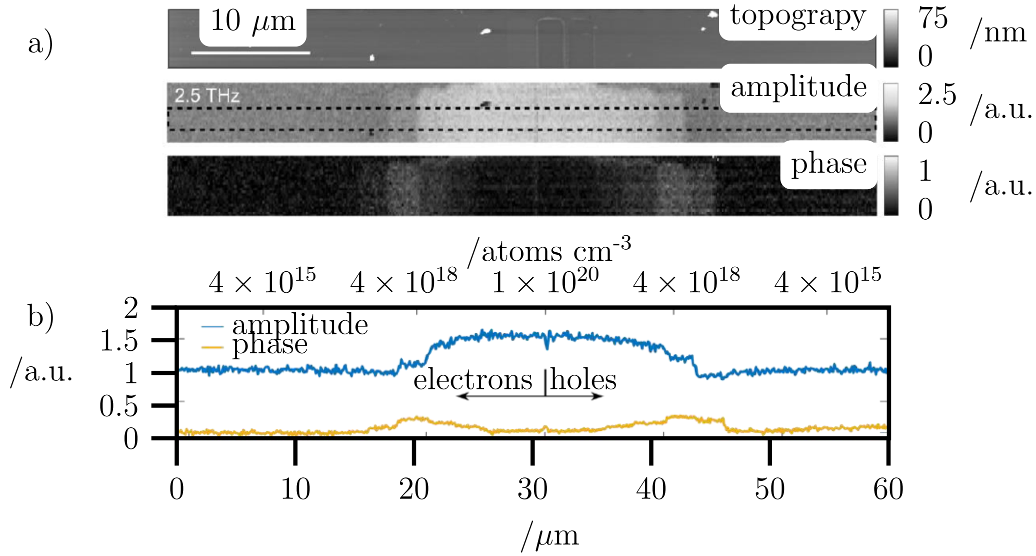

Figure 31: 2.54 THz SSNOM image of the calibration sample. The topography, SSNOM amplitude and phase is shown in (a). The corresponding wave number is 85 cm^{-1}. The extracted profiles are shown in (b). The results are published in [78]

positions is possible by continuous broadband infrared nearfield spectroscopy (nano-FTIR). Nano-FTIR was performed on the calibration sample. Figure 32 (a) shows the topography and nearfield phase image of the calibration sample. The spots where the nano-FTIR curves were acquired are marked in the colors corresponding to the curves in fig. 32 (b). The curves have all been acquired on the n-type silicon part of the sample. As shown, the peak of the nano-FTIR curves shifts to lower wave numbers with decreasing dopant density. The last observable peak is the one acquired at $4x10^{19}$ atoms cm^{-3}. For lower dopant densities, a sweep to lower wave numbers would have been necessary. The big advantage of nano-FTIR is, that the peak position is sample independent and simply depends on the dopant density. SSNOM in combination with nano-FTIR is overall a really promising method. Today its reduced dopant density range due to frequency limitations reduces the applications. If these technical limitations can be overcome, SSNOM will be a very promising method for dopant profiling.

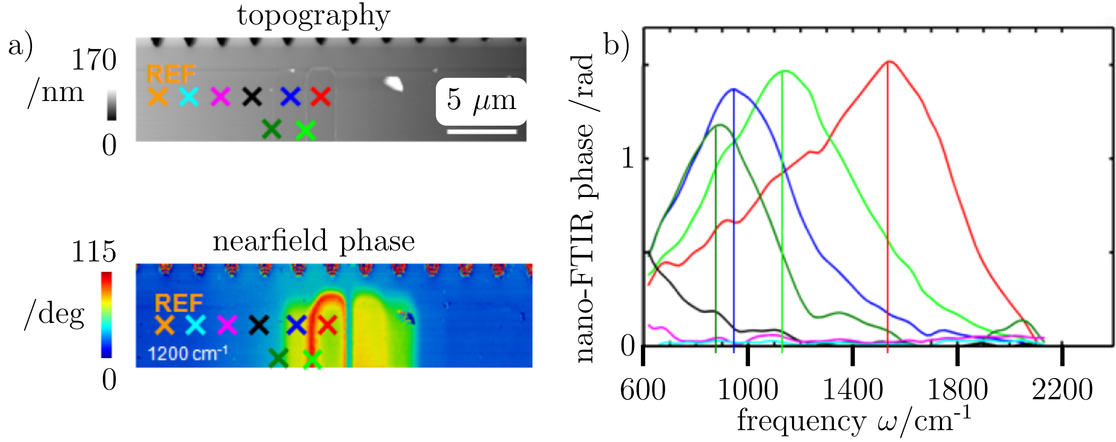

Figure 32: The nano-FTIR has been acquired at the calibration sample. a) shows the topography and nearfiled phase images. b) shows the corresponding nano-FTIR curves, the sweep locations are marked in a).

3.5 Summary

To sum up the dopant profiling methods, they are compared regarding resolution, distinction of dopant type and dopant density quantification. The benefits and disadvantages of the different methods are shown in table 2.

Chemical decoration has a good resolution, as the results of the etching can be visualized with an optical microscope or a SEM. The dopant type distinction works, if there is an abrupt p/n junction. A diffused junction is difficult to resolve. It is not possible to determine a dopant type in a monotonously doped

Table 2: Dopant profiling capabilities of the discussed methods.

Method	Resolution	Dopant type	Dopant density
SMM	+	+	+
SEM	+	-	+
SCM	+	+	0
SMIM	+	+	+
SSRM	++	0	+
SSNOM	+	0	0
SIMS	-	++	++
SRP	-	0	++
Chemical decoration	+	+	0

material. There is no possibility to determine the relation between dopant densities with a classical wet chemical approach.
SRP is a technique to very accurately probe the dopant density of a larger region within a semiconductor. It provides a very limited possibility to distinguish the dopant type and is limited to large sample areas.
SIMS provides a similarly accurate capability to quantitatively measure dopant densities. The advantage of SIMS is, that not only dopant type but even the dopant atoms can be determined. Like SRP, it is limited to large areas. It requires a high atom count rate, which decreases with the investigated area, to accurately measure dopant densities.
SEM provides an imaging capability for dopant densities with a high lateral resolution. There is only very limited possibility to distinguish p- and n-type dopants. The dopant contrast scales with dopant density within the same dopant type. It offers a good possibility to get a first impression of the investigated sample.
SSNOM is an SPM based method. Consequently, it provides a high spatial resolution. The inability to distinguish dopant type and the impossibility to distinguish dopant densities below $4x10^{17}$ atoms cm^{-3}, even with a THz laser, limit the applications of this method.
SSRM offers the best resolution of the discussed methods, down to a couple of nm. The SSRM signal scales with dopant densities, providing a possibility to relate densities. There are limited possibilities to determine the dopant type, practicable only if the sample is measured with a Schottky-like contact.
SCM, as another SPM method, offers a high spatial resolution. The signal scales down with dopant density and reverts at some point. This point depends on various factors. It cannot be predicted exactly. The use for dopant relations is sensitive to errors. The SCM signal phase can be used for dopant type distinction, but the risk of errors due to an unnoticed phase shift must be considered.
SMIM is quite similar to SCM, thus provides similar capabilities. SMIM benefits of the possibility to extract a capacitive and resistive part. Therefore, the p/n distinction can be done reliably and the capacitive signal scales with dopant density.
SMM provides, like most other SPM methods, a good lateral resolution down

to 20 nm, depending on the used probe. Furthermore, it offers various possibilities to determine the dopant type. Similar to SMIM, the extraction of capacitive and resistive part allows a reliable p/n distinction. The capacitance signal scales with dopant density. The capability to calculate absolute capacities provides an advantage over SMIM, which can be used for quantitative investigations. Therefore, section 5 will deal with the possibilities SMM provides to determine dopant types and densities.

4 Experimental Details

4.1 Sample Preparation for SMM

The sample preparation as well as the right choice of imaging method is equally important for dopant profiling. For SMM, there are two possibilities of sample preparation. An image can either be acquired by scanning the sample surface to image the implanted regions, or by performing a cross-section to enable to image the dopant profile in depth.
For the surface scan of the sample, the silicon needs to be bare. To access the bare sample surface, possible metal and passivization layers need to be removed, which can be achieved by a wet-chemical lift-off. Hereby, the sample is dipped into a HF solution to remove the oxide layers on top of the silicon. The metal and further insulating layers get under-etched and the pure silicon is accessible. This method works well for samples with a rather flat topography. When a sample with deep trenches in the area of interest is investigated, the topography after lift-off makes it impossible to investigate the sample in contact mode AFM. The oxide within the trenches is etched and leaves cavities. These cavities present a topography too challenging for standard full metal SMM probes. Alternatively, the sample surface can be polished down to the silicon to reduce the topography. As it is hard to stop at the exact right depth, this method is only used in case of lift-off causing too much topography. In both cases, the mandatory backside contact can easily be achieved by attaching the substrate to the AFM stage using a conductive adhesive, such as silver glue.
Most SMM studies are nowadays performed at a cross-section. The cross-section can be either prepared free standing or embedded. The free standing cross-section offers multiple possibilities to achieve a good sample contact and is therefore the most common cross-section used in AFM based dopant profiling methods. As the cross-section is performed free standing, the sample front with its metal as well as the sample substrate are still accessible. Thus, when a contact through the metal or the substrate is needed, it can be made with silver glue. To prepare the free standing cross-section, the sample substrate is attached to a carrier and grinded to the region of interest. The grain size of the

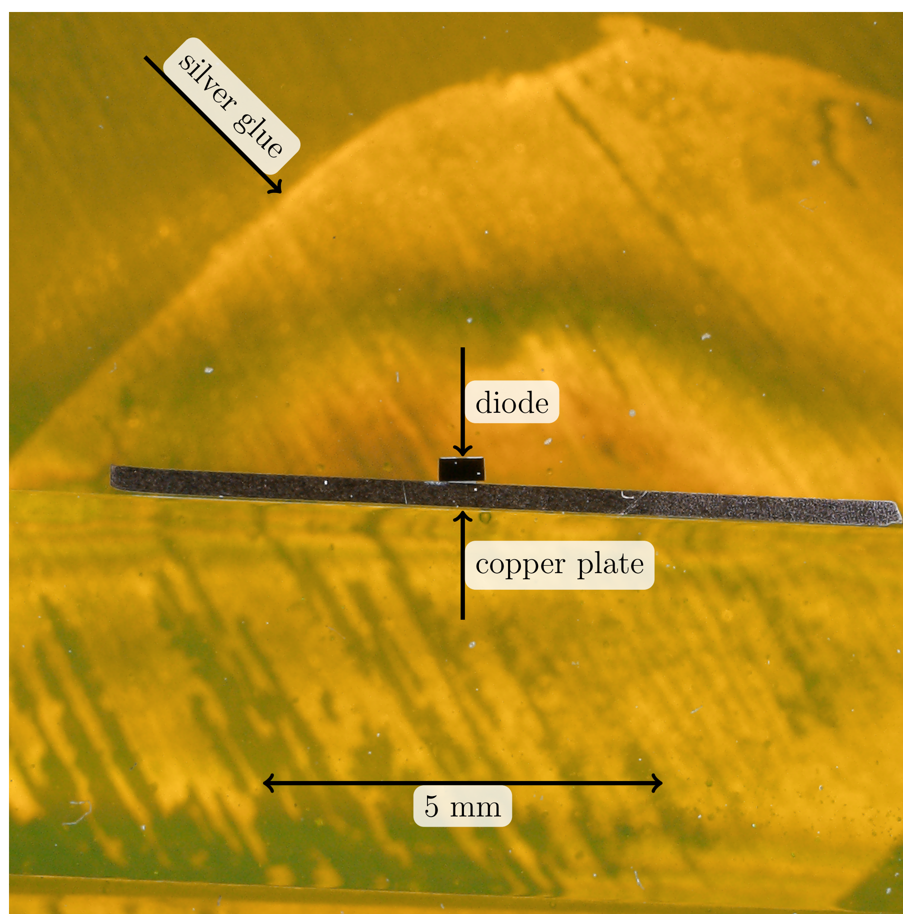

Figure 33: Cross-section of a diode prepared for SMM. The diode is attached to a copper plate with silver glue. The structure is embedded into epoxy (yellow). The silver glue attaching the copper plate to the AFM stage can be seen through the epoxy.

grinding foils is decreased when approaching the region of interest. The final step is a polishing step, reducing the roughness to below 4 nm, thus enabling an SMM scan without topography artifacts. The free standing cross-section can cause break-outs at the edges as well and is susceptible to edge rounding through the polishing steps. As the important dopant layers are mostly close to the sample surface, this edge rounding can cause trouble scanning close to the edges. This problem is eliminated for an embedded cross-section.Here, the sample is clamped into a fixture and embedded into epoxy resin. The epoxy is cured out before the sample is ground. After the embedding, the grinding is

performed similar to the free standing cross-section by reducing the grain size of the grinding foils while approaching the region of interest and finalizing the cross-section with a polishing step. Embedded, a surface roughness below 2 nm is achieved. Embedded cross-sections offer a higher reproducibility and are less susceptible to edge rounding. An embedded cross-section performed for SMM is shown in fig. 33. To make the substrate contact accessible, a conductive metal plate is attached to the respective sample substrate using a conductive silver glue before the embedding procedure is performed. Through this conductive plate, the sample can be connected to the stage potential during the measurement. This kind of sample preparation combines the benefits of free standing and embedded cross-sections.

4.2 Conductive Probes

The physical understanding of conductive probe, consisting of tip, cantilever and chip, plays an essential role in SMM and related methods. On the one hand the mechanical properties of the probe are optimized to prevent unintended oscillations and wear. On the other hand, for all electrical SPM methods a good conductivity of the probe is essential in order to establish a signal path to the sample. While for DC and low frequency methods like SSRM and EFM it is sufficient to provide a conductive path to the tip, SMM and other HF methods need a microwave to be transmitted through the cantilever and tip to the sample.

Therefore, a highly conductive sharp probe is required to obtain high resolution SMM results. The vendor Rocky Mountain Nanotechnology (RMN) specialized on GHz probes provides different kinds of probes, offering full metal cantilevers on a ceramic substrate. Most of the investigations in section 5 are performed using a RMN 25Pt300A probe. According to the data sheet, this probe has a tip shank length of 80 μm ($\pm$ 25 %), a cantilever length of 300 μm ($\pm$ 15 %) and a cantilever width of 110 μm ($\pm$ 15 %). The nominal spring constant is 18 N/m ($\pm$ 40 %) and the resonance frequency is 20 kHz ($\pm$ 30 %). The guaranteed initial tip radius is $<$ 20 nm. The cantilever and tip consist of solid platinum (Pt). Further, a second version of this probe, RMN 25PtIr300A, is used. Besides a small deviation in resonance frequency and spring constant

(21 kHz (± 30 %) and 22 N/m (± 40 %)), the data sheet is similar to the RMN 25Pt300A probe. The platinum-iridium (PtIr) tip of the 25PtIr300A offers a better abrasion characteristic than the Pt probes. A further Pt probe from RMN is the 12Pt400B with a tip shank length of 80 μm (± 25 %), a cantilever length of 400 μm (± 15 %) and a cantilever width of 60 μm (± 15 %). The nominal spring constant is 0.3 N/m (± 40 %) and the resonance frequency 4.5 kHz (± 30 %).
The tested full metal cantilevers suffer more from tip wear compared to diamond or silicon cantilevers. Hence, full metal tips are not suitable for samples with a challenging topography. A better wear characteristic is required, which can be achieved by using metal coated silicon cantilevers. NanoWorld provides different kinds of metal coated silicon probes. The NanoWorld PtSi-Cont and PtSi-FM probes are in principal designed for applications operating at lower frequencies than SMM, e.g. SCM, EFM and Kelvin Probe Force Microscopy (KPFM). The probes are based on silicon cantilevers with a platinum-silicide (PtSi) coating. While the coating is the same for both probes, the PtSi-Cont is designed for contact mode AFM. In contrast, PtSi-FM is a cantilever originally designed for frequency modulation (FM) AFM modes. Both probes have been tested in SMM. The PtSi-Cont probes gave little signal contrast, but the PtSi-FM probes showed promising results. Table 3 shows the data sheet specifications of both probes. The largest differences between both types of probes can be observed in the cantilever width and length. Hence, those are promising parameters to investigate for cantilever optimization.

Table 3: Data sheet values of the two NanoWorld cantilevers PtSi-FM and PtSi-Cont and the parameters of the SMM probe modeled in finite elements method (FEM).

	PtSi-FM	PtSi-Cont	FEM model
Resonance frequency $/kHz$	45-115	6-21	x
Spring constant $/(N/m)$	0.5-9.5	0.02-0.77	x
Cantilever width $/\mu m$	20-35	42.5-57.5	25
Cantilever length $/\mu m$	215-235	440-460	225
Cantilever thickness $/\mu m$	2-4	1-3	3

4.3 Finite Elements Method

In order to find out which parameters do have an important influence on the transmission of the microwave through the probe, a FEM model of the probe was developed. FEM is a numerical method to solve boundary value problems. Besides FEM, there are two further methods to develop numerical models, the finite difference time domain (FDTD) and the method of moments (MoM). FDTD is mainly used for non-sinusoidal problems, which can easily be described in time domain. SMM poses a sinusoidal problem, preferably to be solved with MoM or FEM. MOM provides benefits in boundary definitions, as the free space between objects does not need to be defined and meshed. Nonetheless, material flexibility in MOM provides some problems. Here, FEM is used for the modeling because it provides the best combination of frequency dependent simulation and material flexibility. The FEM model built in this work is based on the PtSi-FM specifications. The right column of table 3 lists the parameters implemented in the model. Ansys HFSS was chosen over Keysight EMPro as software to perform the FEM simulation, as the HFSS parameter sweep capabilities were superior. HFSS provides the possibility to perform parameter sweeps in combination with stepped additional parameters. It was not possible to validate the model by measuring the probe due to the lack of a suitable HF connection of the probe. Therefore, the model was duplicated in EMPro to confirm the principle validity. The reflection and transfer characteristics could be confirmed. Figure 34 shows an overview of the model built in HFSS. The chip material was chosen as a conductor with a conductivity of 10000 S/m to match the highly doped silicon used for the chip. The cantilever and tip are modeled of the same material. Figure 35 shows the tip-sample interface in more detail. The tip radius was chosen with 100 nm, i.e. the radius of a rather worn out tip. Tip and cantilever are coated with a platinum layer of 20 nm. The coating covers the entire cantilever and chip. At the far end of the chip,away from the tip, port 1 is defined. It consists of two terminals. Terminal 1 is the face of the coating at the model boundary and terminal 2 is the ground plane defined below the sample, see fig. 34. The probe-sample-system, detailed in fig. 35, is modeled as a capacitance consisting of a copper layer with an SiO_2 layer on top. This structure enables

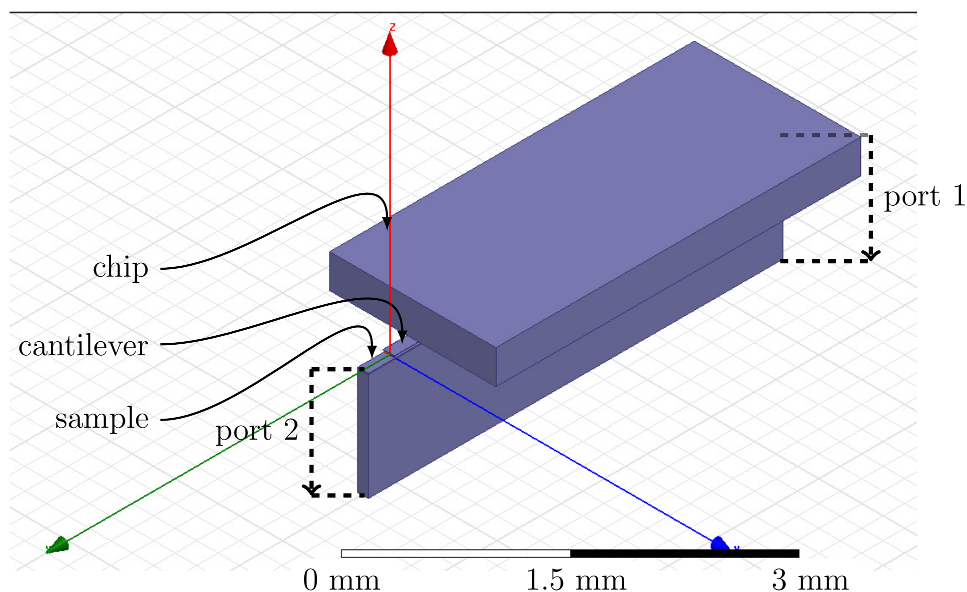

Figure 34: FEM Model of the AFM SMM probe with chip, cantilever and sample. The conductive sample is isolated to the perfect electrical conductor (PEC) ground plane. Port 1 is defined with its terminals being the conductive coating below the chip and the PEC ground plane. Port 2 terminals are the conductive sample and the PEC ground plane.

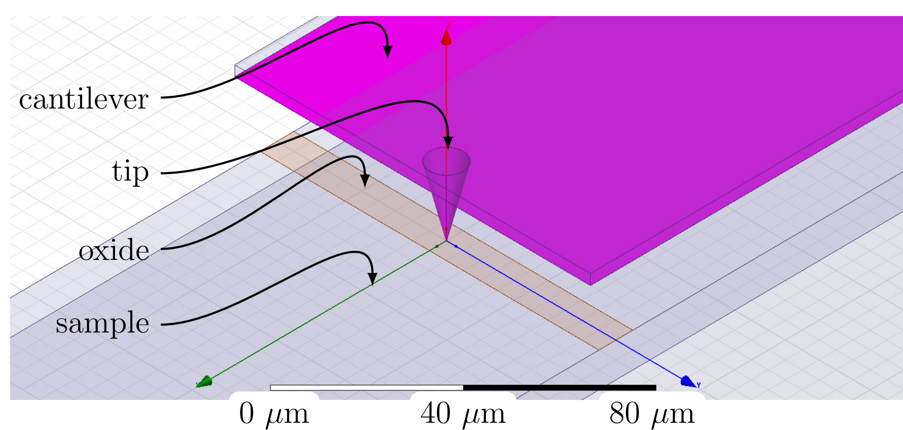

Figure 35: The tip-sample interface in more detail. The sample is modeled as a copper plate with an oxide layer on top. The oxide layer is modelled as a single stripe to reduce the number of elements. Cantilever and tip are covered with a Pt-coating, highlighted in lilac.

the simulation of the sensitivity on small capacitive changes. The oxide layer thickness was varied between 20 nm and 40 nm to simulate the small capacitive changes. The copper layer is insulated to the ground and can therefore be used as port 2, with the copper layer being terminal 1 and the ground plane terminal 2. The environment boundary, where the boundary conditions are applied, is set at 3 mm distance from the bottom, top, left and right of the structure, the maximum distance at which the simulation converged. The boundary condition was chosen as PEC. This is realistic for the bottom and top boundaries, as the ground contact and the shielded cantilever holder are close to the cantilever under measurement conditions. For the boundaries on the sides, the best solution would have been to apply a combined Dirichlet (1st order) and Neumann (2nd order) boundary condition, called 3rd order boundary condition, and manually adjust it in order to avoid bending of E-field lines. Unfortunately, neither HFSS nor EMPro offer a manual boundary condition. Only pre-defined boundary conditions were available. The available radiation boundary condition was tested for the model. The radiation boundary, when placed at the maximum still convergent distance, absorbs a too high amount of energy for this model to be realistic. The PEC boundary condition was also tested and provided realistic energy losses when compared to the radiation boundary condition. As a result, the PEC was applied for all environment boundaries. Using this model, the cantilever lengths of 225 μm of the PtSi-FM probe was compared with the 450 μm of the PtSi-Cont probe. A frequency sweep between 1 GHz and 20 GHz was performed. The maximum deviation between the sweeps with 20 nm and 40 nm oxide layer thickness was taken as the sensitivity. While the maximum difference of the PtSi-FM was 0.0358 dB, the sweep with 450 μm cantilever length showed no sensitivity the capacitive change. Therefore, the PtSi-FM was chosen for the evaluation of tunable parameters. Various parameters were varied, such as chip length and thickness and cantilever width and thickness and the coating thickness. It was observed, that the cantilever width as well as the coating thickness had an important influence on the SMM signal. The upper part of table 4 lists the resulting sensitivities for various values of cantilever width and coating thickness. The maximum difference achieved through a variation of cantilever width is 0.0206 dB. The maximum difference due to oxide thickness variation is 0.0419 dB.

Table 4: The upper table shows the simulated sensitivity on a small capacitive change, investigated by varying the oxide thickness from 20 nm to 40 nm. The lower table shows the sensitivity monitored through the maximum signal difference between highest and lowest signal at different dopant densities on the calibration sample at first measurement with a new tip.

FEM simulation results for tip-sample capacitance sensitivity [dB]			
Cantilever width /height [μm]	20nm Pt-coating	60nm Pt-coating	120nm Pt-coating
105 / 3	0.0511 dB	0.0693 dB	0.0542 dB
65 / 3	0.0256 dB	0.0675 dB	0.0455 dB
25 / 3	0.0358 dB	0.0543 dB	0.0629 dB
SMM measurement results ($d\underline{S}_{11}/dV$ [a.u.])			
Cantilever width /height [μm]	23nm Pt-coating	60nm Pt-coating	120nm Pt-coating
57.5 / 5	0.0052	0.0012	0.0041
47.5 / 1	0.0001	x	x
27.5 / 3	0.0004	0.0008	0.0034

There is no clearly observable trend, but the parameter variations do influence the results. A wider cantilever and a thicker oxide seem to be most promising in order to achieve a high sensitivity.

For comparison of simulation results with experiment, NanoWorld manufactured cantilevers of different widths and coatings. These cantilevers were used for SMM measurements on the calibration sample. The maximum dS_{11}/dV signal difference in between the highest and the lowest signal on the differently doped stripes was taken as a measure for the sensitivity. The measured dS_{11}/dV sensitivity is listed in the lower part of table 4. These measurements show the highest signal for large cantilever widths and heights. A similar trend could be confirmed for thick coatings through the measurements. An increased coating thickness leads in most cases to an increased sensitivity. However, as one outlier, the 57.5 μm wide and 5 μm high cantilever, the largest available, with the thin Pt-coating of 23 nm, offered the best sensitivity in test. After wear, those cantilevers even provided a well enough SNR to allow the capacitance calibration.

As a result of the improvements for SMM experiments suggested by the FEM simulations, the Pt-coated cantilevers were found a suitable alternative to the

full metal cantilevers and could improve scanning samples with a challenging topography. Furthermore, in future research, an additional insulation layer combined with a shielding of the SMM probes has the potential to further improve those cantilevers. In summary, FEM in combination with SMM experiments offers great potential to systematically improve measurement accuracy.

5 Quantitative Dopant Profiling by SMM

The characterization of semiconductor dopants plays an essential role in device development, failure analysis, and process monitoring. SMM offers plenty of different methods to probe the dopant type and density in state-of-the-art semiconductor devices [41, 79, 80]. However, the complexity of the SMM measurement still poses a challenge for the reliable and reproducible determination of dopant type and density. Previous methods do not acquire all relevant data in one image. Some require multiple scans on the sample under investigation as well as a comparison to a calibration sample [41]. Others are not able to identify the doping type [79], only the dopant density, while additional point scans are needed to test for dopant type [80]. Hence, a reliable method for SMM is needed to simplify and speed up the estimation of dopant type and density in electronic devices [22].

5.1 Lateral Resolution

The most commonly used AFM probes, which are suitable for SMM, provide a tip radius down to 20 nm. This enables topography measurements with a high spatial resolution. Nevertheless, the effective tip radius for the SMM signal is not necessarily consistent with the mechanical tip radius. In addition to limitations in spatial resolution caused by the tip radius, the microwave excitation region and the SCRs beneath the semiconductor surface lead to an effective tip radius of a rather unknown size. The significance of this excitation region on the effective tip radius is yet still uncertain.

5.1.1 Experimental results

In order to determine the area of interaction below the scanning tip, a method is introduced to characterize the dimensions of the excitation region. The results of this study are published in ref. [81]. A standard AlGaN/GaN heterostructure is used to evaluate the effective excitation region in SMM. It offers a strongly confined two-dimensional electron gas (2DEG) and is ideally suited to characterize the resolution. The 2DEG was investigated in $d\underline{S}_{11}/dV$

imaging mode, using a VNA frequency of 16 GHz with low frequency modulation of 20 kHz applied through the lock-in amplifiers. The RMN 25Pt300A probe with a nominal tip radius of 20 nm was employed. Further investigations were performed with a PtSi-FM probe from NanoWorld and a tungsten-silicide coated probe EFM-EH from Team Nanotec.
An embedded cross-section of an AlGaN/GaN heterostructure was prepared in order to access 2DEG. Figure 36 shows the image acquired using the RMN 25Pt300A probe. It confirms that the 2DEG is highly confined at the AlGaN/GaN interface. The theoretical width of the 2DEG in the investigated AlGaN/GaN structure is below 5 nm, see inset of fig. 37 [82]. Considering the much wider signal shown in the dS_{11}/dV scan across the AlGaN/GaN interface in fig. 36, the 2DEG width is negligible in a first approximation. To get an idea of the effective tip radius, a profile was extracted from the scan across the 2DEG, plotted in fig. 37. The effective tip diameter and radius were estimated from the full width at half maximum (FWHM) of the profile. To gain

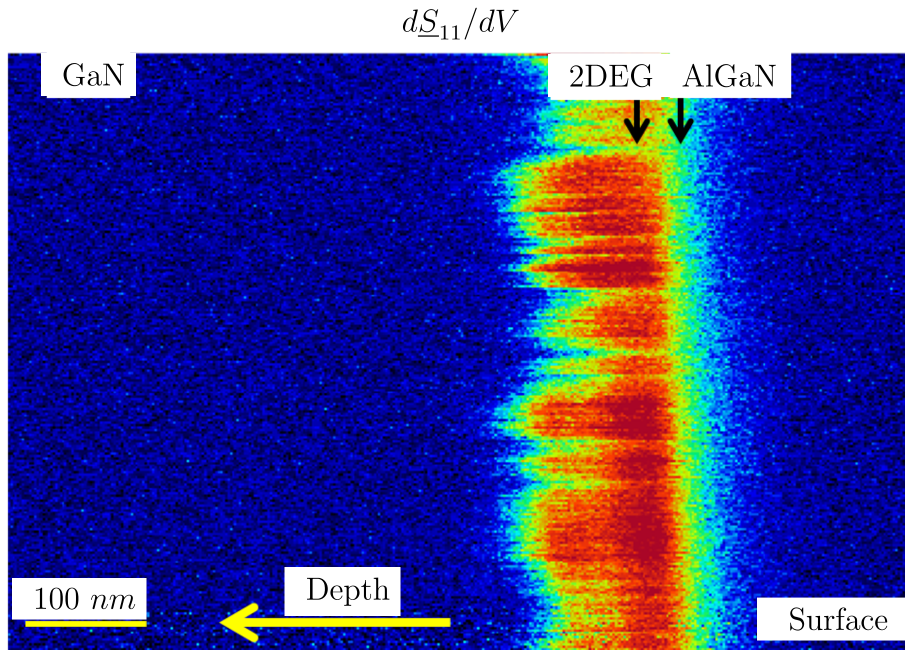

Figure 36: SMM $d\underline{S}_{11}/dV$ image obtained at the 2DEG of the AlGaN/GaN interface. The scan was performed with 0.2 lines/s, the fast scan axis was perpendicular to the AlGaN/GaN interface. An RMN 25Pt300A probe was used.

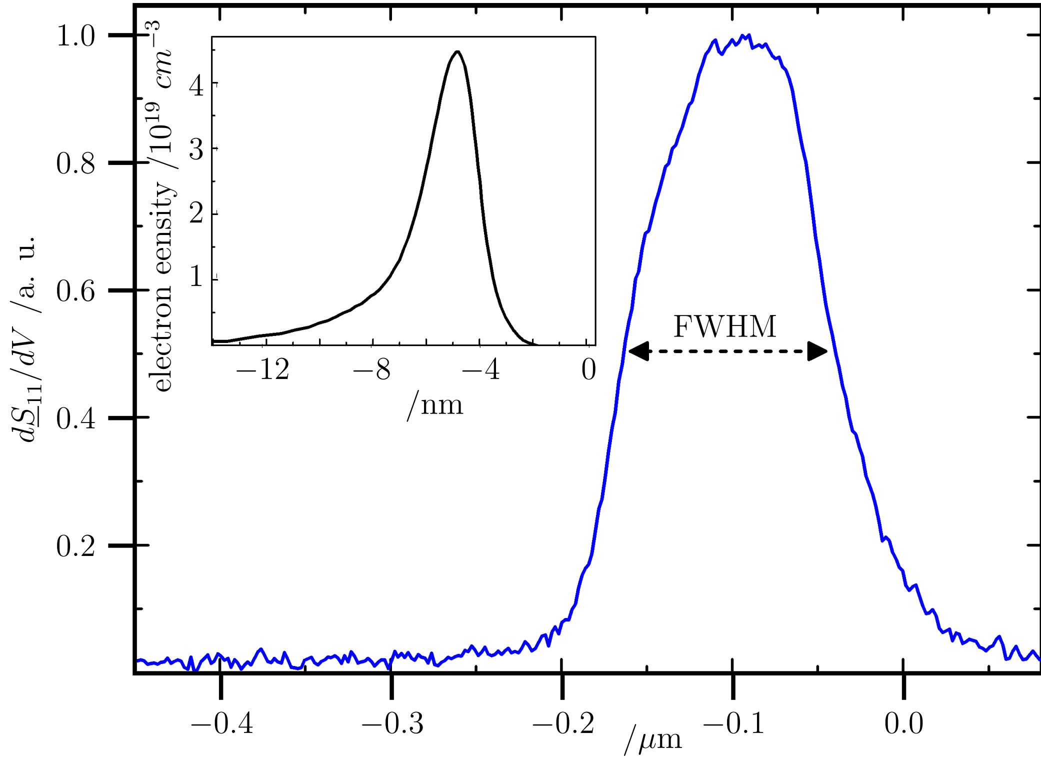

Figure 37: SMM $d\underline{S}_{11}/dV$ depth profile across the 2DEG, extracted from fig. 36 and normalized to the maximum signal. The FWHM indicates the profile width. The AlGaN/GaN interface is located at 0 *nm*. The theoretical electron density across the AlGaN/GaN interface reprinted after [82] is shown in the inset.

a comparable measure of the often uneven tip shapes, a Gaussian distribution was fitted to the resulting profiles and the respective FWHM was extracted. The profile revealed an effective tip radius of 60 nm. This deviation from the nominal 20 nm can either have a mechanical reason due to tip degradation or might be caused by the microwave excitation region influencing the spatial resolution. Since the extracted profile resembles the shape of the theoretical 2DEG profile, both having a tail towards the GaN bulk (seen fig. 37), the theoretical distribution of the electrons in the 2DEG needs to be considered. To extract the effective tip shape from the recorded profile, the profile was flattened to reduce the noise and deconvoluted with the theoretical profile. The resulting deconvoluted profile is depicted in fig. 38. When comparing the originally measured profile with the deconvoluted profile, the electron distribution

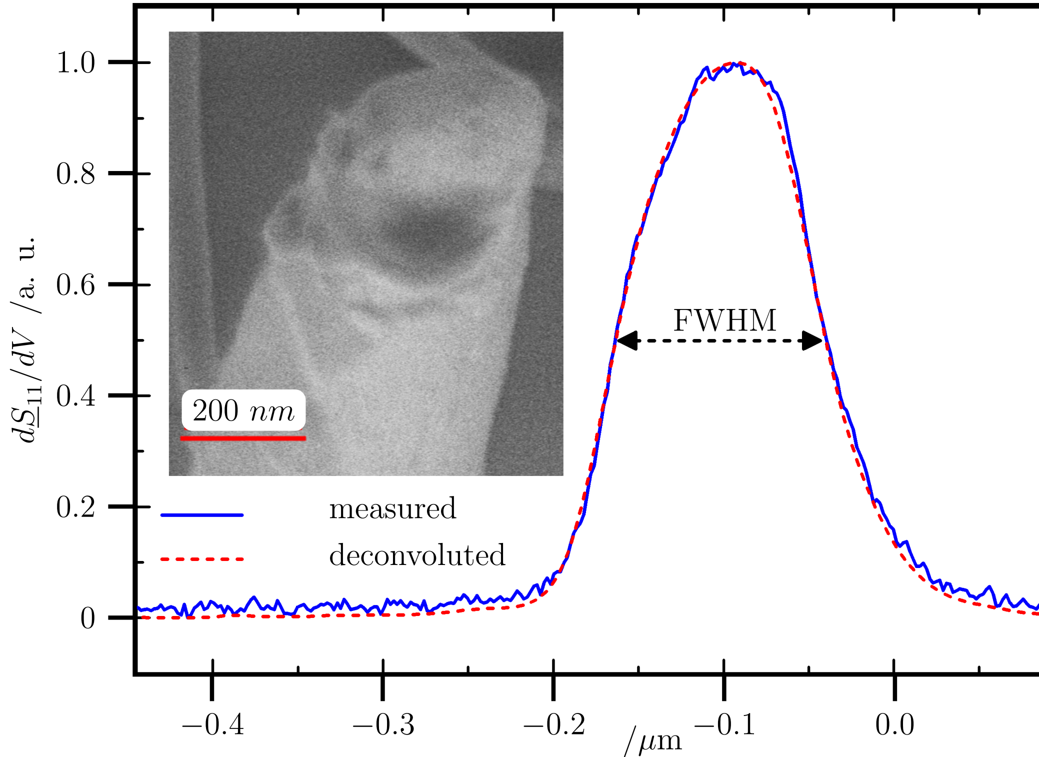

Figure 38: Measured and deconvoluted SMM profile recorded at the 2DEG with a 25Pt300A cantilever. The SEM image of the cantilever tip is shown in the inset.

in the 2DEG seems to only marginally influence the measured profile. This confirms the assumption that the 2DEG profile is nearly negligible when the 2DEG is used to characterize the tip and that the tip radius and shape have a high impact on the measurement results. The SEM image shown in the inset of fig. 38 was obtained after the SMM scans were performed. The shape of the tip resembles the shape of the SMM profile.
The scan with a different cantilever, Nanoworld PtSi-FM, depicted in fig. 39, also reveals a comparable similarity between tip shape in the SEM image and SMM profile. This agreement of shape and profile confirms the presented approach that the highly confined 2DEG scans the active tip shape and SMM properties. Since the shape of the cantilever tips is often uneven, the extraction of the active tip radius from SEM images is difficult. For the PtSi-FM cantilever (see fig. 39), a tip radius of about 500 nm was extracted from SEM,

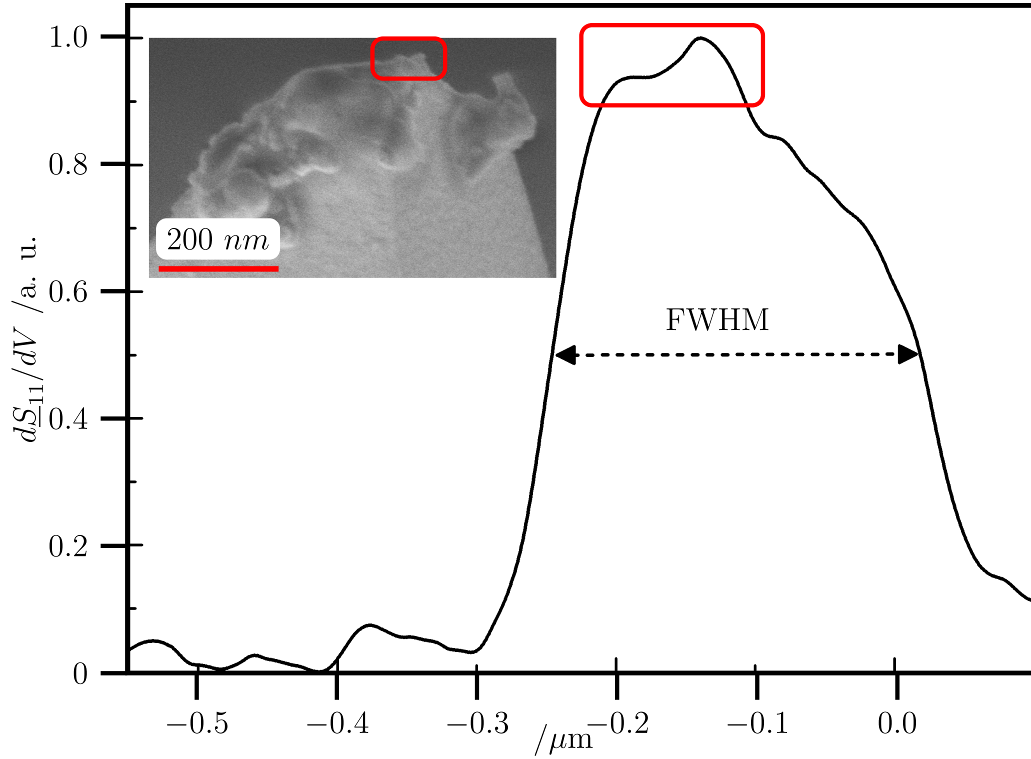

Figure 39: Deconvoluted SMM $d\underline{S}_{11}/dV$ 2DEG profile, obtained using a PtSi-FM cantilever. The inset shows an SEM image of the cantilever tip. The resembling structures responsible for the effective tip shape are marked in red.

while the SMM profile revealed an effective tip radius of 113 nm extracted from FWHM of the Gaussian profile fit. In case of the EFM-EH cantilever the SEM radius could be confirmed with the SMM profile, achieving an effective tip radius of about 50 nm (not shown).

5.1.2 Discussion

The SEM tip radius value of the used tip agrees well with the result from the SMM profile (see fig. 37), indicating the microwave excitation region not to have a severe impact on the spatial resolution of sharp cantilevers. However, for unevenly shaped and used cantilever tips, the microwave excitation region and therefore the effective tip radius can vary from the theoretical tip radius observed, e.g., in SEM. Here, the presented method proved to be ideally suited

for the evaluation of cantilever properties, usage, and effective tip radius for SMM measurements. SMM was demonstrated to resolve the 2DEG in a standard AlGaN/GaN heterostructure with high spatial resolution. Moreover, the 2DEG profile revealing the effective tip radius during SMM measurements was in agreement with the tip radius found using SEM images for sharp probe tips. Furthermore, the 2DEG profile was proven a superior tool to define the effective tip shape for unevenly shaped probe tips. From the SEM images, it was not possible to judge which part of the tip contributes to the signal. The effective tip shape contributing to the signal was obtained using the 2DEG profile. This shape could be correlated to the respective part in the SEM image. This confirms the method is able to characterize effective tip radius and quality.

5.2 Dopant Density by Resistivity

As summarized in section 3.3, most available SMM methods are lacking the ability to quantitatively probe the dopant density. Conventional approaches using the resistive response of the SMM signal typically gain resistivity and permittivity information by comparing data to simulations, like FEM models [34, 83–86]. To avoid this approach, an analytical model was developed in order to extract the dopant density information from the resistance calculated from measured SMM data [79]. The calculation of the error parameters for the calibration of the complex impedance is based on the approach to fit EFM and SMM capacitance, as explained in section 3.3.

5.2.1 Experimental results

The studies on dopant density by resistivity were carried out using the calibration sample with 1 μm wide stripes of varying dopant densities. The results are published in ref. [79]. The stripes were scanned by SMM with a frequency of 18 GHz. The error 2-port model was applied to the SMM data to correct the data and place the calibration plane at the tip-sample interface. To obtain the error parameters, they were used as fitting parameters to match the SMM capacitance to the simultaneously obtained EFM capacitance as described in section 3.3 [79]. Figure 40 shows the capacitance (a) and resistance (b) scan

acquired after calibration. Both capacitance and resistance show a monotonic dependency on the dopant density, which increases towards the center of the scan. Unlike in the parallel model applied in eqs. (6) and (7), a series model was applied to separate $\underline{Z}_{DUT}$ in capacitance and resistance.

$$\underline{Z}_{DUT} = R_{series} + \frac{1}{j\omega C_{series}}, \tag{29}$$

The series resistance itself, R_{series}, is modeled as a series of the surface resistance R_s and the sheet resistance R_x.

$$R_{series} = R_s + R_x \tag{30}$$

The surface resistance is given by

$$R_s = \frac{\rho}{\delta}, \tag{31}$$

where ρ is the resistivity of the scanned region and the skin-depth δ [40,79]. δ can be calculated as

$$\delta = \frac{1}{\omega}\frac{1}{\sqrt{\frac{\mu\epsilon}{2}(\sqrt{1+(\frac{1}{\omega\rho\epsilon})^2}-1)}}, \tag{32}$$

with permeability μ and permittivity ϵ of the silicon sample [79,87]. The sheet resistance is defined as

$$R_s = \frac{\rho}{d_{effective}}, \tag{33}$$

where $d_{effective}$ is the effective measure for the shortest path to the nearest ground [79]. It can be calculated by

$$d_{effective} = \frac{\pi r^2}{W_d}. \tag{34}$$

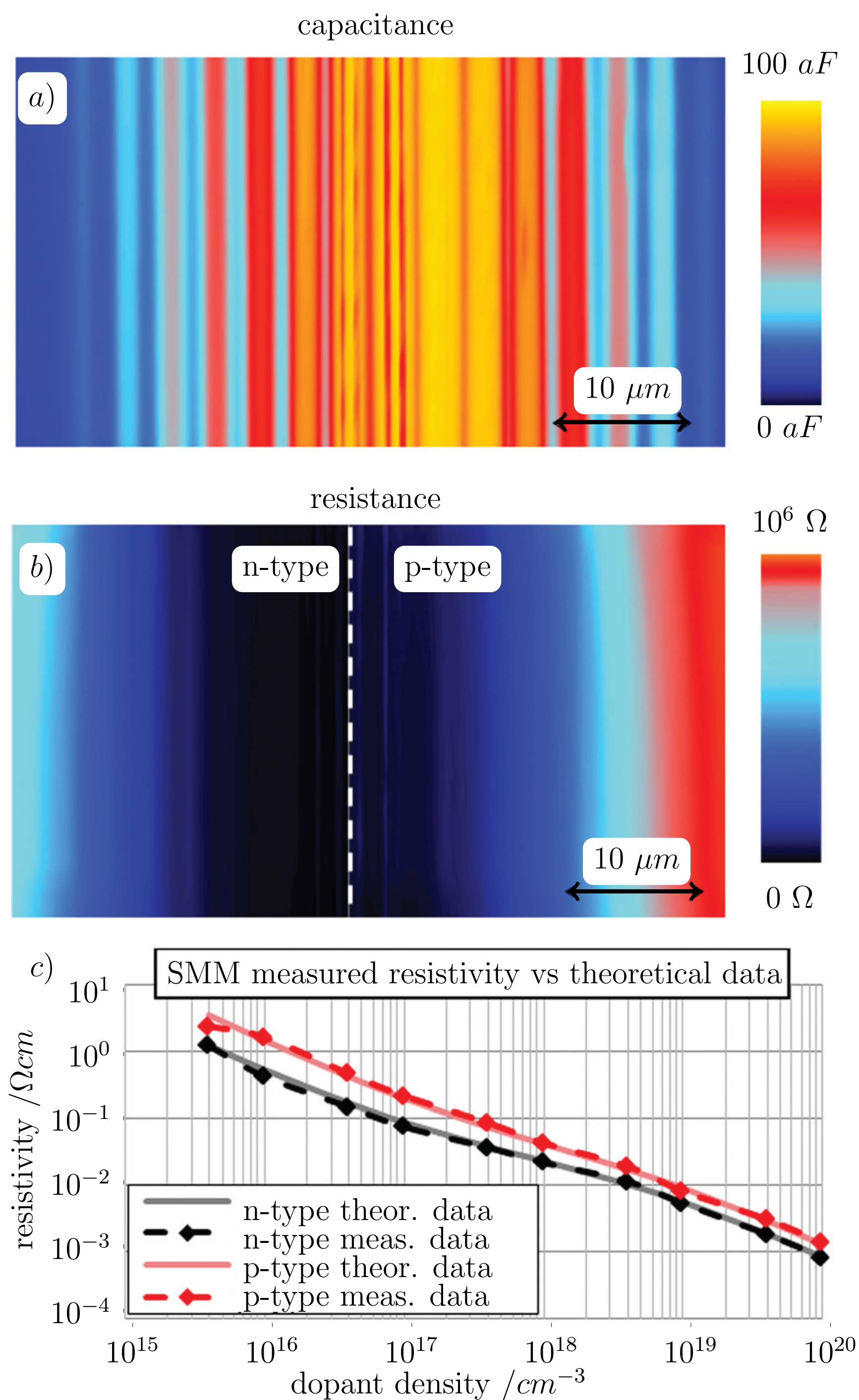

Figure 40: Calibrated SMM data including capacitance (a) and resistance (b) images. The resistivity in (c) is calculated from the calibrated resistance. The SMM resistivity is compared to the datasheet resistivity. Adapted from [79].

The tip radius r defines the contact area, while the SCR width W_d can be substituted with eq. (15) leading to:

$$d_{effective} = \frac{\pi r^2}{\sqrt{\frac{2\epsilon_{Si}\phi_s}{qN_x}}}. \tag{35}$$

The surface potential ϕ_s has to be known to solve the equation. Usually, it has to be calculated like shown in section 2.2.2 leading to an equation involving all internal potentials. For the given measurements, neglecting all potentials not directly related to the interface, ϕ_s was estimated as metal semiconductor work function difference ϕ_{ms}, see eqs. (11) and (12) [79]. Substituting R_s and R_x leads to

$$R_{series} = \rho(\frac{1}{\delta} + \frac{W_d}{\pi r^2}). \tag{36}$$

To calculate the relation between R_{series} and ρ, the tip radius r is required. An analytical model was used to calculate r from the approach curves [88–90]. The fit of this analytical model to the approach curves delivered values between $r = 100\ nm$ and $r = 2\ \mu m$ for different used tips [79]. With the tip radius known, eq. (30) can be solved for ρ.

$$\rho = R_{series}(\frac{\delta \pi r^2}{\delta W_d + \pi r^2}) \tag{37}$$

The dopant densities were then calculated from ρ using the relation

$$\rho = \frac{1}{q(\mu_n N_D + \mu_p N_A)}, \tag{38}$$

where μ_n and μ_p are the respective carrier mobilities of electrons and holes in silicon [79]. Figure 40 (c) shows the resistivities and dopant densities calculated from the resistance image. From the blurry resistance image it is difficult to assign the right values to the corresponding dopant stripes. However, both resistivities and dopant densities match the corresponding datasheet values plotted in fig. 40 (d) quite well [79]. Nonetheless, there is a chance that picked values are slightly off the assigned dopant stripe.

The second investigated sample provides 5 n-type dopant densities ranging between 10^{14} atoms cm^{-3} and 10^{19} atoms cm^{-3}, produced by IMEC. All layers are epitaxial, making the dopant density homogeneous in depth. A cross-section was performed to make the bulk of the sample accessible. The scan of the cross-section was also preformed with a frequency of 18 GHz. The calibration flow described above was applied to the data. Figure 41 (a) shows the resistance image acquired during the scan. It confirms the monotonic trend of increasing resistance with decreasing dopant densities observed on the calibration sample. The decreasing capacitance with decreasing dopant density is depicted in fig. 41 (b). Figure 41 (c) shows the resistivity and dopant density image calculated from the resistance image. Figure 41 (d) shows the extracted profiles and datasheet values provided by IMEC. The profile confirms a very good accuracy of dopant density with expected values within one order of magnitude [79].

5.2.2 Discussion

The plotted resistivity and dopant density results represent an accurate approach for quantitative dopant profiling with SMM. Both samples could be characterized in good quantitative agreement with the datasheet values. The error values were calculated from the logarithmic difference between values calculated from SMM data and datasheet values plotted in fig. 41 (d). The error was found 54 % in the area with 10^{18} atoms cm^{-3}, 18 % in the area with 10^{17} atoms cm^{-3}, 5 % in the area with 10^{16} atoms cm^{-3}, 28 % in the area with 10^{15} atoms cm^{-3} and 36.5 % in the area 10^{14} atoms cm^{-3}. The estimated error bars confirm a good accuracy of the calibration method for average doped regions. The higher error values for highly and lowly doped regions are possibly related to boundary assumptions implemented in the calibration method [79]. The validity of this method is fine for the measurements of the homogeneously doped epitaxial sample.
The skin depth values used for the calculation of the dopant densities range from 0.7 mm for low p-type densities and 0.4 mm for low n-type densities to 10 μm for high p-type densities and 9μm for high n-type densities [79]. As the skin depth is an important parameter in the resistivity calculation, the method

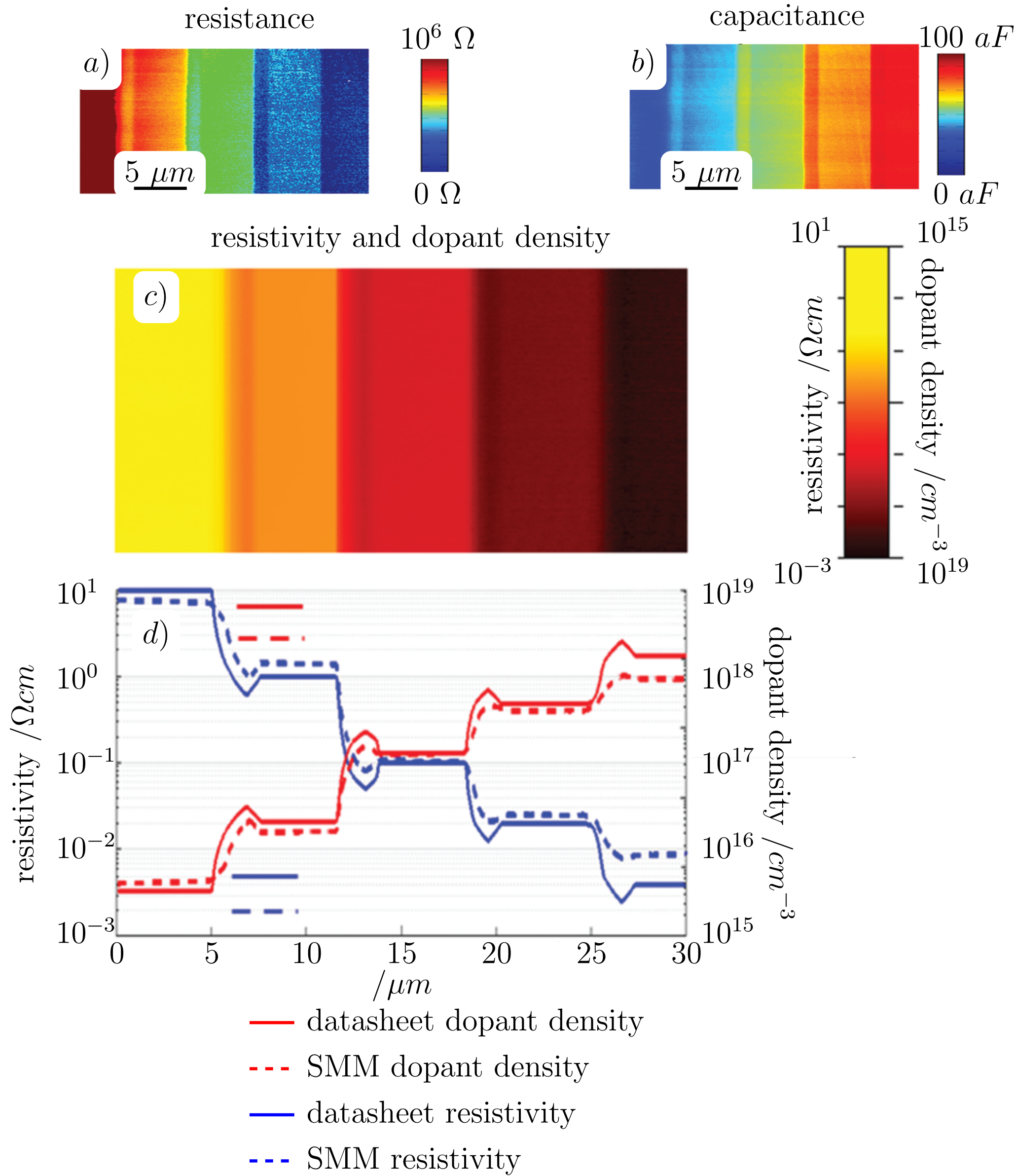

Figure 41: SMM resitance (a) and capacitance (b) data of the IMEC n-type Si dopant sample. The sample has different n-doped areas with doping concentrations ranging from 10^{15} to 10^{19} atoms cm^{-3}. The 5 μm wide doping areas are separated by 1 μm wide bulk interface layers as observed also in the capacitance and resistance images. The resistivity and doping concentration (c) are calculated from the SMM resistance based on the tip/sample analytical model. (d) Comparison of SMM resistivity and doping concentration values extracted from (c) to the datasheet values (provided by IMEC) determined with SIMS. Adapted from [79].

can deliver quite reasonable results for an epitaxial sample with a homogeneous dopant density across depth. In contrast, for the calibration sample providing both p- and n-type densities, the dopant density is only homogeneous for the first 200 nm of sample depth for the low dopant densities and below 1 μm for the high densities [41]. Consequently, the skin depth exceeds the homogeneous dopant density and therefore, an inhomogeneous material would have to be considered for the calculation of the dopant densities. The depth of the homogeneous region needs to be known in advance. Furthermore, an intrinsic potential or even a p/n junction would have to be considered for the calculation of the surface potential and thus the SCR. This adds an error to the assumption that the surface potential is equivalent to ϕ_{ms}. This error influences the eqs. (36) and (37) and the data shown in fig. 40 (c). Another error originates from a different metal work function difference for n-type Si, which has to be considered. Taking into account those influences, the method can be improved further.

The data was acquired in the Keysight Laboratories in Linz. The reproducibility of the calibrated capacitance and resistance data was tested with a similar setup at Failure Analysis laboratories of Infineon Technologies AG in Munich. The capacitance calibration worked fine for the capacitance data in almost all tested cases. In the few exceptions a proper calibration could be achieved with a slight adjustment of the microwave frequency and a repeated calibration procedure. As for the resistance data, only two of twelve datasets could be used for further processing. In all other cases, the data was either too noisy or too blurry to differentiate the different dopant densities. Besides the lack in reproducibility, the method provides the best accuracy for homogeneously doped semiconductors. Nevertheless, as known from resistivity measurements in SSRM, this method offers no opportunity to get information on the dopant type, p- and n-doped silicon cannot be distinguished.

In conclusion, the introduced resistance method is a suitable way to gain information on the dopant density, but a reliable method is still required to obtain a spatially resolved distribution of dopant type.

5.3 Dopant Type and Density by Capacitance

In order to obtain information about the dopant type and at the same time measure quantitative densities with a high reproducibility, a method based on calibrated capacities was developed. Part of those results are published in ref. [22]. The calibration through error parameters calculated by fitting EFM and SMM capacitance as shown before in section 3.3 was performed to calibrate the reflected microwave and calculate capacitance and conductance. To find solutions on the dopant type determination, a p-type sample developed by IMEC was examined in combination with the calibration sample. This additional sample consists of different stacked epitaxial layers with boron densities ranging from 3.8x10^{15} atoms cm^{-3} to 7.5x10^{19} atoms cm^{-3} and a p-type Si substrate doped with 2.3x10^{15} atoms cm^{-3}. Figure 42 shows the datasheet profiles of the boron densities and the corresponding resistivities of the different epitaxial layers, acquired by SRP. The sample was cross-sectioned in order to access the different epitaxial layers across depth. Other than a final polish using a colloidal silica suspension, no oxidation steps were performed to maintain a thin oxide layer.

5.3.1 Spectroscopy

A possibility to define the dopant type in SMM is to use the slope of the C-V characteristics. When the tip bias is swept from negative to positive voltage, a p-type semiconductor goes from accumulation to depletion. Therefore, the slope of the C-V curve is negative. An n-type semiconductor is driven from depletion to accumulation with the same sweep, thus showing a positive slope in the C-V curve. Therefore, C-V spectroscopy curves were recorded to verify the accuracy of SMM C-V to be sufficient for dopant type determination. The measurements were carried out on the p-type epitaxial sample. The DC bias of the AFM tip was swept from -4 V to +4V at one point on each of the epitaxial layers. The resulting C-V spectra are shown in fig. 43. For all acquired C-V curves, a clear p-type behavior, meaning a negative slope, was observed. The only exception is the curve acquired on the epitaxial layer doped with 3.8x10^{15} atoms cm^{-3} dopant density. This curve does not allow to extract a positive or

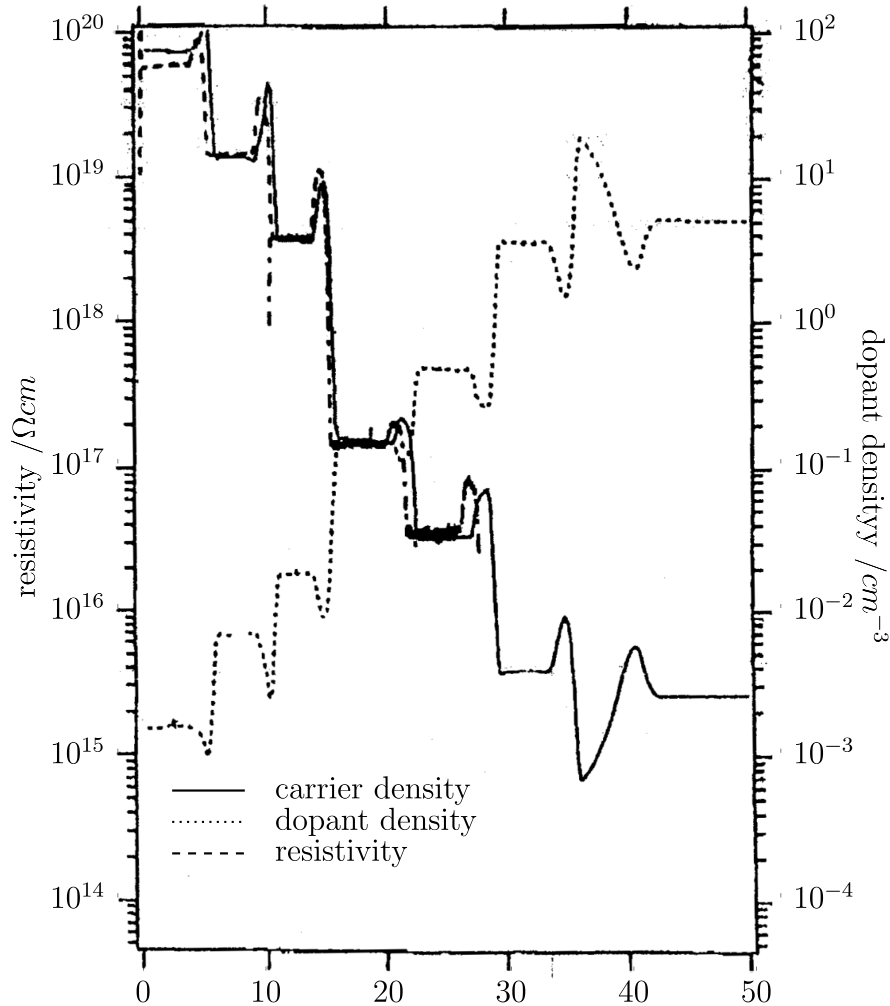

Figure 42: Boron densities and resistivities of the IMEC-T8 sample adapted from datasheet. The datasheet includes the intended carrier density and SRP measurements of resistivity and dopant densty.

negative slope out of the noise. Nonetheless, the spectroscopy curves prove, that an identification of the dopant type is possible down to 3.8x10^{15} atoms cm^{-3} with the chosen measurement frequency of 19 GHz and down to 3.2x10^{16} atoms cm^{-3} when the microwave frequency is 4 GHz. The difference between the accumulation capacitance at -3 V and the depletion capacitance at +3 V can therefore be used to determine the dopant type, further called ΔC.
The slope of the C-V curves is expected to increase with decreasing dopant

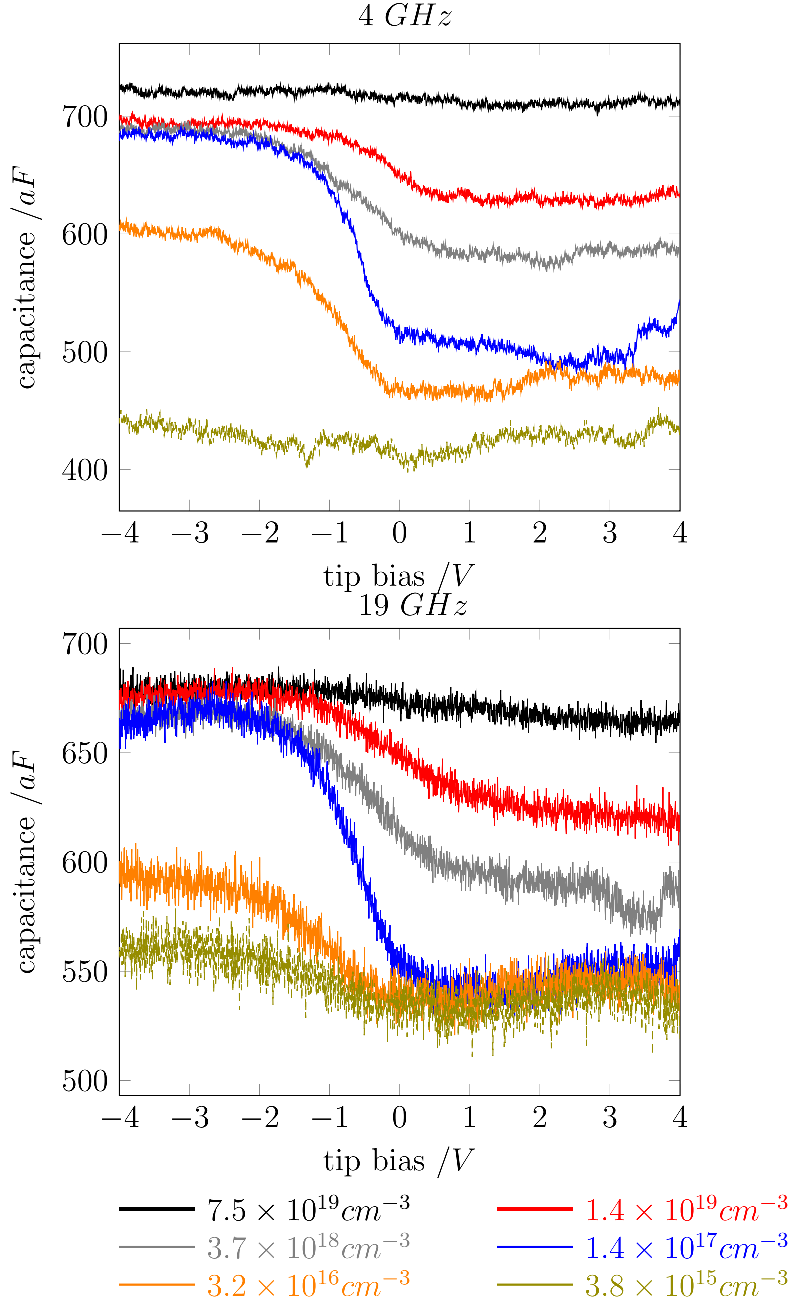

Figure 43: C-V characteristics recorded on boron doped epitaxial layers of the IMEC T8 silicon sample. The tip bias was swept from -4 V to +4V at each density. The curves show a clear p-type behavior. For the lower densities a reduced accumulation capacitance is obtained.

densities, as expected for HF C-V characteristics [19–21]. However, for the C-V characteristics shown in fig. 43, this is only true for dopant densities above 1.4x10^{17} atoms cm^{-3}. For dopant densities below 3.2x10^{16} atoms cm^{-3}, the accumulation capacitance at negative tip bias values does not reach oxide capacitance level any longer. This effect, known from C-V characteristics in a lower frequency range where it occurs for highly resistive substrate, can be transferred to the GHz measurements in SMM due its frequency and series resistivity dependencies [23–26]. While this effect causes a non-monotonic dependency of the C-V curves slope on the dopant density, the depletion capacitance scales with the dopant density over the entire density range investigated here. Hence, the depletion capacitance can be used to determine the relation between the differently doped layers.
Since the noise in the C-V curves obtained at 19 GHz is untypically high, it can be removed by flattening the curve. However, the noise in the 4 GHz curves is random and cannot be removed. Therefore, the noise influence on the dopant type detection is worse for the lower measurement frequency, which makes 19 GHz a more suitable measurement parameter in terms of SNR.

5.3.2 Dopant Type

Since the acquisition time for the spectroscopy curves is quite high, recording the C-V characteristics of a whole SMM image would take several hours to days with the given setup. Instead of acquiring the whole C-V curve, measurements were performed with a negative tip bias of -3 V and a positive tip bias of +3 V to image the epitaxial sample in accumulation and depletion condition, reducing the scan time tremendously. This was done within one measurement by scanning each line twice. The imaging frequencies were 4 GHz and 19 GHz. Figure 44 (a) and fig. 45 (a) show the p-doped sample in depletion condition. For both frequencies, 4 GHz and 19 GHz, the positive charges were depleted from the semiconductor surface. The depletion capacities scale with the dopant densities.

Figure 44 (b) and fig. 45 (b) show the sample data obtained with a negative tip bias of -3 V. Due to the negative tip bias, the positive carriers accumulate and the sample is measured in accumulation condition. The data obtained at

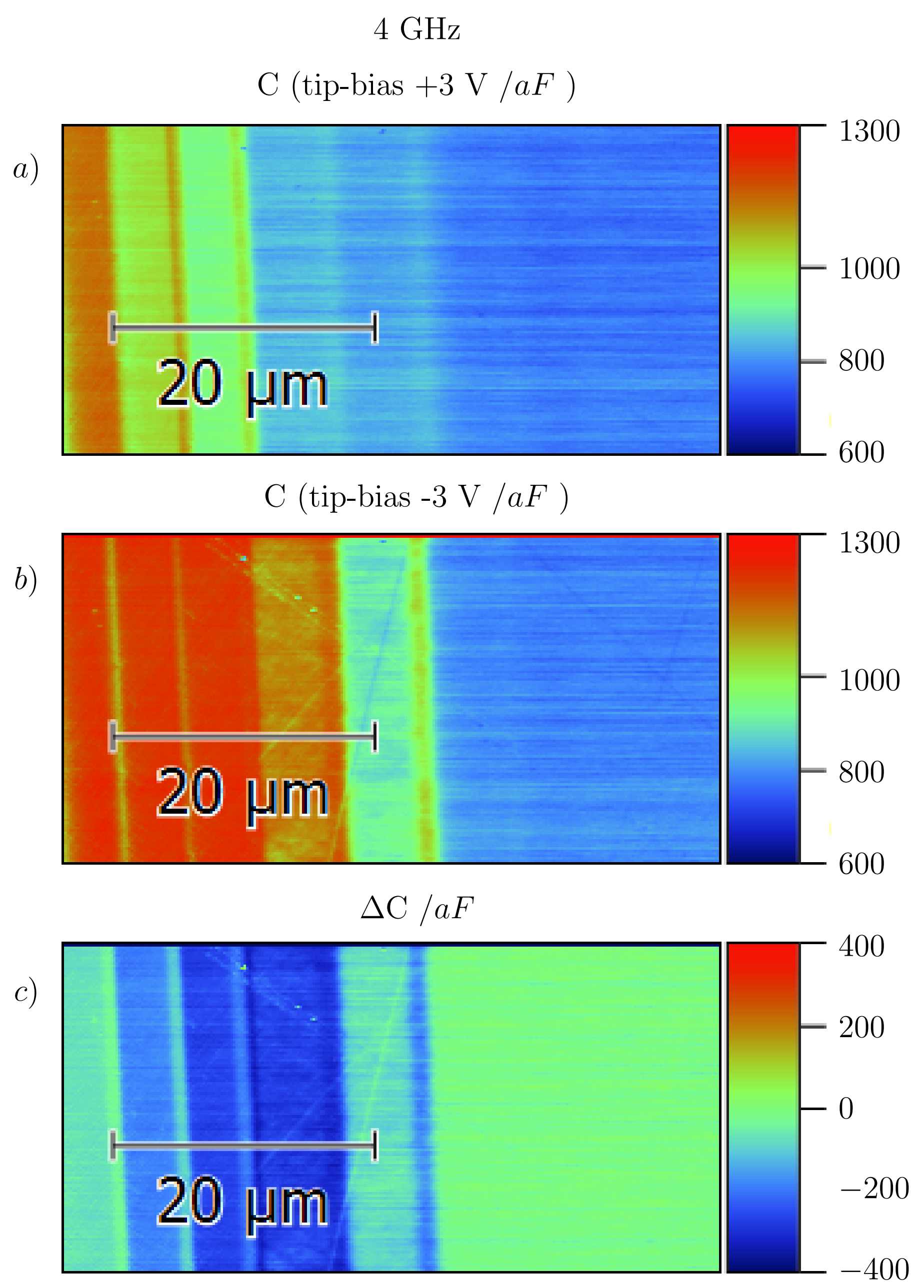

Figure 44: Capacitance images obtained at the p-doped epitaxial layer of an IMEC T8 sample. The microwave frequency was 4 GHz. The images were acquired with +3 V DC bias (a) and -3 V DC bias (b). ΔC (c) depicts the difference of (a) and (b). ΔC represents the slope of the C-V curves, positive values correspond to the positive slope of n-type C-V curves and negative values to the negative slope of p-type C-V curves.

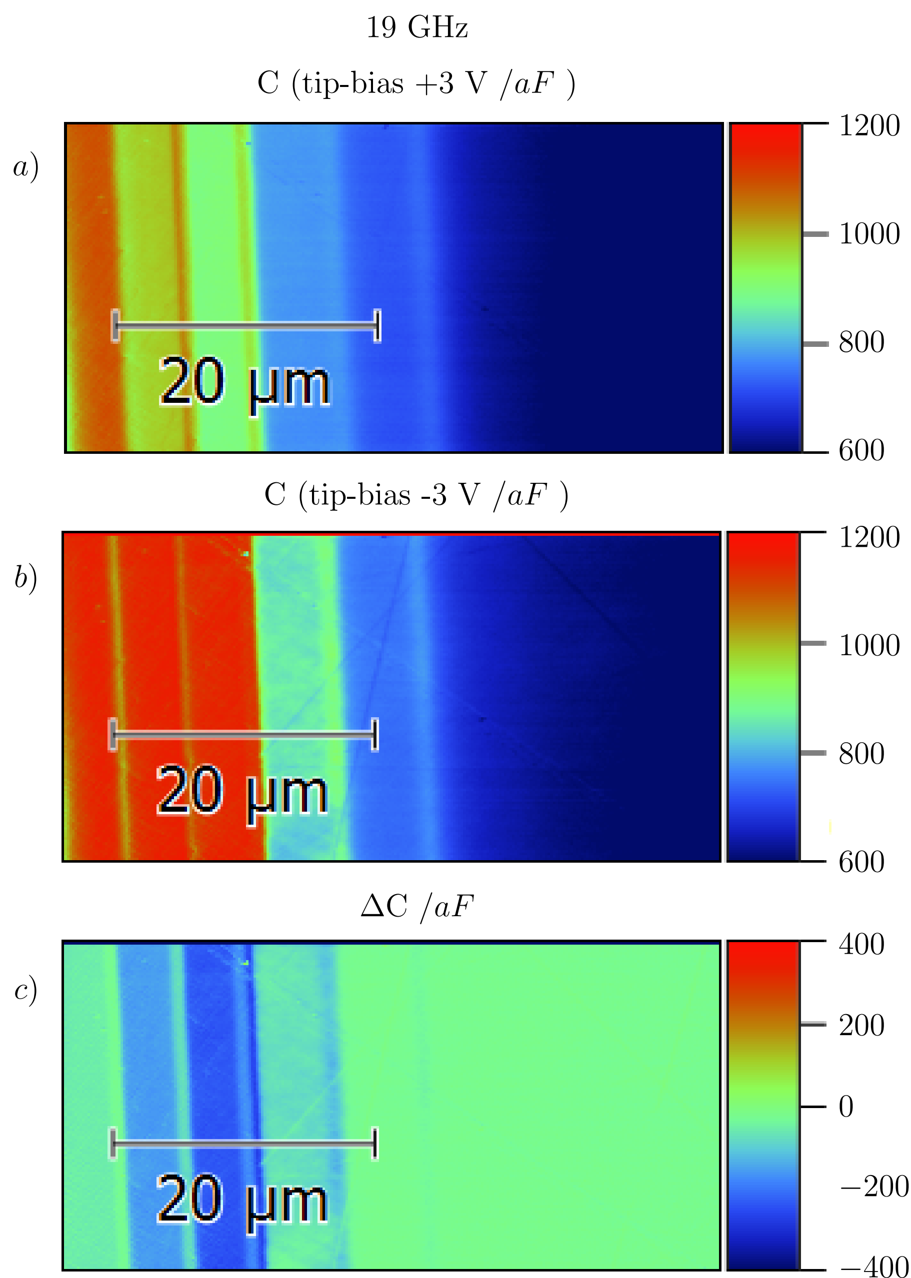

Figure 45: Capacitance images obtained at the p-doped epitaxial layer of the IMEC T8 sample. The microwave frequency was 19 GHz. The images were acquired with +3 V DC bias (a) and -3 V DC bias (b). ΔC (c) depicts the difference of (a) and (b). ΔC represents the slope of the C-V curves, positive values correspond to the positive slope of n-type C-V curves and negative values to the negative slope of p-type C-V curves.

a measurement frequency of 19 GHz shows accumulation capacitance values close to oxide capacitance level down to a dopant density of 3.7x10^{18} atoms cm^{-3}. For lower dopant densities, a reduced accumulation capacitance is measured. This frequency dependent effect is known from C-V characteristics at highly resistive substrate. It is related to the series resistance, more specifically the majority carrier mobility [23, 24]. Since the effect is frequency dependent the capacities measured at 4 GHz are still close to oxide capacitance level at a lower dopant density of 1.4x10^{17} atoms cm^{-3}.

To determine the dopant type, the accumulation and depletion datasets were combined. The data acquired with a negative bias shown in fig. 44 (b) and fig. 45 (b) was subtracted from the data acquired with a positive tip bias shown in fig. 44 (a) fig. 45 (a). The resulting capacitance difference ΔC is plotted in fig. 44 (c) and fig. 45 (c). This data can now be used to determine the dopant type, as negative values correspond to a negative slope in C-V characteristics and thus indicate a p-type semiconductor, and positive values correspond to a positive slope indicating an n-type semiconductor. Figure 44 (c) and fig. 45 (c) clearly show a p-type semiconductor for higher dopant densities. For lower dopant densities, the lowered accumulation capacitance is so close to depletion capacitance, so that ΔC is close to zero and therefore p- and n-type cannot be clearly distinguished. This can be observed for densities below 3.2x10^{16} atoms cm^{-3} at 19 GHz (see fig. 45 (c) and below 3.8x10^{15} atoms cm^{-3} at 4 GHz (see fig. 44 (c), which again agrees with the frequency dependency reported in literature [23–26]. Consequently, lower frequencies are supposedly better suited to determine the dopant type. Nonetheless, the higher measurement frequency provides the better SNR.

Similar measurements were performed on the calibration sample. The microwave frequencies used for those measurements were 6 GHz and 16 GHz. The obtained C and ΔC distributions are shown in fig. 46. The data obtained with a positive tip bias is shown in fig. 46 (a) and (d). The positive bias accumulates the negative charge carriers of the n-doped silicon on the left and depletes the positive charge carriers on the right. The data obtained with a negative tip bias is shown in fig. 46 (b) and (e). Here, the negative charge carriers of the n-doped silicon are depleted and the positive carriers accumulated. Again the accumulation capacitance is close to oxide capacitance level

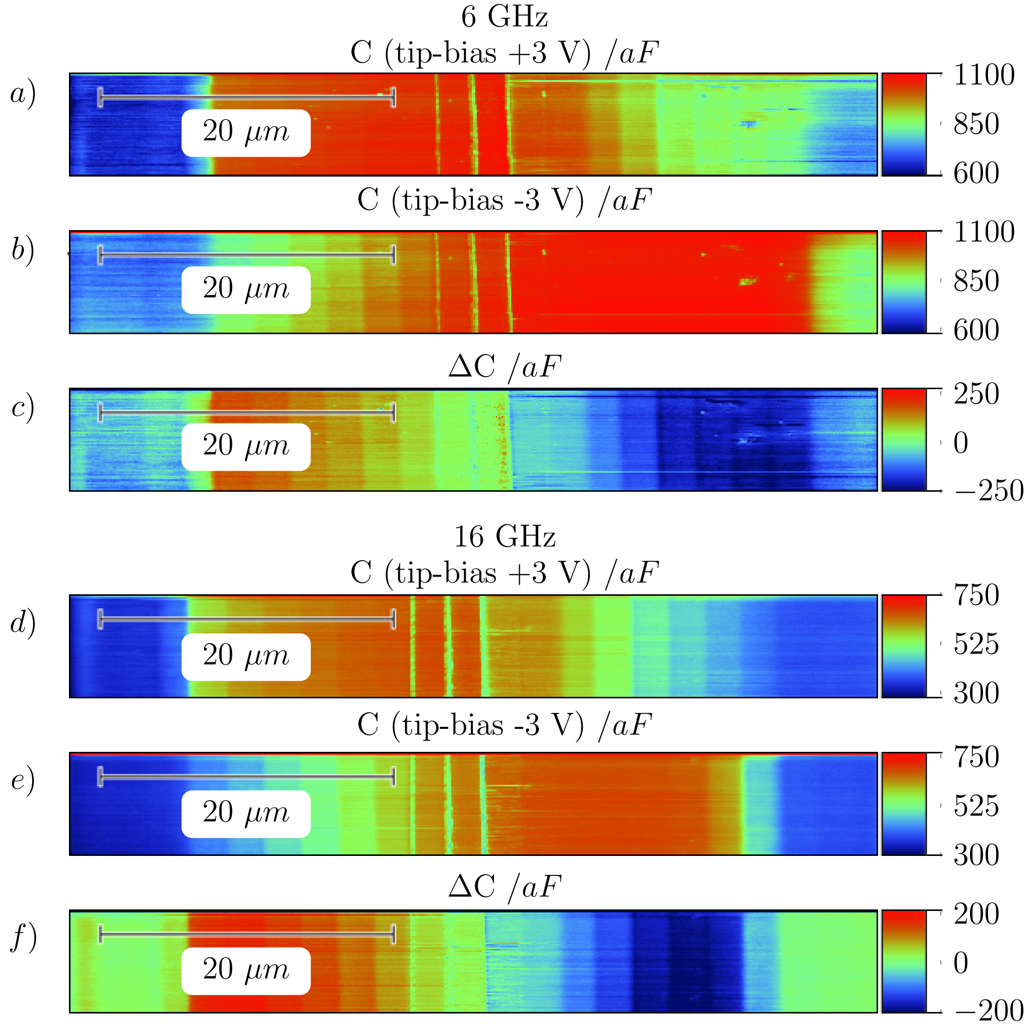

Figure 46: Capacitance measurement for p- (right side) and n-doped (left side) regions performed on Infineon calibration sample. The images (a) and (d) are acquired with +3 V DC bias and (b) and (e) with -3 V DC bias. ΔC in (c) and (f) is calculated of (a) and (d) and (b) and (e). ΔC represents the slope of the C-V curves, positive values correspond to the positive slope of n-type C-V curves and negative values to the negative slope of p-type C-V curves.

for low dopant densities in the data acquired at the lower frequency of 6 GHz in contrast to the 16 GHz data. In order to calculate ΔC, the data from fig. 46 (b) and (e) was subtracted from the data shown in fig. 46 (a) and (d). The resulting ΔC distribution with information on the dopant type is shown in

fig. 46 (c) and (f). The ΔC signal calculated from the data acquired at 6 GHz identifies the positive C-V slope for n-type dopants down to 4x10^{16} atoms cm^{-3} and a negative slope for p-type dopants over the whole density range. The 16 GHz ΔC data reveals a positive slope for n-type densities down to 1x10^{16} atoms cm^{-3} and a negative slope for p-type densities above 4x10^{16} atoms cm^{-3}.

5.3.3 Depletion Capacities

The ΔC method was proven to be an efficient tool to reveal the dopant type, however it shows a non-monotonic dependency on the dopant density. As the depletion capacities scale with dopant densities, the goal is to combine the respective depletion capacitance data for both p- and n-type silicon to one dataset. Therefore, it is necessary to distinguish between p- and n-type sili-

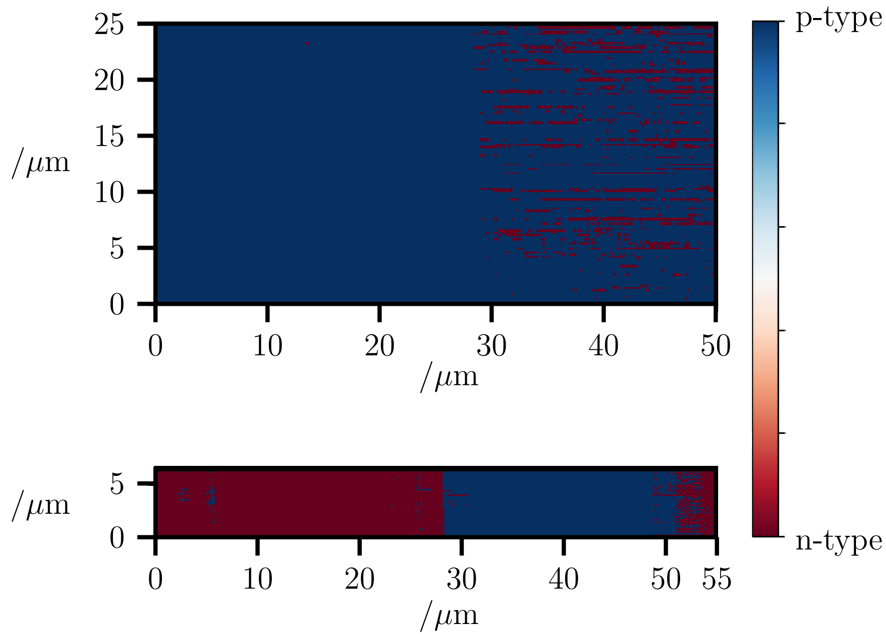

Figure 47: The information of a positive or negative slope extracted from ΔC data to reveal dopant type information. In the upper part the ΔC data obtained with 4 GHz at the p-doped epitaxial layer of the IMEC T8 sample shown in fig. 44 was used. In the lower part, the ΔC data obtained with 16 GHz at the p-and n-doped calibration sample shown in fig. 46 is the basis for the dopant type distinction.

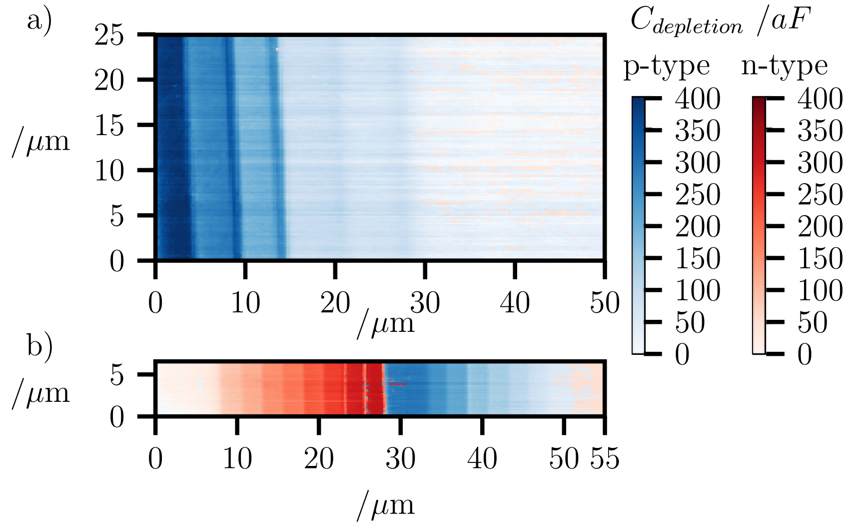

Figure 48: SMM depletion capacitance images, combining p- and -n-type depletion capacitance data. For p-type, the capacitance data obtained with a positive tip bias is plotted. For n-type, the capacitance data obtained with a negative tip bias is plotted.

con. This information can be extracted from the ΔC data as shown in fig. 47. This dopant type recognition enables the combination of the two datasets recorded with a positive and a negative bias to one single image showing the depletion capacities for both dopant types. For the p-type Si, the depletion capacitance data is the data acquired with a positive tip bias while for the n-type Si, the depletion data is selected from the data acquired with a negative tip bias. Figure 48 depicts the combined depletion capacitance data for both dopant types. In order to differentiate between p- and n-type, different color sets were chosen. In fig. 48 (a), the p-type semiconductor stripes are clearly visible for the epitaxial sample at 4 GHz. Furthermore, the depletion capacitance scales with the dopant density over the entire measurement range. Figure 48 (b) depicts the depletion capacitance image calculated of the calibration sample data acquired at 16 GHz. The higher measurement frequency leads to a decreased ΔC at low dopant densities. Nonetheless, the p/n distinction works fine, due to the good SNR. The n-type semiconductor was fully identified over the whole range of densities. The p-type silicon, however, was wrongly classified as n-type at concentrations of $4x10^{15}$ atoms cm^{-3} and below.

Since small capacities in the range of a few aF are difficult to measure, it is not predictable which dopant type will be wrongly classified. Small stray effects can lead to this wrong classification.
The dopant densities scale with the depletion capacities over the whole range of investigated densities for both dopant types. The good SNR at higher measurement frequencies makes up for the benefits the lower measurement frequencies in terms of the accumulation capacitance reduction. Consequently, depletion capacitance SMM data acquired at high frequencies provides a reliable solution for dopant type determination. The presented method enables the distinction of the dopant type and the relation between the doping concentrations valid from at least 4x10^{16} atoms cm^{-3} to 1x10^{20} atoms cm^{-3}, proving to be an ideal tool to characterize dopant types as well as density relations in electronic devices.

5.3.4 Dopant Density Calculation

The SCR capacitance in depletion state is independent on small variations in surface potential and can therefore be used to calculate the dopant densities. The measured depletion capacitance C_D is a series capacitance of the oxide capacitance C_{ox} and the capacitance of the SCR C_{SCR}. The SCR capacitance can be calculated by

$$C_{SCR} = \frac{C_D C_{ox}}{C_{ox} - C_D}. \tag{39}$$

While the depletion capacitance is extracted from SMM measurement data, the oxide capacitance can be estimated as the maximum measured capacitance from both positively and negatively biased data. Here, it is important to remove outliers and neglect abnormally high capacitance values which can be measured, e.g. on a metallic surface. This estimated C_{ox} can then be used to calculate C_{SCR}. The relation between the effective tip area A and the oxide thickness d_{ox} is given by

$$C_{ox} = \frac{\epsilon_i A}{d_{ox}}. \tag{40}$$

While native oxides typically take very long to exceed 1 nm thickness, the colloidal silica slurry used for the SMM polish contains an oxidizing agent increasing the oxide thickness [91, 92]. Assuming an oxide thickness of 2 nm, which is a typical native oxide thickness after SMM sample preparation, the effective tip area can be calculated. The SCR width W_d can then be calculated from the data by

$$W_d = \frac{A\epsilon_i}{C_{SCR}}. \tag{41}$$

In depletion state the SCR is $W_d = W_{d\ max}$. The relation between dopant density and SCR width is thus given by eq. (16). Equation (16) needs to be solved for the dopant density N_A [93].

$$\begin{aligned} W_{d\ max} &= \sqrt{\frac{4\epsilon_{Si}kTln(N_{D/A}/n_i)}{q^2 N_{D/A}}} \\ W_{d\ max}^2 &= \frac{4\epsilon_{Si}kTln(N_{D/A}/n_i)}{q^2 N_{D/A}} \\ \frac{ln(\frac{n_i}{N_{D/A}})}{N_{D/A}} &= -\frac{q^2 W_{d\ max}^2}{4\epsilon_{Si}kT} \\ \frac{n_i}{N_{D/A}} ln(\frac{n_i}{N_{D/A}}) &= -n_i \frac{q^2 W_{d\ max}^2}{4\epsilon_{Si}kT} \end{aligned} \tag{42}$$

This equation can now be solved numerically by using the Lambert W function. The solution can be calculated by substituting x for $n_i/N_{D/A}$, and α for $-n_i q^2 W_{d\ max}^2/(4\epsilon_{Si}kT)$ and using the numerically pre-calculated solutions for $W(\alpha)$.

$$\begin{aligned} xln(x) &= \alpha \\ x &= e^{W(\alpha)} \\ N_{D/A} &= \frac{n_i}{x} \end{aligned} \tag{43}$$

Based on the derived equations, the dopant densities in fig. 49 were calculated from the depletion capacities (fig. 48). The images provide an overview

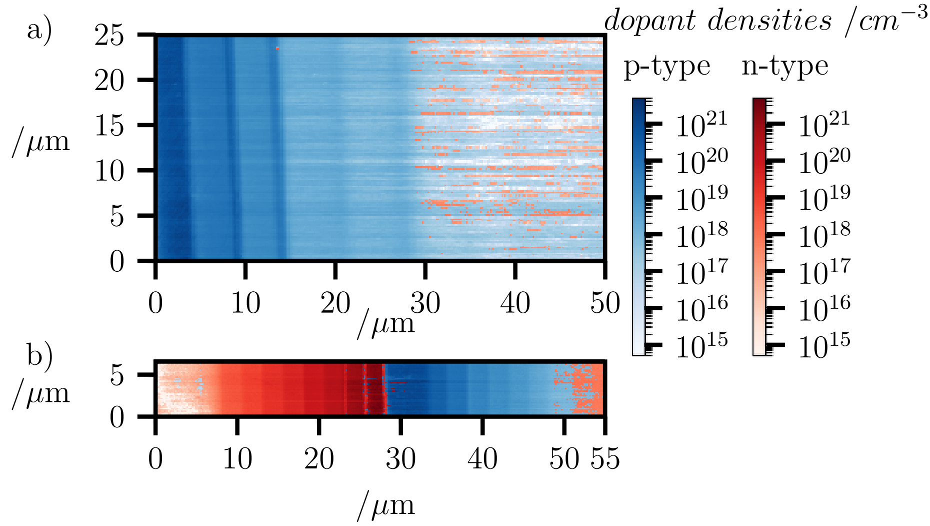

Figure 49: Dopant densities calculated from the depletion capacities measured with SMM, at the epitaxial (a) and calibration sample (b). The calculation is based on an estimated oxide thickness of 2 nm and the lowest measured capacitance assumed to be approximately the offset capacitance.

of dopant type and density of the scanned part of the investigated sample. The calculated dopant densities are about one order of magnitude too high when compared to the expected values from SIMS. For comparison of the calculated dopant densities with the datasheet values, a profile was extracted from the data obtained on the epitaxial sample. An overlay of the extracted profile and the reprinted datasheet values is plotted in fig. 50. The SNR is good for the high dopant densities, because the larger capacities at higher densities are less susceptible to stray capacities then the small capacities of low dopant densities. Hence, the SNR gets worse for the lower dopant densities where the measurement of smaller capacities provide more difficulties. The calculated dopant densities deviate by a factor of 4 to 20 compared to the expected values. There can be several reasons for this deviation. The performed capacitance calibration is not perfectly accurate. It strongly depends on the accuracy of the EFM capacitance used for the calibration and the accuracy of the corresponding fit of the 2-port error parameters, which is one possible influence on the accuracy of the calculated densities. The oxide thickness is assumed to be 2 nm, but it varies from sample to sample due to sample preparation and storing

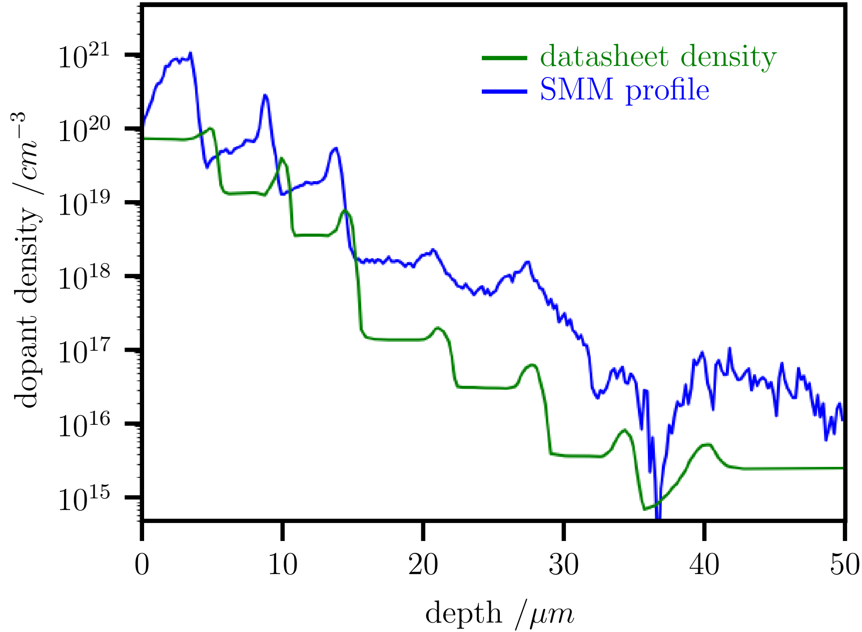

Figure 50: SMM dopant profile of the epitaxial layer sample extrcated from fig. 49.a. The datasheet densities are reprinted for comparison.

conditions. Furthermore, the accuracy of the capacitance calibration decreases for smaller capacities. Consequently, the offset capacitance accuracy has limitations. Those offset capacitance inaccuracies can explain the deviation for low dopant densities, but not for high densities.

5.3.5 Parameter Optimization

To optimize the parameters and achieve a more accurate calculation of dopant densities from the obtained data, different parameter fits, using a fitting procedure based on the equations in section 5.3.4, were performed. A precondition for the fit is that the dopant density of at least one region on the investigated sample is known. At first, the optimization of the offset capacitance was considered. The offset capacitance was chosen as a free fitting parameter and a fit was performed to match the calculated dopant densities to the datasheet values. The fit was repeated for each of the epitaxial layers. Figure 51 shows

the resulting profiles. As the offset dopant density is subtracted from the measured capacitance to achieve the best fit, it can result in very small and even negative capacitance values for dopant densities lower than the fitted density. Hence, the resulting calculated dopant density values are valid only for values above the fitted dopant density value. The averaged capacitance of the corresponding epitaxial layer was used for the fit. The extracted single line profile shows, that small deviations below the average capacitance of the fitted layer cause strong variations in calculated density, confirming the limited validity. As can be seen in fig. 51, the optimization of the offset capacitance agrees well with expected values for the fits with the lower dopant densities of 1.4x10^{17} atoms cm^{-3} and 3.2x10^{16} atoms cm^{-3}. All deviations in the valid range are better than a factor of 6 for the fit to 1.4x10^{17} atoms cm^{-3} and better than a factor of 9 for the fit to 3.2x10^{16} atoms cm^{-3}. For the fit to 3.8x10^{15} atoms cm^{-3}, the accuracy decreases with the maximum deviation of about a factor

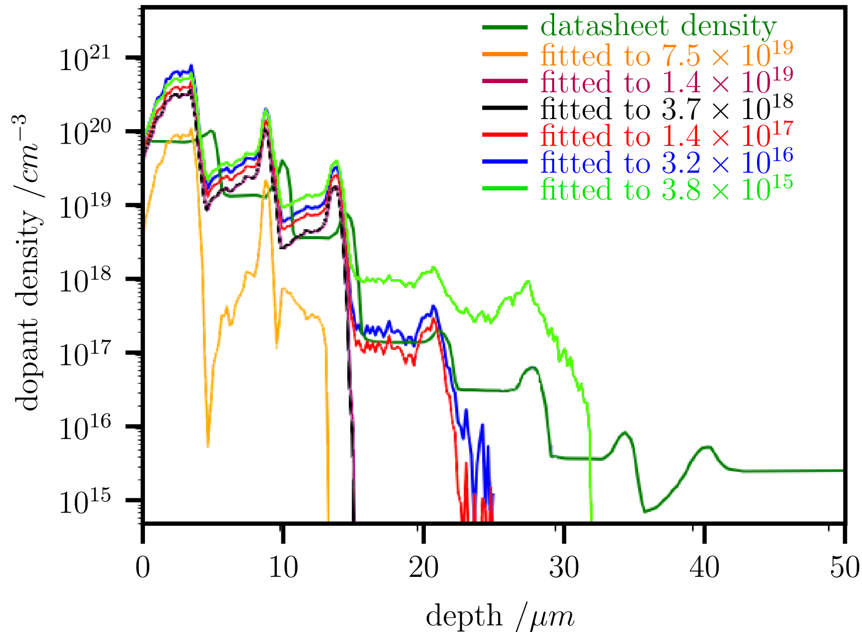

Figure 51: SMM dopant density profiles of the epitaxial layer sample. The offset capacitance was fitted to match the dopant density calculated from the depletion capacitance with the datasheet dopant density.

of 10 in the extracted line profile. In contrast to the relatively homogeneous level obtained at the higher dopant densities, there is a steep gradient in the obtained capacitance at 3.8×10^{15} atoms cm^{-3}, the average level had to be used for the fit. This gradient shows the inaccuracy of the measurement at low dopant density due to the low capacitance, responsible for the stronger deviations of this fit. However, this is an improvement in contrast to the unfitted parameters.

A second parameter for optimization is the oxide thickness, which can vary from sample to sample based on the chemical treatment during the polishing step, the time interval between polishing and measurement and the storage conditions. Hence, scans are typically performed directly after polishing to reduce quality degradation of the cross-section and enhance the signal. This is not true for the cross-sectioned standard sample used here, which is only polished on a yearly basis, since edge rounding increases after each polishing

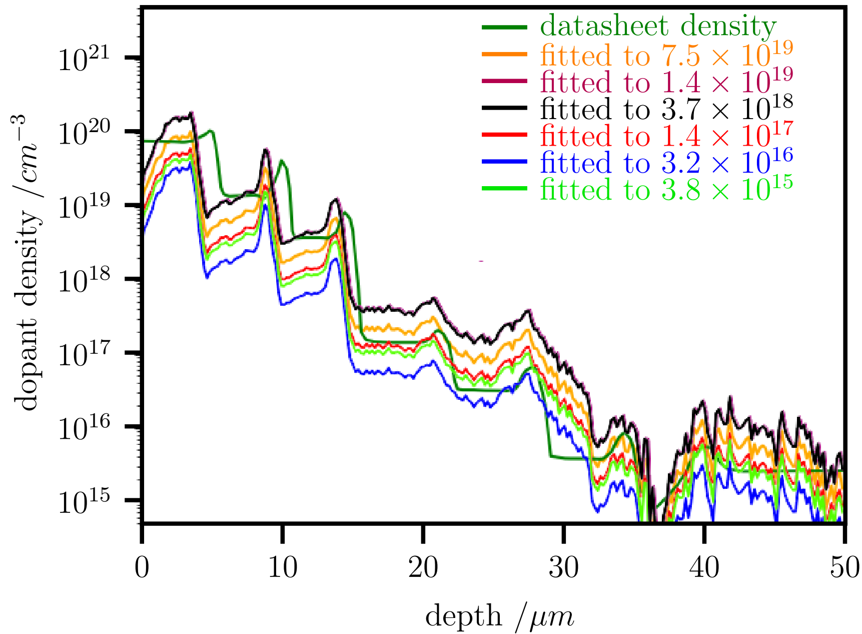

Figure 52: SMM dopant density profiles of the epitaxial layer sample. The oxide thickness was fitted to match the dopant density calculated from the depletion capacitance with the datasheet dopant density.

step. Similar to the offset capacitance fit, the oxide thickness fit was performed for all available densities. The comparison of fit results and expected densities is shown in fig. 52. In contrast to the fitted offset capacitance, fitting the oxide thickness just shifts the level of the profile to align with the fitted dopant density without influencing the relation between the densities. Consequently, the profile is valid for all dopant densities. All fits achieved an accuracy better than a factor of 0.1 to 10. The data obtained on the epitaxial layer with a boron density of 3.8x10^{15} atoms cm^{-3} shows a strong decrease of the calculated density within the layer and could not be measured reliably. Nevertheless, the fit of oxide thickness was used to enhance accuracy by still maintaining the validity over the entire density range. The value of the fitted oxide thickness varies from 4 nm to nearly 10 nm. 4 nm oxide thickness resulting from the fits to 1.4x10^{19} atoms cm^{-3} and 3.7x10^{18} atoms cm^{-3} is slightly above the upper end of the expected range after the treatment with chemical polish and the extended storage time in an uncontrolled atmosphere. The even higher oxide fit results, however, are clearly above the oxide thickness possible by oxidation at room temperature and the expected anodic oxidation through repeated measurements [91, 92, 94, 95]. Nevertheless, the accuracy in terms of dopant densities was improved, even if some fitted oxide thickness values are not in the expected range.

Therefore, a fit was performed to match both parameters, the oxide thickness and the offset capacitance. As there are two free fitting parameters, C_{Offset} and d_{ox}, two known dopant densities are required for this fit. The fit was performed to match the dopant densities at 1.4x10^{19} atoms cm^{-3} and 3.2x10^{16} atoms cm^{-3}. The resulting extracted profile is shown in fig. 53. The fit delivered a more plausible oxide thickness of 3.36 nm. The deviations between the calculated and the datasheet values are quite small. To reduce the influence of noise on the extracted profile, the profile was averaged over the image to reduce the noise. The resulting profile depicted in fig. 54 and the absolute values listed in table 5 show even less deviations from the datasheet dopant densities.

The densities between 3.2x10^{16} atoms cm^{-3} and 1.4x10^{19} atoms cm^{-3} show an accuracy better than ±30 %. The calculated density at 7.5x10^{19} atoms cm^{-3} is off by a factor of 3. While this could be partly due to the accuracy limitations in the calibration, another reason could be that the oxide capacitance assumed

for this calculation is slightly lower than the real oxide capacitance. This seems likely since the oxide capacitance was estimated from the accumulation capacitance, which also implies a measurement error. Deviations between assumed and real oxide capacitance have the strongest influence on the calculation of the highest dopant densities. Hence, this could explain part this error.

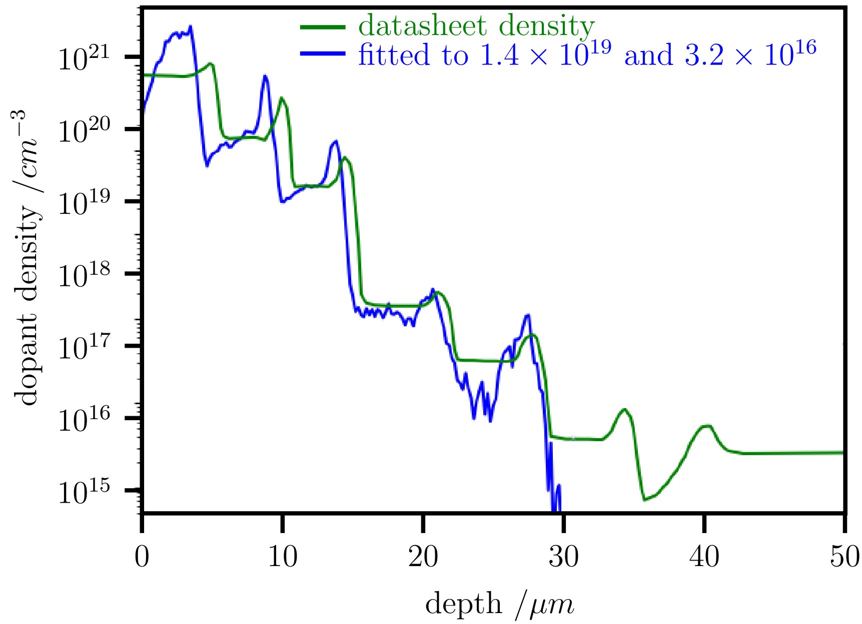

Figure 53: SMM dopant density profiles of the epitaxial layer sample. The oxide thickness and offset capacitance were fitted to match the dopant densities calculated from the depletion capacitance with the datasheet dopant densities.

Table 5: Datasheet dopant densities in comparison to the dopant densities calculated from capacitance data measured with SMM.

SIMS results (cm^{-3})	SMM results (cm^{-3})
3.2×10^{16}	4.1×10^{16}
1.4×10^{17}	1.5×10^{17}
3.7×10^{18}	3.1×10^{18}
1.4×10^{19}	1.5×10^{19}
7.5×10^{19}	2.0×10^{20}

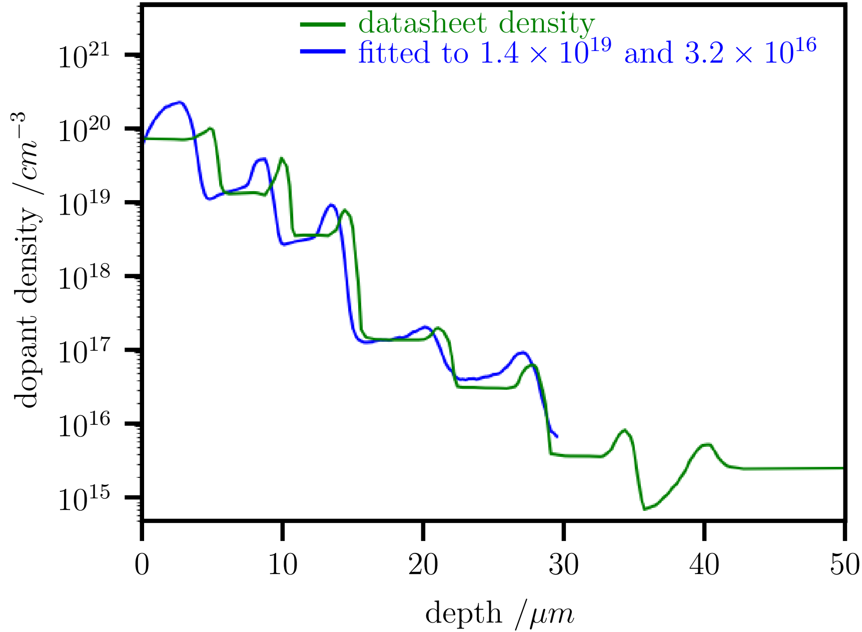

Figure 54: SMM dopant density profiles of the epitaxial layer sample. The oxide thickness and offset capacitance were fitted to match the dopant densities calculated from the depletion capacitance with the datasheet dopant densities. The profile was averaged over the whole image to reduce the noise.

Figure 55 shows the dopant density profile calculated and fitted from SMM data acquired on the calibration sample. The densities were fitted to $4x10^{16}$ atoms cm^{-3} and $1.2x10^{19}$ atoms cm^{-3} of the n-type dopant densities on the left side of the lateral dopant density profile plotted in fig. 55. The resulting dopant densities calculated from SMM data are compared with the SIMS and datasheet values in table 6.

The dopant densities are in good agreement with the SIMS as well as datasheet values within a deviation factor of 0.5 to 2. The exception is the highest p-type dopant density (marked red). While the deviation factor from datasheet value is 0.5, the value deviates by a factor of $5.6x10^{-2}$ from the SIMS result. This strong deviation from SIMS is partly due to the fact that the strong peak in the SIMS measurement reaches only into a few nm of depth and decreases by an order of magnitude afterwards. This depth is exceeded by the SCR in

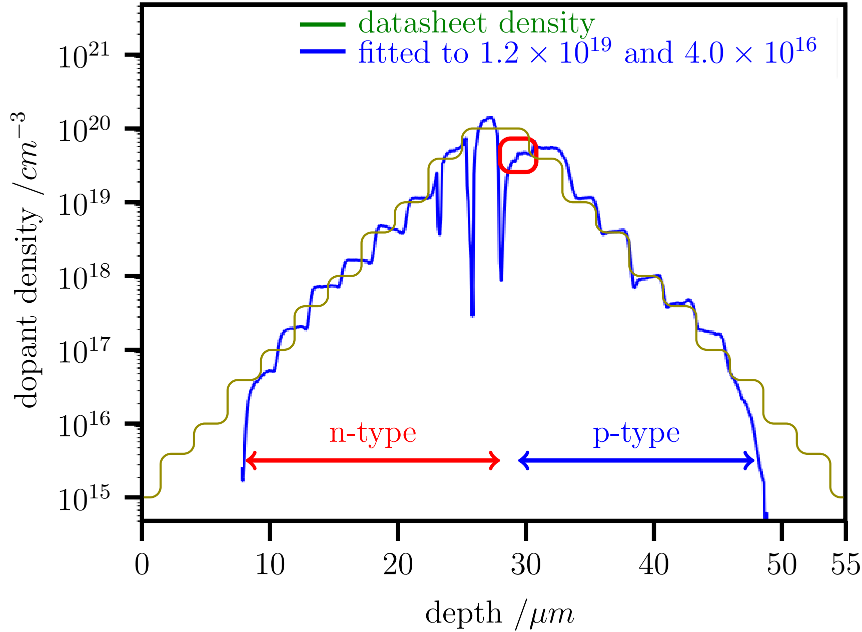

Figure 55: SMM dopant density profile obtained at the calibration sample. The oxide thickness and offset capacitance were fitted to match the dopant densities calculated from the depletion capacitance with the datasheet dopant densities. The profile was averaged over the whole image to reduce the noise. The largest deviation from datasheet values is indicated in red.

the SMM measurement. Thus the density within the probed region in SMM is closer to 10^{20} atoms cm^{-3} than 10^{21} atoms cm^{-3}. Nonetheless, the dopant density there is evidently higher than in the neighboring region, which is according to the datasheet doped with 4x10^{19} atoms cm^{-3}. Therefore, the density calculated from SMM data should be higher as well. To gain a deeper understanding of this abnormality, the data obtained in this area was analyzed in detail. The topography data at this position shows an average step height of 0.85 nm to the neighboring density levels, suggesting that a stronger oxidation in this area led to a lower measured capacitance. This is confirmed by the reduced accumulation capacitance found in the capacitance data obtained with negative tip bias. The oxide capacitance is reduced by 25 aF compared to the neighboring areas. Hence, the thicker oxide growth invalidates the measured

Table 6: Datasheet dopant densities are compared with the SIMS and SMM results. The fitted values are marked in green.

Dopant type	Intended dopant density (cm^{-3})	SIMS results (cm^{-3})	SMM results (cm^{-3})
n-type	4.0×10^{16}	4×10^{16}	4×10^{16}
n-type	1.0×10^{17}	1.0×10^{17}	2.0×10^{17}
n-type	4.0×10^{17}	4.0×10^{17}	7.6×10^{17}
n-type	1.0×10^{18}	1.1×10^{18}	1.8×10^{18}
n-type	4.0×10^{18}	5.0×10^{18}	4.8×10^{18}
n-type	1.0×10^{19}	1.2×10^{19}	1.2×10^{19}
n-type	4.0×10^{19}	5.5×10^{19}	5.5×10^{19}
n-type	1.0×10^{20}	1.5×10^{20}	1.3×10^{20}
p-type	1.0×10^{20}	9.0×10^{20}	5.0×10^{19}
p-type	4.0×10^{19}	8.0×10^{19}	6.0×10^{19}
p-type	1.0×10^{19}	1.4×10^{19}	1.2×10^{19}
p-type	4.0×10^{18}	5.0×10^{18}	4.4×10^{18}
p-type	1.0×10^{18}	1.2×10^{18}	1.0×10^{18}
p-type	4.0×10^{17}	3.5×10^{17}	4.6×10^{17}
p-type	1.0×10^{17}	1.0×10^{17}	1.9×10^{17}
p-type	4.0×10^{16}	4.0×10^{16}	3.3×10^{16}

capacities in this area. Consequently, for highly p-doped areas, the accumulation capacitance and topography data need to be checked to make sure the calculated dopant densities are valid.

The results show that the calculation of dopant densities from SMM data enables the simultaneous display of dopant types and densities in one image. The accuracy of this method is about one order of magnitude. The relation factor between the densities calculated from SMM data and the datasheet densities ranges from 0.1 to 20. The method can be improved by fitting calculation parameters to known densities. With one density known, the accuracy can be improved to below one order of magnitude. If the fitted parameter is the offset capacitance, all calculated densities below the fitted one are invalid and hence, must not be considered. For a fit performed with the oxide thickness as free fitting parameter, the entire measurement range stays valid. By fitting two parameters to densities, an improved accuracy factor ranging from 0.5 to

2 was achieved. Yet again, calculated densities below the lowest fitted density are invalid.

5.4 Industrial Applications

The standard samples introduced in previous chapters provide ideally suited objects to investigate the theoretical behavior of the SMM signals with reduced parasitic influences. For the calibration sample, there was only one implant per area on a lowly doped silicon substrate, while for the epitaxial sample there was no implant in the substrate, besides the epitaxial doping. Thus, those samples were ideal to develop a deep understanding of the basic influences in the absence of further parasitic effects. In industrial applications, there are many additional influences on the measurement data. Therefore, the developed methods are applied and tested on state-of-the-art electronic devices to test the methods' capability for semiconductor industry.

5.4.1 Dopant Profile

The first investigated sample is an ESD diode structure. Figure 56 shows the SIMS measurements obtained on the two different pads of the ESD diode. It was used to evaluate the SMM data. The SIMS data obtained below the big pad shows an n-p-n structure, the data below the small pad shows a p-n structure. A cross-section was prepared enabling access to the sample area of interest. An SMM calibrated capacitance scan was performed at ± 3 V DC bias. The obtained depletion capacities were combined to one image plotted in fig. 57. The center of the sample was scanned with a scan width of 70 μm to image structures below both pads at one time. The two trenches in the middle of fig. 57 separate the structure below the big pad on the left side of the image from the structure below the small pad on the right side of the image.
The n/p/n structure below the big pad is clearly visible in the SMM image. In contrast to the SIMS results, the n-type region below the contact seems more confined. At the highly doped n-type region on the upper end of the image, the depletion capacitance increases towards the edge, in agreement with the

SIMS measurements of the big pad. At the bottom of the image, the depletion capacitance increases towards the substrate. This increase matches the increasing phosphor density towards the substrate observed in the SIMS data. Based on the SIMS data of the big pad, the substrate phosphor density is lower than the density in the contact implant. In contrast, the SMM data shows, that the depletion capacitance measured at the substrate is higher than the capacitance at the contact implant. To find the reason for those deviation in SMM results, the minority carrier distribution needs to be taken into account. A comparison with the SIMS results shows, that the boron density is higher towards the substrate, increasing the amount of minority carriers. An accumulation of minority carriers might to be the reason for the increased depletion capacitance. This effect coincides with a similar effect observed at the p/n junctions of vertical transistors, not shown here, where an increased depletion capacitance was observed in the SCR due to the higher amount of minority carriers.

The structure on the right side of the image, corresponding to the small pad, matches the SIMS results. In both SMM and SIMS data, the p-type signal increases towards the upper edge. The signal peak is observed a few nanometers before this edge. In the SIMS data, the peak is located 680 nm from the edge, which agrees well with the position in SMM of 690 nm from the edge.

To calculate the dopant densities from the measured depletion capacities, a

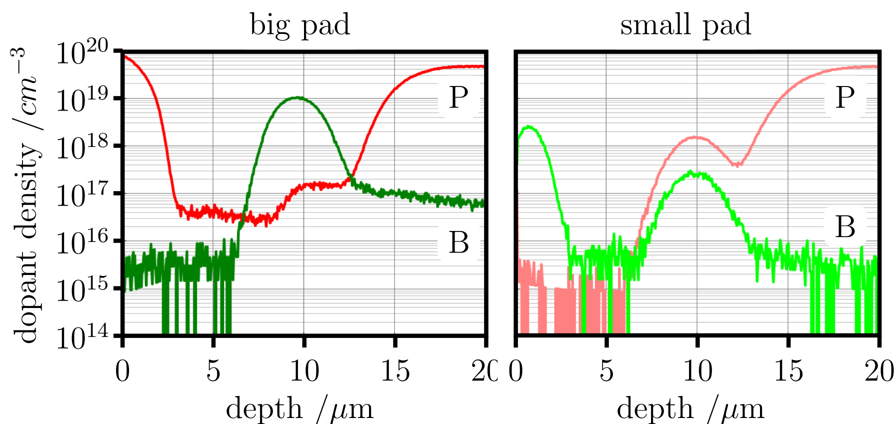

Figure 56: SIMS depth profiles revealing boron (green) and phosphor (red) concentrations obtained at the two different pads of an ESD diode structure.

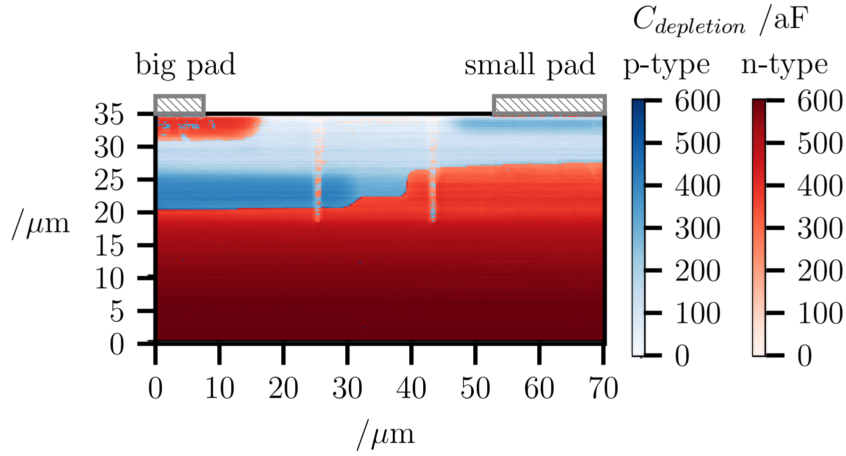

Figure 57: SMM depletion capacities showing dopant types and relations, obtained at +3 V resp. -3 V at an ESD diode struture. The pad areas are indicated above the plot.

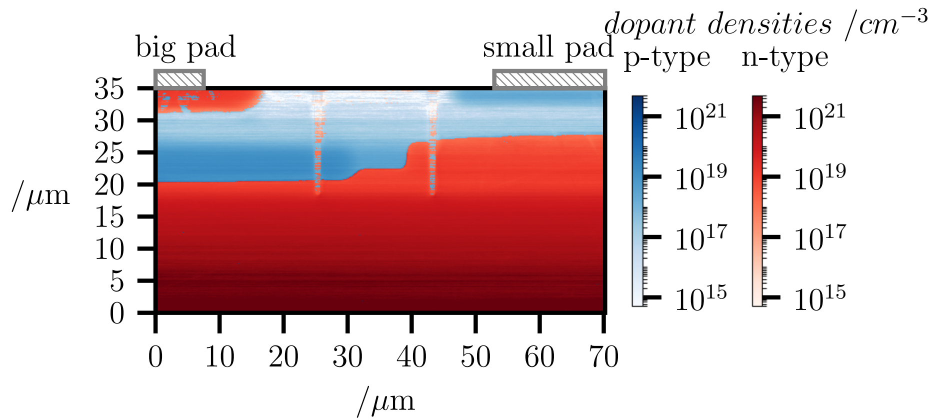

Figure 58: The calculated dopant densities obtained at the middle of an ESD diode structure were calculated fom the depletion capacitance data using an offset capacitance of 73.17 aF and an oxide thickness of 4.76nm.

two-parameter-fit was performed, optimizing values for the offset capacitance and the oxide thickness. The fit was performed to match the boron peak dopant density of 2.5x10^{18} atoms cm^{-3} and the lower boron density of 4.0x10^{16} atoms cm^{-3} below the small pad. The boron densities were chosen because no apparent underlying n-type doped region was detected by SIMS. The resulting dopant density distribution is shown in fig. 58. Comparing the results from SIMS and SMM, the dopant densities of the boron doped regions reveal

a good match at the peak density where the implant is $2.5x10^{18}$ atoms cm^{-3} and a lower boron density in the uniform region very noisy between 10^{16} atoms cm^{-3} and 10^{17} atoms cm^{-3}. The good agreement benefits from the fact that those densities were used for the fit. The first phosphor peak at the small pad is in the order of $1.5x10^{18}$ atoms cm^{-3} according to the SIMS results, while the density calculated from the SMM data is with $1.5x10^{19}$ atoms cm^{-3} one order of magnitude higher. Cause for this relatively large deviation is the overlayed boron peak at the very same scan position (see fig. 56), increasing the depletion capacitance used to calculate the dopant density. Similarly, the phosphor density in 20 μm distance from the surface towards the substrate should be $4.6x10^{19}$ atoms cm^{-3} referring to the SIMS data and is $1.5x10^{20}$ atoms cm^{-3} in the SMM data. The deviation factor of 3.26 is smaller than above, however the respective overlayed boron density in this region still contributes to the discrepancy. The phosphor density at the edge under the big pad is $7.2x10^{19}$ atoms cm^{-3} according to SIMS data, while SMM data gives a value of $1.5x10^{19}$ atoms cm^{-3}, i.e., the deviation factor is 0.21. The boron peak below the big pad should be at $1x10^{19}$ atoms cm^{-3} referring to the SIMS data. The density calculated from the SMM data is $1.8x10^{19}$ atoms cm^{-3}, deviating only by a factor of 1.8 from the SIMS data. This small deviation despite an increased overlayed phosphor density only marginally supports the assumption, that the minority carriers influence the measured depletion capacitance.
In summary, an overall good agreement between SMM and SIMS was achieved. The results prove the suitability of the method for industrial applications. Further investigation could improve the accuracy taking into account the additional aspect of increased minority carrier densities and their influence on the calculated dopant densities. This can be done by considering the minority carrier density in eq. (16) leading to a decreased SCR width. Consequently, the resulting densities will be lower when the dopant density is calculated from the SCR width. As SMM provides no opportunity to measure the minority carrier density, this solution could only be applied for samples with a known minority carrier density, e.g. from process simulation or SIMS measurements.

5.4.2 Trap Generated Charges

Trapping effects and their influence on device performance are critical for device reliability in semiconductor applications. Ongoing miniaturization in the semiconductor industry leads to an even higher sensitivity of device characteristics on trap-related effects such as unexpected charges or unstable potentials. Techniques to improve the understanding of trapping effects and trap distribution in electronic devices are therefore essential to enhance device performance and reliability. Various established methods investigate the trapping effects in semiconductors by analyzing the electrical properties on device level. For example, C-V curves, voltage pulse measurements, charge pumping techniques and deep-level transient spectroscopy (DLTS) can be used to characterize the influence of traps on the device performance in great detail [96–98]. Nonetheless, these methods investigate the impact of charge trapping on the final device characteristics and can only provide, in combination with a trap model, a rough estimate of the location of traps within the device. Hence, a direct and reliable method is needed to spatially resolve trapping effects within electronic devices. SMM is a powerful tool to characterize charge carrier distributions in semiconductor devices. It is ideally suited to spatially probe electrical properties in semiconductors, but is not directly sensitive to oxide or interface trap states. As traps induce a change in charge distribution, e.g. in the local capacitance, the trapping effect can be visualized by observing the accumulated charge carriers at the Si-side of the Si/SiO_2 interface in case of interface-near oxide traps.

In contrast to typical SMM applications, this chapter introduces a SMM based method for the localization of oxide traps. The results of are published in ref. [99]. The investigated sample is a Si diode structure, showing an electrically abnormal leakage at the edge. The leakage indicates a conductive path at the Si/SiO_2 interface. Trapping effects in the oxide could be considered as a possible root cause, positively charged oxide or interface traps accumulate electrons, which form the leakage path [100, 101]. A cross-section of the sample was prepared to access the region of interest. The conventional approach for charge carrier detection was to measure the $d\underline{S}_{11}/dV$ signal at the sample cross-section. Figure 59 shows the spatial distribution of the measured

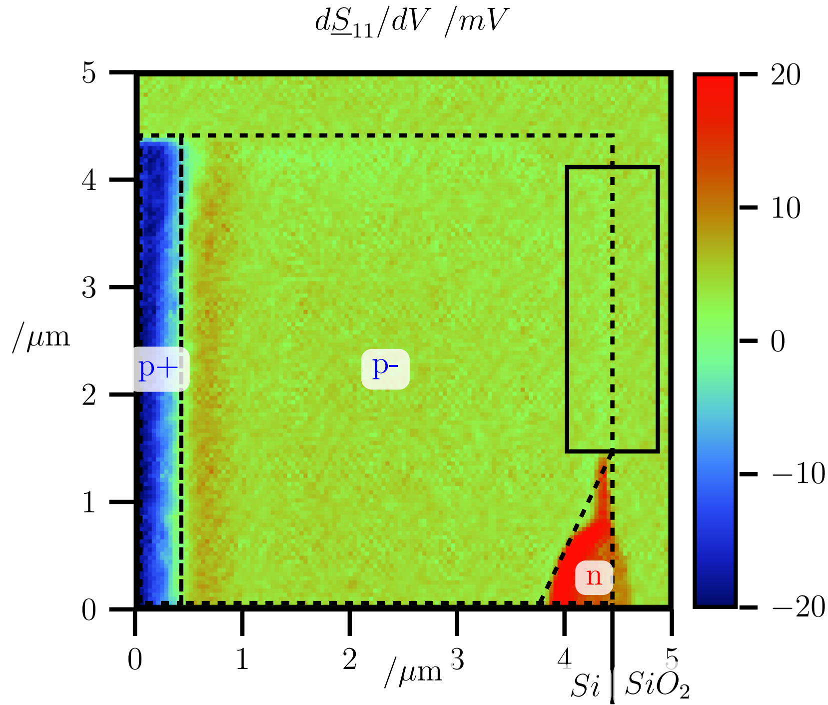

Figure 59: Real part of the $d\underline{S}_{11}/dV$ signal obtained at the edge structure of the investigated diode. The p+doped substrate, p-doped epi and n-type contact implant are highlighted with dashed lines. The solid rectangle marks the Si/SiO_2 interface where the "trap channel" would have been suspected.

$d\underline{S}_{11}/dV$ signal in the active device region. The Si/SiO_2 interface located in the right part of the image does not show any abnormality, which would confirm the suspected electron channel concluded from electrical measurements. Therefore, the calibrated capacitance method was employed for further investigation. The SMM scan using the ΔC approach on the embedded cross-section of the diode structure was performed at 7 GHz, scanning each line twice, first with a tip bias of +3 V and second with a tip bias of -3 V. The capacitance data was then calculated from the acquired $\underline{S}_{11}$ signal, as shown in fig. 60 for the +3 V scan. A relatively sharp cantilever tip was used to obtain an improved resolution. As the area of the MOS capacitor is mainly defined by the tip diameter, the measured capacitance was relatively small. That led to a large influence of the typical drift in the reflected microwave. In the marked region in the upper right of fig. 60 the interface between p-doped Si and the

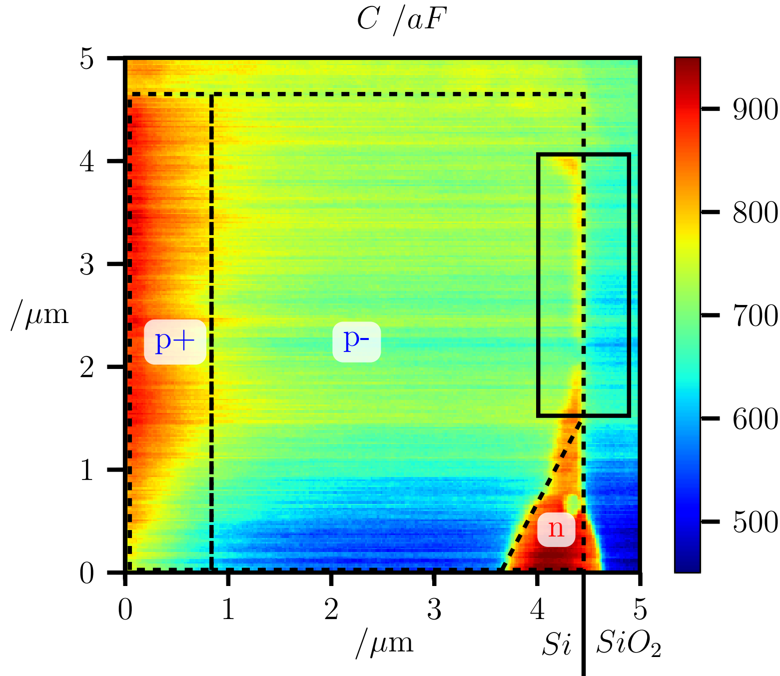

Figure 60: Capacitance data acquired at +3 V tip bias, calculated from a scan at the edge structure of the diode. The expected regions of differently doped Si are indicated by dashed lines. The solid rectangle marks the region of accumulated carriers.

SiO_2 can be seen. Although no accumulated charges in the intentionally lowly p-doped region would be expected for p-type, a small channel with a higher capacitance was found at the Si/SiO_2 interface. This channel indicates n-type carriers at the interface caused by process related interface traps. Still, the increased capacitance might also relate to a higher amount of p-type carriers at the Si/SiO_2 interface, which would increase the depletion capacitance. In fig. 61, the calculated ΔC of this SMM scan is shown, revealing the spatial distribution of the dopant type. The drift is eliminated by the subtraction of positive and negative data. The p+ region on the left side of the image is clearly distinguished as well as the n-doped region on the lower right. The p-doped region in the center could not clearly be separated from undoped regions, possibly due to a low doping concentration close to the detection limit of SMM. In the marked area on the upper right of the sample, similarly to the initial $\underline{S}_{11}$ data (see fig. 60), the expected accumulated charge appears at

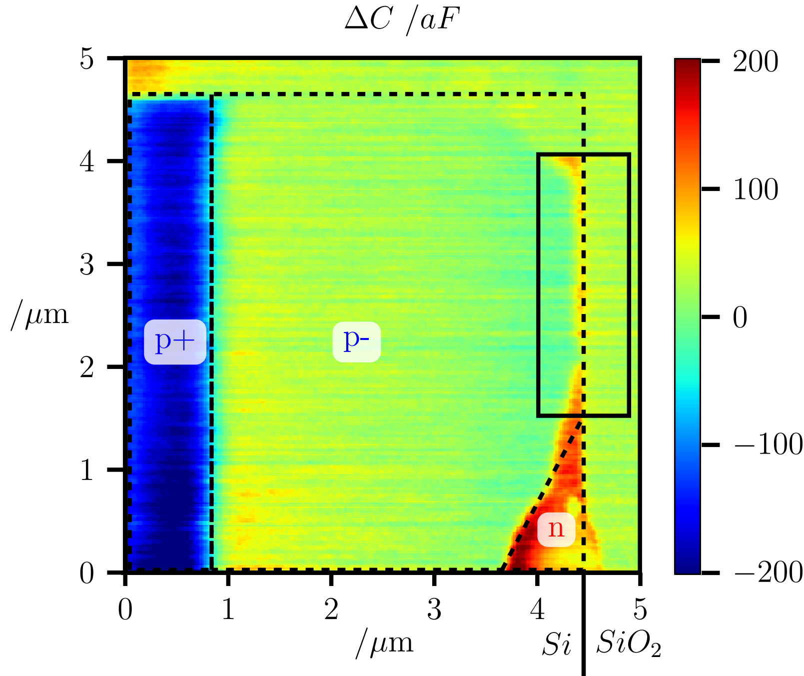

Figure 61: ΔC distribution calculated from a scan at the edge structure of the diode. Positive values indicate n-type carriers, negative ones to p-type. The channel of accumulated traps, indicated with the solid rectangle, is consequently n-type.

the interface between p-doped Si and SiO_2, which forms a conductive path. The ΔC data clearly proves this charge, accumulated on the Si-side of the Si/SiO_2 interface, to be n-type. Hence, the possibility of positive charges in the silicon can be ruled out. The detected negative charge on the Si side indicates positively charged oxide traps at or near the Si/SiO_2 interface. These possibly provide the driving force for the accumulation of electrons in the semiconductor. Since this method is based on the analysis of ΔC, it is also applicable to other SMM-related methods such as SMIM and SCM, where capacitive data is acquired. An established procedure for SMIM, e.g., enables the separation of the capacitive part of the signal from the resistive part [59]. For SCM, a similar procedure could in principle be applied to the resonance circuits raw data output. Hence, the differential capacitance method presented here provides a universal approach to study trapping effects in electric devices by different scanning techniques. By means of the example of a Si diode, SMM

has proven to be a valuable method to spatially resolve charge carriers accumulated by trapping effects. In conclusion, the SMM-based method provides a way to localize trapping effects at the Si/SiO_2 interface with a high spatial resolution. The differential capacitive method presented here provides a way to study trapping effects by SMM as well as related measurement systems.

6 Summary

Two dimensional charge carrier profiling of semiconductor devices is an application of essential importance for device development, process control and failure analysis. It allows to check the implant density distribution and compare it to the results of the process simulation to correct and optimize parameters. In failure analysis, deviations from intended dopant densities or even missing implants in electrically failing devices, e.g. due to shading in a lithography mask during frontend process, can be localized.
In this thesis a number of different carrier- and dopant profiling techniques were compared using a standard dopant calibration sample. The methods were evaluated based on their resolution, their ability to distinguish dopant types and their quantification ability. SIMS and SRP have a superior quantification ability, but lack in spatial resolution. Chemical decoration does not require complex equipment and was therefore often employed in the past, but has issues with reproducibility and offers no way to distinguish different densities. SEM offers a good resolution and signal scaling with dopant density, but cannot be used to distinguish dopant type or obtain quantitative results. The SCM signal scales with dopant density over a large range offering a good resolution. However, the non-monotonic signal hinders the direct quantification of dopant density possibly leading to misinterpretations. Nevertheless, it allows to differentiate p- and n-type if the type of at least one region on the sample is known. The signal scales with dopant density in SSRM, while allowing an even better spatial resolution than all other methods. The limited ability to distinguish dopant types and to measure absolute densities are disadvantages of SSRM. SSNOM provides the ability to measure absolute densities, but the range is limited to densities above $4 \text{x} 10^{18}$ atoms cm^{-3}. Even with a THz laser, the lower density limit is $4 \text{x} 10^{17}$ atoms cm^{-3}. Furthermore, the dopant type cannot be extracted. SMM and SMIM stand out by fulfilling all requirements. They offer spatial resolution and signals scale with dopant density, also inheriting the information to distinguish the dopant types. The possibility to obtain absolute capacitance and resistance using SMM enables the development of dopant quantification methods. These advantages make SMM an ideally suited method to study dopant characteristics in semicon-

ductor devices. Therefore, SMM is in the focus of this thesis.
Considering the cantilever parameters used in SMM to scan the sample surface, most SMM applications deal with a relatively smooth topography of a few nanometers and can thus be scanned with standard full metal probes. For samples with a more demanding topography, metal coated Si probes provide better wear stability. An FEM model of the probe-sample-interaction in SMM was developed to obtain the sensitivity of coated tips and to check the their suitability for SMM. Different probe parameters were varied in the model as well as in the experiment in collaboration with cantilever manufacturer NanoWorld. As a result, a set of optimized parameters was found for metal coated Si probes. The developed probes allow an SMM scan with an up to thirteen times higher sensitivity on dopant variations compared to the commercially available Si probes.
Since SMM combines the mechanical tip dimensions with the microwave excitation region the effective scan resolution is not directly given by the cantilever parameters. In order to investigate the effect of the microwave excitation region on the scan resolution, the highly confined 2DEG in a standard AlGaN/GaN heterostructure was scanned and the corresponding SMM signal was recorded. The deconvolution of the extracted profile with the expected shape of the 2DEG profile revealed the effective tip radius in SMM. A comparison between different cantilevers showed that the effective scan resolution is affected by the cantilever radius and shape as well as to a smaller extent by the microwave excitation region. For probes with a sharp tip, the effective tip radius was in agreement with the SEM image of the tip. The effective tip radius of unevenly shaped tips was found to differ from the SEM image. The effective tip shape could only be extracted from the profile. The introduced method was proven to enable the characterization of the effective tip radius and quality in SMM.
An established procedure allows the extraction of capacitance and resistance from calibrated $\underline{S}_{11}$ data recorded in SMM. A method to calculate resistivity and dopant density from the SMM resistance was presented. This method has been validated on two standard dopant profiling samples. It enables the quantitative 2D dopant profiling with an accuracy better than 60 % [79].
As the presented method does not reveal the dopant type and the capacitance calibration can be reproduced with a better repeatability than the resistance

calibration, a second method based on the capacitive signal was introduced. SMM C-V spectroscopy was performed to show, that the difference between accumulation and depletion capacitance, ΔC, can be used for dopant type distinction down to 4x10^{16} atoms cm^{-3}. Frequencies above 16 GHz were demonstrated to improve distinguishability between n- and p-type doped regions down to 10^{16} atoms cm^{-3}, based on a better SNR. The accumulation capacitance was shown to decrease for a low dopant density level, while the rate of the decrease was found to depend on measurement frequency. This phenomenon could be attributed to a frequency dependent effect known from high resistive substrates, where it occurs already at lower frequencies. It is related to the reduced charge carrier mobility at low dopant densities. Consequently, ΔC could not be used for a quantitative approach. To overcome this deficit, the depletion capacitance was shown to present a reliable tool to investigate the relations between dopant densities. The accuracy of dopant density calculation from depletion capacity densities is about one order of magnitude, deviating from the datasheet densities by a factor between 0.1 and 20. The accuracy could be improved by fitting unknown parameters, which vary slightly between measurements. It was improved to better than one order of magnitude deviation by using the oxide thickness as a free fitting parameter and fitting the calculated densities to a known density. With two free parameters, oxide thickness and offset capacitance further improvement to a deviation between 0.5 and 2 was achieved. Calculated densities below the lowest fitted density are not valid due to the subtraction of the fitted offset capacitance and were therefore neglected. In conclusion, it was demonstrated that the calculation of dopant densities from SMM data is a powerful tool to display dopant types and densities in one single image with all data obtained in one scan.
The transfer of the dopant density calculation to an industrial application was demonstrated on example of an ESD diode. The accuracy of the dopant densities calculated from SMM data when compared to the expected dopant profile was within a factor of 0.2 and 10. Further investigation on additional effects in complex semiconductor structures could help to further improve the accuracy.
A further industrial application demonstrated in this thesis is the spatially resolved imaging of charge carriers accumulated by trapping effects. On the example of a Si diode the extraction of ΔC from SMM data clearly identified

an electron channel caused by positively charged oxide traps.
Further improvements in calibration algorithm could be used to gain accuracy of the calibrated capacitance and accordingly make the necessity of parameter fits for this purpose obsolete. The presence of an SMM signal on the AlGaN/GaN heterostructure demonstrates that the methods introduced in this thesis are not limited to silicon, but can also be transferred to wide band-gap semiconductors. In summary, SMM was shown to provide reliable quantitative 2D dopant profiles with a high spatial resolution for failure analysis and product development.

Notations and Abbreviations

2DEG	2 dimensional electron gas
$\underline{a}_1$	output wave quantity
AFM	atomic force microscopy
$\underline{b}_1$	incident wave quantity
C_d	depletion capacitance
C_{ox}	oxide capacitance
C_{ts}	local tip sample capacitance
C_{SCR}	space charge region capacitance
C_{series}	series capacitance
C-V	capacitance-voltage
$d_{effective}$	shortest path to ground
DLTS	deep level transient spectroscopy
DPMM	dopant profiling measurement module
DUT	device under test
$e_{00},\ e_{01},\ e_{10},\ e_{11}$	error-2-port parameters
E_C	conduction band energy
E_F	fermi energy
E_g	midgap energy
E_V	valance band energy
EFM	electrostatic force microscopy
F_{DC}	EFM constant force term
F_{Ω}	EFM force term at 1st harmonic
$F_{2\Omega}$	EFM force term at 2nd harmonic
FDTD	finite difference time domain
FEM	finite-elements-method
FM	frequency modulation
FWHM	full width half maximum
G-V	conductance-voltage
HEB	head electronics box
HF	high frequency
k	Boltzmann constant
KPFM	kelvin probe force microscopy
MIS	metal-insulator-semiconductor

MoM	method of moments
MOS	metal-oxide-semiconductor
N_A	acceptor density
N_D	donor density
n_i	intrinsic carrier density
nano-FTIR	nano broadband infrared nearfield spectra
OSL	open short load
PEC	perfect electrical conductor
Pt	platinum
PtIr	platin-iridium
PtSi	Platin-silizide
q	elementary charge
r_{DUT}	reflection caused by DUT
R	resistance
R_s	surface resistance
R_{series}	series resistance
R_x	sheet resistance
RMN	Rocky Mountain Nanotechnology
Si	silicon
SiO_2	silicon-dioxide
SMM	scanning microwave microscopy
S-parameter	scattering parameter
$\underline{S}_{11}$	microwave backscattered from port 1 on port 1
$\underline{S}_{11,meas}$	measured backscattered microwave
SCR	space charge region
SEM	scanning electron microscopy
SIMS	secondary ion mass spectroscopy
SMIM	scanning microwave impedance microscopy
SMM	scanning microwave microscopy
SNR	signal to noise ratio
SPM	scanning probe microscopy
SRP	spreading resistance profiling
SSNOM	scattering-type scanning nearfield optical microscopy

STM	scanning tunneling microscopy
T	temperature in Kelvin
ToF-SIMS	time of flight SIMS
$V_{applied}$	applied voltage
V_{FB}	flatband voltage
V_{ts}	Voltage between tip and sample
V_{TS}	Voltage between tip and substrate
VNA	vector network analyzer
W_d	space charge region width
W_d, max	maximum space charge region width
$\underline{Y}_{DUT}$	admittance of the device under test
$\underline{Z}$	complex impedance
$\underline{Z}_0$	characteristic impedance
$\underline{z}_{dislocated}$	normalized impedance transformed by transmission line
$\underline{Z}_{DUT}$	impedance of the device under test
$\underline{z}_{DUT}$	normalized impedance of the device under test
$\underline{Z}_{in}$	input impedance
δ	skin-depth
Δ_C	capacitance difference
ϵ_i	insulator permittivity
ϵ_{Si}	silicon permittivity
θ	relaxation time
ρ	resistivity
ρ_{Si}	silicon resistivity
ϕ_{bm}	backside metal work function
ϕ_c	contact potential, similar to ϕ_{ms}
ϕ_i	built in potential
ϕ_m	metal work function
ϕ_{ms}	metal semiconductor work function difference
ϕ_s	surface potential
χ	electron affinity
ψ_{Bn}	n-Si fermi potential with respect to midgap
ψ_{Bp}	p-Si fermi potential with respect to midgap

List of Figures

1	Error two port.	11
2	Smithchart.	14
3	MOS-structure n-type flatband.	15
4	MOS-structure p-type flatband.	16
5	MOS-structure n-type accumulation.	17
6	MOS-structure p-type accumumlation.	17
7	MOS-structure n-type depletion.	18
8	MOS-structure p-type depletion.	19
9	Voltages and potentials in a simple MOS-structure.	21
10	High frequency C-V characteristics for (a) n- and (b) p-type silicon.	22
11	High frequency (GHz-range) C-V characteristics for (a) n- and (b) p-type silicon concidering reduced accumulation capacitance.	24
12	AFM conatct mode schematics.	26
13	AFM tapping mode schematics.	28
14	Calibration sample with different n- and n-type dopant densities.	32
15	AFM SMM schematics.	34
16	High frequency (GHz-range) C-V characteristics for (a) n- and (c) p-type silicon considering reduced accumulation capacitance.	35
17	SMM dS11/dV measurement of calibration sample.	35
18	EFM and SMM approach curves fitted for capacitance calibration.	36
19	SMM reflection measurement of calibartion sample.	37
20	Components of the Keysight 5600 LS.	38
21	Vector network analyzer Keysight N5230C.	39
22	SEM image of calibration sample.	42
23	AFM SCM schematics.	43

24 SCM image of calibration sample. 45

25 SMIM dC/dV measurement of calibration sample. 46

26 SMIM capacitive measurement of calibartion sample. 47

27 AFM SSRM schematics. 48

28 SSRM measurement of calibartion sample. 49

29 AFM SSNOM schematics. 50

30 SSNOM image of the calibration sample. 51

31 THz SSNOM image of the calibration sample. 52

32 Nano-FTIR at the calibration sample. 53

33 Cross-section of a diode prepared for SMM. 57

34 FEM Model of the AFM SMM probe. 61

35 FEM model with the tip-sample interface in more detail. 61

36 SMM image of 2DEG at the AlGaN/GaN interface. 66

37 SMM and literature depth profile of electron densities in 2DEG. 67

38 SMM 2DEG profile with a 25Pt300A cantilever. 68

39 SMM 2DEG profile with a PtSi-FM cantilever. 69

40 SMM data of the calibration sample sample. 72

41 SMM data of the IMEC n-type Si dopant sample. 75

42 IMEC-T8 datasheet densities. 78

43 C-V characteristics recorded on p-type silicon. 79

44 Capacities at IMEC T8 sample at 4GHz. 81

45 Capacities at IMEC T8 sample at 19 GHz. 82

46 Capacities at calibration sample. 84

47 Dopant type distinction extracted fom ΔC. 85

48 SMM depletion capacitance images. 86

49 Dopant densities of epitaxial and calibration sample. 89

50 SMM dopant profile of epitaxial sample. 90
51 SMM dopant density profiles with fitted offset capacities. 91
52 SMM dopant density profiles with fitted oxide thickness. 92
53 SMM dopant density profiles with fitted oxide thickness and offset capacitance. 94
54 SMM dopant density profile with fitted oxide thickness and offset capacitance averaged over all image lines. 95
55 SMM dopant density profile of the calibration sample with fitted oxide thickness and offset capacitance averaged over all image lines. 96
56 SIMS results obtained at an ESD diode structure 99
57 SMM depletion capacitance image of an ESD diode structure. . 100
58 SMM image of an ESD diode structure revealing the dopant densities. 100
59 Conventional SMM image of the silicon/oxide interface. 103
60 SMM capacitance image at +3 V of the silicon/oxide interface. . 104
61 SMM capacitance image of the silicon/oxide interface. 105

List of Tables

1 Dopant densities and types of the substrate and the 20 differently doped fields in area A. The p-type is boron doped, the n-type phosphor. The intended dopant densities and the results achieved with SIMS measurements in area A are shown. 31

2 Dopant profiling capabilities of the discussed methods. 53

3 Data sheet values of the two NanoWorld cantilevers PtSi-FM and PtSi-Cont and the parameters of the SMM probe modeled in finite elements method (FEM). 59

4 The upper table shows the simulated sensitivity on a small capacitive change, investigated by varying the oxide thickness from 20 nm to 40 nm. The lower table shows the sensitivity monitored through the maximum signal difference between highest and lowest signal at different dopant densities on the calibration sample at first measurement with a new tip. 63

5 Datasheet dopant densities in comparison to the dopant densities calculated from capacitance data measured with SMM. . . . 94

6 Datasheet dopant densities are compared with the SIMS and SMM results. The fitted values are marked in green. 97

List of Publications

Authered Publications

S Hommel, N Killat, A Altes, T Schweinboeck, D Schmitt-Landsiedel, M Silvestri, and O Haeberlen, *Scanning microwave microscopy for electronic device analysis on nanometre scale*, Microelectronics Reliability 64, 310-312 (2016)

S Hommel, N Killat, A Altes, T Schweinboeck, and F Kreupl, *Determination of doping type by calibrated capacitance scanning microwave microscopy*, Microelectronics Reliability 76, 218-221 (2017)

S Hommel, N Killat, T Schweinboeck, A Altes, and F Kreupl, *Resolving Trap-caused Charges by Scanning Microwave Microscopy*, 2018 IEEE 25th International Symposium on the Physical and Failure Analysis of Integrated Circuits (IPFA), 1-3 (2018)

Co-authered Publications

T Schweinboeck and S Hommel, *Quantitative scanning microwave microscopy: A calibration flow*, Microelectronics Reliability 54, 2070-2074 (2014)

E Brinciotti, G Gramse, S Hommel, T Schweinboeck, A Altes, M Fenner, J Smoliner, M Kasper, G Badino, S Tuca, and F Mienberger, *Probing resistivity and doping concentration of semiconductors at the nanoscale using scanning microwave microscopy*, Nanoscale 7, 14715-14722 (2015)

E Brinciotti, G Campagnaro, G Badino, M Kasper, G Gramse, S Tuca, J Smoliner, T Schweinboeck, S Hommel, and F Mienberger, *Frequency analysis of dopant profiling and capacitance spectroscopy using Scanning Microwave Microscopy*, IEEE Transactions on Nanotechnology 16, 75-82 (2017)

C Maissen, S Mastel, J Hesler, S Hommel, T Schweinboeck, I Amenabar, and R Hillenbrand, *Synthetic optical holography for phase resolved Terahertz*

nano-imaging at sub-50 nm resolution, 6th EOS Topical Meeting on Terahertz Science and Technology (TST 2018), (2018)

References

[1] S Morita, *Roadmap of scanning probe microscopy.* Springer Science & Business Media, 2006.

[2] GE Moore, *Cramming more components onto integrated circuits*, Electronics **38**, 114–117 (1965).

[3] D Hisamoto, WC Lee, J Kedzierski, H Takeuchi, K Asano, C Kuo, E Anderson, TJ King, J Bokor, and C Hu, *FinFET-a self-aligned double-gate MOSFET scalable to 20 nm*, IEEE Transactions on Electron Devices **47**, 2320–2325 (2000).

[4] Xuejue Huang, Wen-Chin Lee, Charles Kuo, Digh Hisamoto, Leland Chang, Jakub Kedzierski, Erik Anderson, Hideki Takeuchi, Yang-Kyu Choi, Kazuya Asano, *et al.*, *Sub 50-nm finfet: Pmos*, in *International Electron Devices Meeting*, pp. 67–70, Citeseer. 1999.

[5] B Yu, L Chang, S Ahmed, H Wang, S Bell, CY Yang, C Tabery, C Ho, Q Xiang, TJ King, *et al.*, *FinFET scaling to 10nm gate length*, in *International Electron Devices Meeting*, pp. 251–254, IEEE; 1998. 2002.

[6] GK Celler and S Cristoloveanu, *Frontiers of silicon-on-insulator*, Journal of Applied Physics **93**, 4955–4978 (2003).

[7] I Bertrand, V Pathirana, E Imbernon, F Udrea, M Bafleur, R Ng, H Granier, B Rousset, and JM Dilhac, *New lateral DMOS and IGBT structures realized on a partial SOI substrate based on LEGO process*, in *Bipolar/BiCMOS Circuits and Technology Meeting, 2005. Proceedings of the*, pp. 74–77, IEEE. 2005.

[8] D Widmann, H Mader, and H Friedrich, *Technologie hochintegrierter Schaltungen*, vol. 19. Springer-Verlag, 2013.

[9] J Rabkowski, D Peftitsis, and HP Nee, *Silicon carbide power transistors: A new era in power electronics is initiated*, IEEE Industrial Electronics Magazine **6**, 17–26 (2012).

[10] Y Uemoto, M Hikita, H Ueno, H Matsuo, H Ishida, M Yanagihara, T Ueda, T Tanaka, and D Ueda, *Gate injection transistor (GIT)-A normally-off AlGaN/GaN power transistor using conductivity modulation*, IEEE Transactions on Electron Devices **54**, 3393–3399 (2007).

[11] M Kanamura, T Ohki, T Kikkawa, K Imanishi, T Imada, A Yamada, and N Hara, *Enhancement-mode GaN MIS-HEMTs with n-GaN/i-AlN/n-GaN triple cap layer and high-k gate dielectrics*, IEEE Electron Device Letters **31**, 189–191 (2010).

[12] SC Binari, PB Klein, and TE Kazior, *Trapping effects in GaN and SiC microwave FETs*, Proceedings of the IEEE **90**, 1048–1058 (2002).

[13] E Zinner, *Depth profiling by secondary ion mass spectrometry*, Scanning **3**, 57–78 (1980).

[14] H Cachet, M Froment, E Souteyrand, and C Dennig, *Selective metal deposition on silicon substrates*, Journal of The Electrochemical Society **139**, 2920–2925 (1992).

[15] JR Matey, *Scanning capacitance microscope*, 1984. US Patent 4,481,616.

[16] F Strauß, *Grundkurs Hochfrequenztechnik*. Springer, 2016.

[17] G Zimmer, ed., *Hochfrequenztechnik*. Springer, Berlin, 2000.

[18] Friedrich-Wilhelm Gundlach, *Taschenbuch der Hochfrequenztechnik*. Springer-Verlag, 1992.

[19] SM Sze and KK Ng, *Physics of Semiconductor Devices*. John Wiley & Sons, 2008.

[20] YN Taur and Tak H, *Fundamentals of modern VLSI devices*. Cambridge university press, 2013.

[21] K Hoffmann, *Systemintegration: vom Transistor zur großintegrierten Schaltung*. Walter de Gruyter, 2012.

[22] S Hommel, N Killat, A Altes, T Schweinboeck, and F Kreupl, *Determination of doping type by calibrated capacitance scanning microwave microscopy*, Microelectronics Reliability **76**, 218–221 (2017).

[23] B Rong, LK Nanver, JN Burghartz, ABM Jansman, AGR Evans, and BS Rejaei, *CV characterization of MOS capacitors on high resistivity silicon substrate*, in *European Solid-State Device Research, 2003. ESSDERC'03. 33rd Conference on*, pp. 489–492, IEEE. 2003.

[24] B Rong, *Capacitance-voltage characterization for MOS capacitor on p-type high-resistivity silicon substrate*, in *Solid-State and Integrated Circuits Technology, 2004. Proceedings. 7th International Conference on*, vol. 1, pp. 198–201, IEEE. 2004.

[25] O Rejaiba, M Ben Amar, and A Matoussi, *Effects of series and parallel resistances on the CV characteristics of silicon-based metal oxide semiconductor (MOS) devices*, The European Physical Journal Plus **130**, 80 (2015).

[26] O Rejaiba, AF Braña, and A Matoussi, *Series and parallel resistance effects on the C–V and G–V characteristics of Al/SiO2/Si structure*, Journal of Computational Electronics **15**, 831–838 (2016).

[27] P Fernández-Martínez, FR Palomo, S Hidalgo, C Fleta, F Campabadal, and D Flores, *Analysis of displacement damage effects on MOS capacitors*, Nuclear Instruments and Methods in Physics Research Section A: Accelerators, Spectrometers, Detectors and Associated Equipment **730**, 91–94 (2013).

[28] M Pfost, HM Rein, and T Holzwarth, *Modeling substrate effects in the design of high-speed Si-bipolar ICs*, IEEE Journal of Solid-State Circuits **31**, 1493–1501 (1996).

[29] JA Luna-Lopez, M Aceves-Mijares, Malik Oleksandr, and R Glaenzer, *Modelling the CV characteristics of MOS capacitor on high resistivity silicon substrate for PIN photodetector applications*, Revista mexicana de física **52**, 45–47 (2006).

[30] G Binnig, H Rohrer, C Gerber, and E Weibel, *Surface studies by scanning tunneling microscopy*, Physical review letters **49**, 57 (1982).

[31] G Binnig, CF Quate, and C Gerber, *Atomic force microscope*, Physical review letters **56**, 930 (1986).

[32] M Dukic, JD Adams, and GE Fantner, *Piezoresistive AFM cantilevers surpassing standard optical beam deflection in low noise topography imaging*, Scientific reports **5**, 16393 (2015).

[33] P Girard, *Electrostatic force microscopy: principles and some applications to semiconductors*, Nanotechnology **12**, 485 (2001).

[34] G Gramse, M Kasper, L Fumagalli, G Gomila, P Hinterdorfer, and F Kienberger, *Calibrated complex impedance and permittivity measurements with scanning microwave microscopy*, Nanotechnology **25**, 145703 (2014).

[35] L Fumagalli, MA Edwards, and G Gomila, *Quantitative electrostatic force microscopy with sharp silicon tips*, Nanotechnology **25**, 495701 (2014).

[36] L Fumagalli, G Ferrari, M Sampietro, I Casuso, E Martinez, J Samitier, and G Gomila, *Nanoscale capacitance imaging with attofarad resolution using ac current sensing atomic force microscopy*, Nanotechnology **17**, 4581 (2006).

[37] A Bachtold, MS Fuhrer, S Plyasunov, M Forero, Erik H Anderson, A Zettl, and Paul L McEuen, *Scanned probe microscopy of electronic transport in carbon nanotubes*, Physical review letters **84**, 6082 (2000).

[38] M Kasper, G Gramse, and F Kienberger, *An advanced impedance calibration method for nanoscale microwave imaging*, in *Microwave Symposium (IMS), 2016 IEEE MTT-S International*, pp. 1–4, IEEE. 2016.

[39] J Smoliner, HP Huber, M Hochleitner, M Moertelmaier, and F Kienberger, *Scanning microwave microscopy/spectroscopy on*

metal-oxide-semiconductor systems, Journal of Applied Physics **108**, 064315 (2010).

[40] A Imtiaz, TM Wallis, SH Lim, H Tanbakuchi, HP Huber, A Hornung, P Hinterdorfer, J Smoliner, F Kienberger, and P Kabos, *Frequency-selective contrast on variably doped p-type silicon with a scanning microwave microscope*, Journal of Applied Physics **111**, 093727 (2012).

[41] T Schweinboeck and S Hommel, *Quantitative scanning microwave microscopy: A calibration flow*, Microelectronics Reliability **54**, 2070–2074 (2014).

[42] J Rossignol, C Plassard, E Bourillot, O Calonne, M Foucault, and E Lesniewska, *Imaging of Located Buried Defects in Metal Samples by an Scanning Microwave Microscopy*, Procedia Engineering **25**, 1637–1640 (2011).

[43] J Myers, S Mou, KH Chen, and Y Zhuang, *Scanning microwave microscope imaging of micro-patterned monolayer graphene grown by chemical vapor deposition*, Applied Physics Letters **108**, 053101 (2016).

[44] G Gramse, E Brinciotti, A Lucibello, SB Patil, M Kasper, C Rankl, R Giridharagopal, P Hinterdorfer, R Marcelli, and F Kienberger, *Quantitative sub-surface and non-contact imaging using scanning microwave microscopy*, Nanotechnology **26**, 135701 (2015).

[45] MC Biagi, R Fabregas, G Gramse, M Van Der Hofstadt, A Juarez, F Kienberger, L Fumagalli, and G Gomila, *Nanoscale electric permittivity of single bacterial cells at gigahertz frequencies by scanning microwave microscopy*, ACS nano **10**, 280–288 (2015).

[46] YJ Oh, HP Huber, M Hochleitner, M Duman, B Bozna, M Kastner, F Kienberger, and P Hinterdorfer, *High-frequency electromagnetic dynamics properties of THP1 cells using scanning microwave microscopy*, Ultramicroscopy **111**, 1625–1629 (2011).

[47] J Hoffmann, M Wollensack, M Zeier, J Niegemann, HP Huber, and F Kienberger, *A calibration algorithm for nearfield scanning microwave microscopes*, in *Nanotechnology (IEEE-NANO), 2012 12th IEEE Conference on*, pp. 1–4, IEEE. 2012.

[48] I Volotsenko, M Molotskii, Z Barkay, J Marczewski, P Grabiec, B Jaroszewicz, G Meshulam, E Grunbaum, and Y Rosenwaks, *Secondary electron doping contrast: Theory based on scanning electron microscope and Kelvin probe force microscopy measurements*, Journal of Applied Physics **107**, 014510 (2010).

[49] AKW Chee, RF Broom, CJ Humphreys, and EGT Bosch, *A quantitative model for doping contrast in the scanning electron microscope using calculated potential distributions and Monte Carlo simulations*, Journal of Applied Physics **109**, 013109 (2011).

[50] AKW Chee, *Quantitative dopant profiling by energy filtering in the scanning electron microscope*, IEEE Transactions on Device and Materials Reliability **16**, 138–148 (2016).

[51] SL Elliott, RF Broom, and CJ Humphreys, *Dopant profiling with the scanning electron microscope-A study of Si*, Journal of applied physics **91**, 9116–9122 (2002).

[52] H Murray, R Germanicus, A Doukkali, P Martin, B Domenges, and P Descamps, *Analytic description of scanning capacitance microscopy*, Journal of Vacuum Science & Technology B: Microelectronics and Nanometer Structures Processing, Measurement, and Phenomena **25**, 1340–1352 (2007).

[53] JS McMurray, J Kim, and CC Williams, *Quantitative measurement of two-dimensional dopant profile by cross-sectional scanning capacitance microscopy*, Journal of Vacuum Science & Technology B: Microelectronics and Nanometer Structures Processing, Measurement, and Phenomena **15**, 1011–1014 (1997).

[54] A Shik and HE Ruda, *A Theoretical Analysis of Scanning Capacitance Microscopy*, in *AIP Conference Proceedings*, vol. 696, pp. 947–954, AIP. 2003.

[55] A Shik and HE Ruda, *Theoretical problems of scanning capacitance microscopy*, Surface science **532**, 1132–1135 (2003).

[56] VV Zavyalov, JS McMurray, and CC Williams, *Surface and tip characterization for quantitative two dimensional dopant profiling by scanning capacitance microscopy*, in *AIP Conference Proceedings*, vol. 449, pp. 753–756, AIP. 1998.

[57] JF Marchiando, JJ Kopanski, and JR Lowney, *Model database for determining dopant profiles from scanning capacitance microscope measurements*, Journal of Vacuum Science & Technology B: Microelectronics and Nanometer Structures Processing, Measurement, and Phenomena **16**, 463–470 (1998).

[58] J Smoliner, B Basnar, S Golka, E Gornik, B Loeffler, M Schatzmayr, and H Enichlmair, *Mechanism of bias-dependent contrast in scanning-capacitance-microscopy images*, Applied Physics Letters **79**, 3182–3184 (2001).

[59] O Amster, F Stanke, S Friedman, Y Yang, DW St J, and B Drevniok, *Practical quantitative scanning microwave impedance microscopy*, Microelectronics Reliability **76**, 214–217 (2017).

[60] F Stanke, Y Yang, O Amster, *et al.*, *Advances in imaging and quantification of electrical properties at the nanoscale using Scanning Microwave Impedance Microscopy (sMIM)*, Bulletin of the American Physical Society **61**, (2016).

[61] L Lei, R Xu, S Ye, X Wang, K Xu, S Hussain, YJ Li, Y Sugawara, L Xie, W Ji, *et al.*, *Local characterization of mobile charge carriers by two electrical AFM modes: multi-harmonic EFM versus sMIM*, Journal of Physics Communications **2**, 025013 (2018).

[62] S Friedman, Y Yang, and O Amster, *Advances in imaging and quantification of electrical properties at the nanoscale using Scanning Microwave Impedance Microscopy (sMIM)*, in *APS Meeting Abstracts*. 2015.

[63] O Amster, Y Yang, B Drevniok, S Friedman, F Stanke, and DW St J, *Practical quantitative scanning microwave impedance microscopy of semiconductor devices*, in *Physical and Failure Analysis of Integrated Circuits (IPFA), 2017 IEEE 24th International Symposium on the*, pp. 1–4, IEEE. 2017.

[64] P De Wolf, R Stephenson, T Trenkler, T Clarysse, T Hantschel, and W Vandervorst, *Status and review of two-dimensional carrier and dopant profiling using scanning probe microscopy*, Journal of Vacuum Science & Technology B: Microelectronics and Nanometer Structures Processing, Measurement, and Phenomena **18**, 361–368 (2000).

[65] S Doering, A Wachowiak, U Winkler, M Richter, J Goehler, H Roetz, S Eckl, and T Mikolajick, *Scanning Spreading Resistance Microscopy analysis of locally blocked implant sites*, Microelectronic Engineering **122**, 77–81 (2014).

[66] S Doering, A Wachowiak, M Rochel, C Nowak, M Hoffmann, U Winkler, M Richter, H Roetz, S Eckl, and T Mikolajick, *Polycrystalline silicon gate originated CMOS device failure investigated by Scanning Spreading Resistance Microscopy*, Microelectronic Engineering **142**, 40–46 (2015).

[67] P Ferrada, R Harney, E Wefringhaus, S Doering, S Jakschick, T Mikolajick, P Eyben, T Hantschel, W Vandervorst, M Weiss, *et al.*, *Local Doping Profiles for Height-Selective Emitters Determined by Scanning Spreading Resistance Microscopy (SSRM)*, IEEE Journal of Photovoltaics **3**, 168–174 (2013).

[68] P Eyben, S Denis, T Clarysse, and W Vandervorst, *Progress towards a physical contact model for scanning spreading resistance microscopy*, Materials Science and Engineering: B **102**, 132–137 (2003).

[69] S Doering, R Rudolf, M Pinkert, H Roetz, C Wagner, S Eckl, M Strasser, A Wachowiak, and T Mikolajick, *Scanning spreading resistance microscopy for failure analysis of nLDMOS devices with decreased breakdown voltage*, Microelectronics Reliability **54**, 2128–2132 (2014).

[70] P Eyben, D Degryse, and W Vandervorst, *On the spatial resolution of scanning spreading resistance microscopy: experimental assessment and electro-mechanical modeling*, in *AIP Conference Proceedings*, vol. 788, pp. 264–269, AIP. 2005.

[71] K Mylvaganam, LC Zhang, P Eyben, J Mody, and W Vandervorst, *Evolution of metastable phases in silicon during nanoindentation: mechanism analysis and experimental verification*, Nanotechnology **20**, 305705 (2009).

[72] W Choi, E Seabron, PK Mohseni, JD Kim, T Gokus, A Cernescu, P Pochet, HT Johnson, WL Wilson, and X Li, *Direct electrical probing of periodic modulation of zinc-dopant distributions in planar gallium arsenide nanowires*, ACS nano **11**, 1530–1539 (2017).

[73] ET Ritchie, DJ Hill, TM Mastin, PC Deguzman, JF Cahoon, and JM Atkin, *Mapping Free-Carriers in Multijunction Silicon Nanowires Using Infrared Near-Field Optical Microscopy*, Nano letters **17**, 6591–6597 (2017).

[74] R Hillenbrand, B Knoll, and F Keilmann, *Pure optical contrast in scattering-type scanning near-field microscopy*, Journal of microscopy **202**, 77–83 (2001).

[75] R Jacob, S Winnerl, H Schneider, M Helm, MT Wenzel, HG von Ribbeck, LM Eng, and SC Kehr, *Quantitative determination of the charge carrier concentration of ion implanted silicon by IR-near-field spectroscopy*, Optics Express **18**, 26206–26213 (2010).

[76] J Wittborn, R Weiland, D Kazantsev, A Huber, R Hillenbrand, and F Keilmann, *Material and doping contrast in semiconductor devices at*

nanoscale resolution using scattering-type scanning near-field optical microscopy, in *INTERNATIONAL SYMPOSIUM FOR TESTING AND FAILURE ANALYSIS*, vol. 32, p. 98, ASM International; 1998. 2006.

[77] J Wittborn, R Weiland, AJ Huber, F Keilmann, and R Hillenbrand, *Quantitative, nanoscale free-carrier concentration mapping using terahertz near-field nanoscopy*, in *Reliability Physics Symposium (IRPS), 2011 IEEE International*, pp. 5C–1, IEEE. 2011.

[78] C Maissen, S Mastel, J Hesler, S Hommel, T Schweinboeck, I Amenabar, and R Hillenbrand, *Synthetic optical holography for phase resolved Terahertz nano-imaging at sub-50 nm resolution*, in *Conference Program of the 6th EOS Topical Meeting on Terahertz Science & Technology (TST 2018)*, 6th EOS Topical Meeting on Terahertz Science & Technology (TST 2018). 2018.

[79] E Brinciotti, G Gramse, S Hommel, T Schweinboeck, A Altes, MA Fenner, J Smoliner, M Kasper, G Badino, SS Tuca, and F Kienberger, *Probing resistivity and doping concentration of semiconductors at the nanoscale using scanning microwave microscopy*, Nanoscale **7**, 14715–14722 (2015).

[80] E Brinciotti, G Campagnaro, G Badino, M Kasper, G Gramse, SS Tuca, J Smoliner, T Schweinboeck, S Hommel, and F Kienberger, *Frequency analysis of dopant profiling and capacitance spectroscopy using Scanning Microwave Microscopy*, IEEE Transactions on Nanotechnology **16**, 75–82 (2017).

[81] S Hommel, N Killat, A Altes, T Schweinboeck, D Schmitt-Landsiedel, M Silvestri, and O Haeberlen, *Scanning microwave microscopy for electronic device analysis on nanometre scale*, Microelectronics Reliability **64**, 310–312 (2016).

[82] H Morkoç, A Di Carlo, and R Cingolani, *GaN-based modulation doped FETs and UV detectors*, Solid-State Electronics **46**, 157–202 (2002).

[83] K Lai, W Kundhikanjana, M Kelly, and ZX Shen, *Modeling and characterization of a cantilever-based near-field scanning microwave impedance microscope*, Review of scientific instruments **79**, 063703 (2008).

[84] S Berweger, JC Weber, J John, JM Velazquez, A Pieterick, NA Sanford, AV Davydov, B Brunschwig, NS Lewis, TM Wallis, *et al.*, *Microwave near-field imaging of two-dimensional semiconductors*, Nano letters **15**, 1122–1127 (2015).

[85] DE Steinhauer, CP Vlahacos, FC Wellstood, Steven M Anlage, C Canedy, R Ramesh, A Stanishevsky, and J Melngailis, *Quantitative imaging of dielectric permittivity and tunability with a near-field scanning microwave microscope*, Review of Scientific Instruments **71**, 2751–2758 (2000).

[86] JH Lee, S Hyun, and K Char, *Quantitative analysis of scanning microwave microscopy on dielectric thin film by finite element calculation*, Review of Scientific Instruments **72**, 1425–1434 (2001).

[87] EC Jordan and CL Andrews, *Electromagnetic waves and radiating systems*, American Journal of Physics **19**, 130 (1951).

[88] G Gomila, J Toset, and L Fumagalli, *Nanoscale capacitance microscopy of thin dielectric films*, Journal of Applied Physics **104**, 024315 (2008).

[89] G Gomila, G Gramse, and L Fumagalli, *Finite-size effects and analytical modeling of electrostatic force microscopy applied to dielectric films*, Nanotechnology **25**, 255702 (2014).

[90] L Fumagalli, G Ferrari, M Sampietro, and G Gomila, *Dielectric-constant measurement of thin insulating films at low frequency by nanoscale capacitance microscopy*, Applied Physics Letters **91**, 243110 (2007).

[91] Y Ahn, JY Yoon, CW Baek, and YK Kim, *Chemical mechanical polishing by colloidal silica-based slurry for micro-scratch reduction*, Wear **257**, 785–789 (2004).

[92] M Morita, T Ohmi, E Hasegawa, M Kawakami, and M Ohwada, *Growth of native oxide on a silicon surface*, Journal of Applied Physics **68**, 1272–1281 (1990).

[93] Y Ammar, *Software Optimization for Scanning Microwave Microscopy Data Processing*, bachelor thesis, Technical University of Munich, 2017.

[94] P Avouris, T Hertel, and R Martel, *Atomic force microscope tip-induced local oxidation of silicon: kinetics, mechanism, and nanofabrication*, Applied Physics Letters **71**, 285–287 (1997).

[95] H Aida, H Takeda, K Koyama, H Katakura, K Sunakawa, and T Doi, *Chemical mechanical polishing of gallium nitride with colloidal silica*, Journal of The Electrochemical Society **158**, 1206–1212 (2011).

[96] NL Cohen, RE Paulsen, and MH White, *Observation and characterization of near-interface oxide traps with CV techniques*, IEEE Transactions on Electron Devices **42**, 2004–2009 (1995).

[97] H Tahi, B Djezzar, A Benabdelmoumene, A Chenouf, and M Goudjil, *Investigation of interface, shallow and deep oxide traps under NBTI stress using charge pumping technique*, Microelectronics Reliability **54**, 882–888 (2014).

[98] D Vuillaume, JC Bourgoin, and M Lannoo, *Oxide traps in Si-SiO 2 structures characterized by tunnel emission with deep-level transient spectroscopy*, Physical Review B **34**, 1171 (1986).

[99] S Hommel, N Killat, T Schweinboeck, A Altes, and F Kreupl, *Resolving Trap-caused Charges by Scanning Microwave Microscopy*, in *Physical and Failure Analysis of Integrated Circuits (IPFA), 2018 IEEE 25th International Symposium on the*, pp. 1–3, IEEE. 2018.

[100] TR Oldham and FB McLean, *Total ionizing dose effects in MOS oxides and devices*, IEEE Transactions on Nuclear Science **50**, 483–499 (2003).

[101] TR Oldham, ed., *Ionizing radiation effects in MOS oxides.* World Scientific, 1999.

Danksagung

An dieser Stelle möchte ich mich bei allen Bedanken, die mich während meiner Zeit als Doktorand unterstützt haben. In diesem Zusammenhang gilt mein Dank auch dem BMBF, der diese Promotion im Rahmen des europäischen EUREKA EURIPIDES und CATRENE Programms unter der Nummer 16ES0339k gefördert hat.

Vielen Dank an Prof. Franz Kreupl, der mich von Seiten der TUM betreut hat und es mir damit ermöglicht hat, meine Promotion an der TUM durchzuführen. Auch wenn der Kontakt wahrscheinlich nicht so intensiv war wie bei internen Doktoranden, konnte ich mich doch stets darauf verlassen innerhalb kürzester Zeit Rat oder produktives Feedback per Telefon oder E-Mail einholen zu können.

Ein großes Dankeschön gebührt auch der gesamten Abteilung der Infineon Fehleranalyse in München für die tolle Unterstützung mit Fachwissen und ihrer Erfahrung, aber auch für die tolle Arbeitsatmosphäre. Ich habe meine Zeit als Doktorand bei euch sehr genossen.

Mein ganz besonderer Dank gilt hier Thomas Schweinböck, der mir die Möglichkeit gegeben hat, mich mit dieser spannenden Aufgabenstellung zu beschäftigen. Und natürlich dafür, dass er sich die Themenstellung in dieser Form überhaupt erst mit mir ausgedacht hat. Er war auch fast immer mein erster Diskussionspartner, wenn ich mal wieder eine neue Idee hatte und hat viel Zeit in Korrekturlesen von Papern und der Dissertation investiert. Dankeschön auch dafür, dass ich meine Ergebnisse auf den Fehleranalysekonferenzen und Tagungen präsentieren konnte. Vielen Dank auch für die Unterstützung schon auf dem Weg zum Doktoranden durch diverse studentische Anstellungen in der Fehleranalyse.

Ein besonderes Dankeschön möchte ich auch an Nicole Killat richten, die mich bei Papern und der Dissertation durch intensivstes Korrekturlesen und Aufzeigen der Probleme in Formulierungen und Struktur riesig unterstützt hat, auch wenn sie als Belohnung dafür oft noch mit mir diskutieren musste, bis ich die Verbesserung hinter einer Änderung eingesehen habe.

Einen ebenso großen Dank auch an Andreas Altes für seine Unterstützung, der die Arbeit seitens Infineon betreut hat, sowohl für das ausgedehnte Kor-

rekturlesen als auch für die vielen fachlichen Diskussionen.
Und ein weiteres besonderes Dankeschön gilt auch Klaus Lidl, erstmal für die Geduld und Arbeit bei meinen Ideen, SCM und SMM Schliffe eingebettet zu machen und dann für die absolut perfekte Qualität der Schliffe seitdem die Methode etabliert ist. Ansonsten sähen einige Messungen in dieser Arbeit wohl anders aus.
Vielen Dank auch an Yassine Ammar, dessen aus seiner Bachelorarbeit zur SMM Datenauswertung entstandenes Skript mir das Leben doch deutlich erleichtert hat.
Weiterhin möchte ich mich bei Tina Zoth, Mehdi Kashani, Stefan Littin, Lloyd Grills, Jessica Frank, Christoph Möller und Boris Scherwitzel für die lustige Zeit, ob auf der Arbeit oder Privat, bedanken.
Über die FA hinaus möchte ich mich noch für die Unterstützung durch Proben bei Oliver Häberlen, Marco Silvestri, Harald Böhm, Karl Heinz Bach, Stefan Decker, Joost Willemen, Peter Christmann und Lauri Knuuttila bedanken. Und bei Markus Zundel und natürlich wieder Thomas Schweinböck, deren Kalibriersample maßgeblich zum Verständnis der Signale beigetragen hat.
Einen Riesendank möchte ich auch an meine Familie für die Unterstützung während meiner gesamten Studienzeit richten. Vielen Dank an meine Mutter Birgit und meinen Bruder Malte, die mich immer in all meinen Zielen ermutigt und bestärkt und unterstützt haben und immer an mich geglaubt haben.
Den allergrößten Dank von allen möchte ich an meine Frau Daniela richten, die all meine Hochs und Tiefs abfängt, sich mit mir freut und auch schön mit mir schimpft und mir immer das Gefühl gibt zu Hause zu sein.